



A.S. GAIA

SF2A 2011

Paris, 20-21 juin 2011
Centre FIAP Jean Monnet

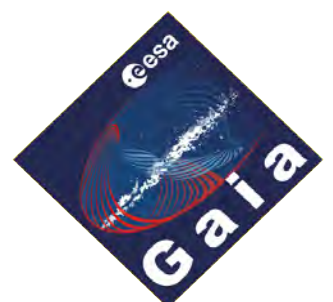
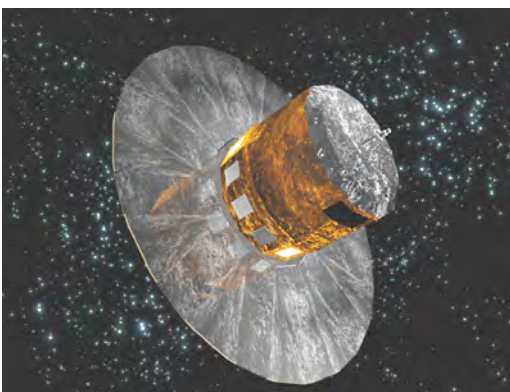


Table des matières

| | |
|--|------|
| Préface | p 5 |
| Présentation de l'AS Gaia en séance plénière | p 7 |
| Présentations invitées et contributions orales | p 15 |
| Posters | p 73 |

Préface

Les Journées de la SF2A sont, chaque année, pour l'A.S. Gaia l'occasion de présenter, et de discuter en collaboration avec les Programmes Nationaux qui pavent la discipline, les différents champs d'application des futures données de Gaia. En effet, celles-ci seront uniques à plusieurs points de vue : recensement complet du ciel pour tous les objets plus brillants que la magnitude 20 (étoiles, objets du Système Solaire ou objets extragalactiques quasi-ponctuels), données astrométriques d'une précision inconnue jusqu'ici (100 fois plus précises qu'Hipparcos pour une étoile de magnitude 10, encore un ordre de grandeur plus précises que la précision moyenne d'Hipparcos pour les étoiles de magnitude 20), données photométriques et spectroscopiques acquises en parallèle pour l'ensemble des objets observés (pour la photométrie) ou pour la partie la plus brillante du programme (pour la spectroscopie).

En 2011, la physique stellaire et interstellaire était à l'honneur, avec une présentation de Bertrand Plez pendant la session plénière de la SF2A, le mardi 21 juin au matin, sur « **Stellar Physics with Gaia** ». Sa présentation est disponible en ligne à l'adresse suivante :

http://wwwhip.obspm.fr/AS/squelettes/doc/Plez_AS_Gaia_SF2A2011.pdf

et le texte correspondant est inclus dans ce fascicule et disponible en ligne à l'adresse <http://sf2a.cesr.fr/2011/2011sf2a.conf..0047P.pdf>.

Par ailleurs, l'A.S. Gaia a été à l'initiative d'un atelier commun A.S. Gaia-PNPS-PNCG-PCMI « **Stellar and Interstellar physics for the modelling of the Galaxy and its components** », A03, qui s'est tenu les 20 et 21 juin 2011. La SF2A ayant l'honneur d'inviter cette année la Société Astronomique Espagnole (SEA), nous avons profité de cette occasion pour inviter nos collègues espagnols très impliqués dans Gaia, les observations complémentaires au sol ou la préparation de l'exploitation scientifique des futures données du satellite.

Cet atelier a rassemblé des scientifiques travaillant sur Gaia (analyse des données et préparation de l'exploitation scientifique) ainsi que des collègues des domaines de la Physique Stellaire, du Milieu Interstellaire et de la modélisation de la Galaxie et de ses composantes. Il a permis d'aborder d'une part les conséquences de l'arrivée des données de Gaia (en particulier des distances extrêmement précises pour un très grand nombre d'étoiles) sur la physique stellaire et la compréhension du milieu interstellaire, mais aussi d'identifier les thèmes de physique stellaire et du milieu interstellaire à développer pour interpréter au mieux les données Gaia en terme de structure et d'évolution de la Galaxie et des galaxies proches.

Le présent fascicule rassemble l'ensemble des textes correspondant aux présentations orales et aux posters présentés lors de cet Atelier A03. Lorsque les textes ne sont pas disponibles, les abstracts sont donnés. Ils sont ici présentés dans l'ordre des présentations orales (présentations invitées et contributions), puis dans l'ordre alphabétique des posters. Les numéros des pages correspondent à la publication « Proceedings of the annual meeting of the French Society of Astronomy and Astrophysics, Paris, 20-23 June 2011, G. Alecian, K. Belkacem, R. Samadi & D. Valls-Gabaud (eds) ». Ces textes sont par ailleurs disponibles sur l'ADS et, par ordre alphabétique, sur le site de la SF2A, Atelier A03 :

<http://sf2a.cesr.fr/php/spip/spip.php?article350#3>

et dans les comptes-rendus complets des Journées de la SF2A 2011, disponibles à l'adresse <http://lesia.obspm.fr/semaine-sf2a/2011/proceedings/2011/book.pdf>.

Les présentations ou posters eux-mêmes sont disponibles sur le site de l'A.S. Gaia, à l'adresse suivante :

<http://wwwhip.obspm.fr/AS/animation/article/journee-sf2a-2011>.

Catherine Turon, Frédéric Arenou et Misha Haywood

**Présentation de l'AS Gaia
pendant la session plénière de la SF2A**

STELLAR PHYSICS WITH GAIA

B. Plez¹

Abstract. Gaia will provide a three-dimensional map of our Galaxy, with unprecedented positional and radial velocity measurements for about one per cent of the Galactic stellar population. Combined with astrophysical information derived from spectroscopy and photometry for each star, this will lead to a detailed understanding of the formation, and dynamical and chemical evolution of our Galaxy. Other scientific products include extra-solar planets, minor bodies in the solar system, or distant quasars. The contribution of Gaia to stellar physics is less publicized, although very significant. I show here a number of illustrative examples. For example, we will have access to very precise HR diagrams with very large sample of stars allowing extensive tests of fine effects in stellar evolution. Accurate parameters (esp. luminosities, and masses) will allow the independent determination of surface gravities, the characterization of non-LTE effects, and the derivation of more accurate chemical abundances. We will be able to quantify transport processes in various populations of stars, and shed new light on abundance anomalies. In addition, the preparation of Gaia induces a very large effort devoted to homogenize the stellar parameters of a great number of reference stars, and the development of performant tools designed to automatically extract parameters from tremendous amounts of spectra.

Keywords:

1 Introduction

Gaia's main goal is to provide high-precision astrometric data (positions, parallaxes, and proper motions) for one billion objects in the sky. These data, together with multi-epoch photometric and spectroscopic data will allow us to reconstruct the formation history, structure, and evolution of the Galaxy. Many other exciting breakthroughs will also result from this tremendous data set of unprecedented accuracy, in the fields of, e.g., exoplanets, fundamental physics, solar system science, dark matter, the cosmological distance scale (Perryman et al. 2001). In the study of the Galaxy, stars are used as markers of the kinematics, and chemistry. The purpose of this paper is to show that stars will be studied by Gaia as targets per se. We will gain insight into various aspects of stellar physics, thanks to the knowledge of many accurate distances, luminosities, radii, and masses. In addition the preparation of the Gaia mission generates an enormous amount of efforts aimed at a better understanding of stars, and at the development of extremely performant tools for the analysis of stellar observations. I will illustrate these two points through selected examples in the following.

2 What will Gaia provide for stellar physics studies?

Gaia aims at measuring parallaxes of one billion stars with an accuracy better than 300 micro-arcsec, for a complete magnitude limited sample down to $V=20$. The accuracy will be 20 mas (milli-arcsec) for 26 million stars down to $V=15$. As an illustration this translates to 2% errors for Sun-like stars at 1 kpc, 5% errors for red giants out to 2.5 kpc, and M-L dwarfs distances with 3% errors within 100 pc. In total, distances will be known to better than 1% for 11 million stars, and to better than 10% for 150 million stars. Proper motions should be 50% more accurate than parallaxes. The RVS (radial velocity spectrometer) will collect radial velocities down to $V=16$, with an accuracy of 1 to 10 km/s. Details about all these numbers can be found in Turon et al. (2012), and at <http://www.rssd.esa.int>. This unprecedented data set will allow the determination of accurate luminosities for a very large sample of stars. Luminosity (L) is the most commonly missing parameter

¹ LUPM, UMR 5299, CNRS, Université Montpellier 2, 34095 Montpellier, France

in Galactic star studies. Luminosities combined with effective temperatures (T_{eff}) derived from photometry or spectroscopy will give radii (R). With precise masses (M) from the numerous binaries, this will lead to surface gravities (g) independently of ill-controlled hypotheses, as is the case when they are spectroscopically derived, due to NLTE effects. An aspect not to underestimate is the possibility to increase the scientific return using Gaia data in synergy with asteroseismology data that provide strong constraint on other combinations of stellar parameters such as the mean density, M/R^3 or the state of evolution. The multiple epochs of observation (80 per object on average) will allow the study of stellar variability, and of rare types of stars in short evolutionary stages. It is estimated that about 18 million variables will be observed and characterized (Eyer & Cuyppers 2000).

3 Examples in the field of stellar evolution

One field that will greatly benefit from Gaia results is stellar structure and evolution. Modeling stellar evolution requires the inclusion of the the most up-to-date physics, e.g., equation of state, nuclear reaction rates, opacities, atomic diffusion, atmosphere models. Special difficulties are encountered for cool, dense stars, late stages of evolution, and of course when very accurate modeling is demanded by very high-quality observations, as in the case of the Sun (Lebreton 2005, 2008). Atmospheres are a particularly critical ingredient as they constitute the boundary condition of the stellar interior, they provide the transformation from theoretical (L , T_{eff}) to observed quantities like magnitudes, colors, and bolometric corrections. Finally, the stellar parameters T_{eff} , $\log g$, chemical composition, are mostly derived from spectroscopic or photometric observations using calculated spectra from model atmospheres. Despite great recent progress (opacities, 3D hydrodynamical models, NLTE calculations), there are still relatively large systematic errors for, e.g., cool giants, hot stars, very metal-poor stars.

3.1 Isochrones: calculations and observations

Stellar evolution models provide stellar parameters like $L(t)$, $R(t)$, $T_{\text{eff}}(t)$, $Z(t)$, that must be confronted to quantities derived from observations, in order to estimate ages, masses, helium content, or metallicities. One widely used, and in principle straightforward way to derive a star's age, mass and initial metal content is to compute isochrones for a distribution of initial masses and just place the star in the magnitude- T_{eff} diagram. This is not as easy as it seems, nor unambiguous. Isochrones overlap on the main sequence, around the turn-off, and on the red giant branch (RGB). But even outside these domains, there is a need for very precise, and accurate L , T_{eff} , and metallicity determinations (Jørgensen & Lindegren 2005). Gaia will dramatically increase the precision of luminosity determinations through better distance measurements, and indirectly also the precision of stellar parameter determinations (see section 4), thus allowing better age determinations (Lebreton & Montalbán 2009). Nevertheless, only the combination with asteroseismology will allow to lift degeneracies in the HR diagram (Lebreton 2011; Gilliland et al. 2011).

3.2 Validation of stellar evolution models

Before these models can be used on a large scale they must be validated using well observed, well constrained systems, of which the Sun, and the α Cen binary are among the few that can be used nowadays.

The case of the Sun is much debated, with the most recent atmospheric abundance determinations (Asplund et al. 2005; Grevesse et al. 2010) leading to discordance of the observed and predicted sound speed profile, and of the depth of the lower boundary of the convection zone. The progress we anticipate Gaia will induce in our understanding of stellar structure on one hand, and of line formation and NLTE effects on the other hand will certainly impact the work on the Sun.

The basic parameters of the α Cen system are known within very small error bars. For the A and B components the masses are $M_A = 1.105 \pm 0.007$, $M_B = 0.934 \pm 0.006 M_{\odot}$ (Pourbaix et al. 2002), and the interferometrically derived radii are $R_A = 1.224 \pm 0.003$, $R_B = 0.863 \pm 0.005 R_{\odot}$ (Kervella et al. 2003), resulting in surface gravities $\log g_A = 4.307 \pm 0.005$, $\log g_B = 4.538 \pm 0.008$ (in c.g.s. units). Porto de Mello et al. (2008) recently published a very careful spectroscopic study of the system leading to $T_{\text{eff A}} = 5824 \pm 26$ K, and $T_{\text{eff B}} = 5223 \pm 62$ K. At least for α Cen B, this is not compatible with the hotter $T_{\text{eff B}}$ derived from the very well known luminosity and radius. The fit of isochrones on the system's data leads to different ages for the components. The most probable explanation put forward by Porto de Mello et al. (2008) is that the estimated temperature of the B component is too low. In addition a review of all abundance determinations for this system show a very large scatter (up to 0.4 dex for Ti). To impose a consistent solution for all parameters of

this system brings a strong constraint on atmosphere and evolution models. The important point is that with Gaia we will have many other systems with well determined masses, luminosities, and radii, distributed all over the HR diagram. This will allow stringent tests of the models.

Another contribution of Gaia will be to bring accurate distances for a rich variety of clusters. Clusters are a very powerful way of testing stellar evolution models, as different physical processes dominate the isochrones shape in different parts of the HR diagram. The lower main sequence is impacted by the uncertainties in the calculation of spectra and atmosphere models. The description of convection affects the main sequence around solar-type stars, and rotation and overshooting affect the upper main sequence, and the turn-off, not to forget the effect of the equation of state, opacities, and nuclear reaction rates. The calibration of models on a large number of clusters will open the way to exciting science, as can be seen in the case of the best studied cluster, the Hyades. In addition to the very precise Hipparcos dynamical parallaxes, the presence of the spectroscopic eclipsing binary HD 27130, with very accurate masses and luminosities, allows to delineate the He content of the stars from the isochrones fit (Lebreton et al. 2001). As a consequence of the fit of the tight observational sequence Lebreton et al. (2001) can also discuss details of the physical ingredients used in the models (mixing-length parameter, model atmospheres, equation of state). This illustrates well what will be possible with the Gaia data on clusters.

4 Gaia and the determination of accurate chemical abundances

The chemical composition of stars is a central piece of information, and considerable work has been devoted to improve the quality of the determinations that are made through the analysis of stellar spectra. Most of the time the stellar parameters T_{eff} and $\log g$ are derived from the spectra together with the abundances. However, model atmospheres suffer from approximations (e.g. LTE) that may induce systematic errors in the results. One enlightening example is given by the case of Procyon, a single-lined nearby binary, for which an astrometric determination of the gravity ($\log g = 4.05$), strongly disagrees with a spectroscopic determination based on the ionization equilibrium of iron ($\log g = 3.6$), as is discussed in detail by Fuhrmann et al. (1997). This is a well known manifestation of NLTE: the Fe I/Fe II, or any other element ratio depend critically on inelastic collisions with hydrogen. The cross-sections are not well known, and extremely difficult to calculate or to measure for many atoms, although progress has been made recently (Barklem et al. 2011). The Drawin (1969) approximation of the H-collision cross-sections is commonly used, often with a scaling factor, S_{H} , with values from 0 (no collisions), to about 3, which tends towards the LTE situation. Korn et al. (2003) derived a value $S_{\text{H}} = 3$ from a careful study of iron lines in a few (4) reference stars with known distances (thus L), T_{eff} (thus R), and masses (thus g). They show that the set of fundamental parameters (of which the distance is a critical one) is only compatible with the NLTE Fe I/Fe II ratio calculated using $S_{\text{H}} = 3$. This kind of work can be done today only on a small number of stars. Gaia will provide very large such samples, that will allow a breakthrough in this domain, especially if combined with interferometric and astero-seismologic data.

5 Transport processes and abundance anomalies

The increasing quality of observational data, and refinements in analysis techniques have unveiled abundance peculiarities that require new mechanisms to be taken into account, i.e. mixing, and diffusion. The work of Spite et al. (2007) on field metal-poor red giant stars uncovered two well-separated groups, one with a high N/C, and a low $^{12}\text{C}/^{13}\text{C}$ ratios, and no detectable Li, showing the sign of CN-processing, and mixing. In higher metallicity stars ($[\text{Fe}/\text{H}]=-1.5$), Gratton et al. (2000) showed that extra mixing happens at the bump, as explained by thermohaline mixing (Charbonnel & Zahn 2007; Cantiello & Langer 2010). In the more metal-poor stars of the Spite et al. (2007) sample, however, unmixed stars are found above the bump and mixed stars seem to exist below the bump. In addition variation in Al and Na abundances indicate very deep mixing in some cases. Firm conclusions cannot be drawn, as there exist the possibility that the spectroscopically derived gravities may suffer from uncertainties. More importantly the distances, and thus the luminosities may be in error. Also, the position of the bump is dependent on metallicity and not well defined yet at very low metallicity. Some stars of the sample might also be AGB or RHB stars and not on the RGB. Halo stars are within reach of Gaia, and this question should be settled once good distances are secured for a large number of field metal-poor stars.

5.1 *The case of Li*

Another illuminating example of the contribution of Gaia to stellar physics concerns element diffusion inside stars. The radial chemical composition of stars is not homogeneous, even outside the regions where nuclear reactions operate. In radiative zones, gravitational settling competes with radiative acceleration leading to sometimes strong abundance gradients. The surface composition of a star does not always reflect its inner content. This is particularly critical in the case of Li, the surface abundance of which measured in very metal-poor stars is a factor of 2 or 3 lower than the primordial abundance that is compatible with standard BBN and the WMAP measurements of the cosmic microwave background (Sbordone et al. 2010). Current models including diffusion predict moderate abundance modifications, due to the inclusion of additional turbulent mixing which is unfortunately tuned with a free parameter. The calibration of the amount of turbulent mixing was made by Korn et al. (2006, 2007) using a sequence of stars in the NGC 6397 cluster. The model tuned to match the observed Mg, Ca, Ti, and Fe abundances does explain sub-primordial Li in these cluster stars, offering a solution to this Li problem, as was already suggested by Richard et al. (2005). This work needs to be extended to more metal-poor stars, as the amount of turbulent mixing might be metallicity dependent. As shown in Sbordone et al. (2010) the Spite plateau dissolves at metallicities below -2.5 , and even more below $[\text{Fe}/\text{H}]=-3.0$, further deepening the mystery of primordial Li. To study the effect of element diffusion at such low metallicities demands to know precisely the evolutionary status of field stars, the distances, and luminosities of which are poorly known. Again, Gaia data will be decisive in the solution of this question.

6 Gaia preparation

Apart from much awaited contributions from Gaia science data, the preparation of the mission itself is developing into a full industry of new tools, and approaches in our way of doing stellar physics.

6.1 *Global stellar parametrizers*

The paramount size of the sample of RVS data to be analyzed calls for innovative methods to, e.g., quickly derive stellar parameters from spectra (and in the case of Gaia RVS, relatively low resolution, and restricted range spectra). A number of algorithms (Global Stellar Parametrizers - GSP-spec) have been developed based on optimization (minimization of distance between observations and reference spectra), projection (the observations are projected on a set of vectors defined during a learning phase), or classification (pattern recognition). They prove to be very efficient, once tested and calibrated on well studied samples of spectra. The two algorithms Matisse (Recio-Blanco et al. 2006) and Degas using the two latter methods compare well with published data when applied to spectral libraries (Kordopatis et al. 2011). Their performances are characterized in terms of accuracy depending on the SNR, and the resolution of the spectra, and the position of the star in the HR diagram. Kordopatis et al. (2011) claim that the results are sufficiently accurate down to SNR as low as 20 for galactic archaeology work, opening new horizons in this field. These tools are absolutely indispensable to deal with the extremely large coming surveys, including Gaia. These algorithms are already used to derive stellar parameters (T_{eff} , $\log g$, abundances) from in particular the ESO archive of spectra.

6.2 *Large homogeneous samples of stars*

As is mentioned above, the accuracy to which GSP's will deliver their results is largely dependent on the spectra they are trained on, and on the stellar parameters attached to them. As GSP's are trained on synthetic spectra that are not error-free, systematic errors in astrophysical parameters (AP) may arise. A high quality external calibration with reference stars is therefore mandatory. A Work Package within CU8 of the DPAC of Gaia ("provide calibration of training data") has undertaken this task. The objective is to determine high quality AP's on an homogeneous scale. A few tens of stars that can be studied at very high resolution with a variety of techniques, but too bright for Gaia, will serve as fundamental calibrators. On this basis, AP's will be differentially determined for 500 to 5000 primary calibrators. Then, thousands of secondary calibrators will allow a large scale validation in a large range of stellar parameters, as, e.g., the 90 000 SDSS stellar spectra discussed by Re Fiorentin et al. (2007). Also, many large samples analyzed in recent years by various authors will be homogenized using the tools described above, coupled with the detailed study of primary calibrators. This is an unprecedented major effort, extremely important to validate stellar models, and that will impact stellar physics at large.

6.3 3D hydrodynamical models, photocenters, and parallax accuracies

The preparation for Gaia also benefits from efforts to develop more ambitious models of stellar atmospheres and interiors. 3D hydrodynamical simulations of red giants and supergiants atmospheres dominated by granulation are now able to make quantitative predictions on the size of granules, their intensity contrast, the shifts and asymmetries affecting spectral line, and their time scales. Chiavassa et al. (2011) have showed that the fluctuations in the position of the photocenter of red supergiants are of the order of a fraction of an AU. This will result in systematic errors in Gaia's parallax determinations of the order of 5%. In return Gaia measurements will help verify these predictions on a large number of stars, which can not be done with, e.g., interferometers from the ground, as it necessitates repeated observations of a number of stars during a few years.

7 Conclusions

Gaia will increase our sample of binary systems with masses known to the 1% level from 100 to about 17 000. It will bring us 11 million stars with parallaxes at the 1% level, to compare with the 700 we have today, of which 100 000 will have a 0.1% accuracy. We will have parallaxes for types of stars for which we have none today (subdwarfs, subgiants). The distance to individual stars in 20 globular clusters (100 to 100 000 stars per cluster) will be determined to better than 10%. It is obvious that this will revolutionize our view of the Galaxy and its evolution. I have shown here that the tremendous Gaia data set, combined with interferometric (R/d), and astero-seismologic (e.g., M/R^3) data will also allow stringent tests, and validations of models of the interior and atmosphere of stars. This will ultimately lead to a much improved quantitative understanding of the physical processes at work in stars.

Stellar physics is a broad field the diversity of which no one can fully embrace. On many topics discussed here I am merely the carrier of others words. Many colleagues helped me while preparing this paper, and without them the task would have been much heavier. Be they all thanked here: Alain Jorissen, Andrea Chiavassa, Andreas Korn, Caroline Soubiran, François Spite, Mathias Schultheis, Monique Spite, Olivier Richard, Patrick de Laverny, and not the least Yveline Lebreton. I thank the AS Gaia and the SF2A for inviting me, and the AS Gaia for providing financial support. Special thanks to Catherine Turon, who so kindly insisted that I gave this talk at the Annual Meeting of the SF2A. I truly enjoyed it.

References

- Asplund, M., Grevesse, N., & Sauval, A. J. 2005, in *Astronomical Society of the Pacific Conference Series*, Vol. 336, *Cosmic Abundances as Records of Stellar Evolution and Nucleosynthesis*, ed. T. G. Barnes III & F. N. Bash, 25
- Barklem, P. S., Belyaev, A. K., Guitou, M., et al. 2011, *A&A*, 530, A94
- Cantiello, M. & Langer, N. 2010, *A&A*, 521, A9
- Charbonnel, C. & Zahn, J.-P. 2007, *A&A*, 467, L15
- Chiavassa, A., Pasquato, E., Jorissen, A., et al. 2011, *A&A*, 528, A120
- Drawin, H. W. 1969, *Zeitschrift für Physik*, 228, 99
- Eyer, L. & Cuypers, J. 2000, in *Astronomical Society of the Pacific Conference Series*, Vol. 203, *IAU Colloq. 176: The Impact of Large-Scale Surveys on Pulsating Star Research*, ed. L. Szabados & D. Kurtz, 71–72
- Fuhrmann, K., Pfeiffer, M., Frank, C., Reetz, J., & Gehren, T. 1997, *A&A*, 323, 909
- Gilliland, R. L., McCullough, P. R., Nelan, E. P., et al. 2011, *ApJ*, 726, 2
- Gratton, R. G., Sneden, C., Carretta, E., & Bragaglia, A. 2000, *A&A*, 354, 169
- Grevesse, N., Asplund, M., Sauval, A. J., & Scott, P. 2010, *Ap&SS*, 328, 179
- Jørgensen, B. R. & Lindegren, L. 2005, *A&A*, 436, 127
- Kervella, P., Thévenin, F., Ségransan, D., et al. 2003, *A&A*, 404, 1087
- Kordopatis, G., Recio-Blanco, A., de Laverny, P., et al. 2011, *ArXiv e-prints*, 1109.6237
- Korn, A. J., Grundahl, F., Richard, O., et al. 2006, *Nature*, 442, 657
- Korn, A. J., Grundahl, F., Richard, O., et al. 2007, *ApJ*, 671, 402
- Korn, A. J., Shi, J., & Gehren, T. 2003, *A&A*, 407, 691
- Lebreton, Y. 2005, in *ESA Special Publication*, Vol. 576, *The Three-Dimensional Universe with Gaia*, ed. C. Turon, K. S. O'Flaherty, & M. A. C. Perryman, 493
- Lebreton, Y. 2008, in *IAU Symposium*, Vol. 248, *IAU Symposium*, ed. W. J. Jin, I. Platais, & M. A. C. Perryman, 411–416
- Lebreton, Y. 2011, *ArXiv e-prints*, 1108.6153

- Lebreton, Y., Fernandes, J., & Lejeune, T. 2001, *A&A*, 374, 540
- Lebreton, Y. & Montalbán, J. 2009, in *IAU Symposium*, Vol. 258, *IAU Symposium*, ed. E. E. Mamajek, D. R. Soderblom, & R. F. G. Wyse, 419–430
- Perryman, M. A. C., de Boer, K. S., Gilmore, G., et al. 2001, *A&A*, 369, 339
- Porto de Mello, G. F., Lyra, W., & Keller, G. R. 2008, *A&A*, 488, 653
- Pourbaix, D., Nidever, D., McCarthy, C., et al. 2002, *A&A*, 386, 280
- Re Fiorentin, P., Bailer-Jones, C. A. L., Lee, Y. S., et al. 2007, *A&A*, 467, 1373
- Recio-Blanco, A., Bijaoui, A., & de Laverny, P. 2006, *MNRAS*, 370, 141
- Richard, O., Michaud, G., & Richer, J. 2005, *ApJ*, 619, 538
- Sbordone, L., Bonifacio, P., Caffau, E., et al. 2010, *A&A*, 522, A26
- Spite, M., Bonifacio, P., Cayrel, R., et al. 2007, in *IAU Symposium*, Vol. 239, *IAU Symposium*, ed. F. Kupka, I. Roxburgh, & K. Chan, 280–285
- Turon, C., Luri, X., & Masana, E. 2012, in *The fundamental distance scale: state of the art and the Gaia perspectives*, ed. M. Marconi, G. Clementini & E. Brocato, *Astrophysics and Space Science Conference Series*, in press

**Atelier A03 commun ASGAIA-PNPS-PNCG-PCMI
SF2A-SEA**

**Stellar and Interstellar physics for the modelling of the
Galaxy and its components**

SF2A 2011
Paris, 20-21 juin 2011

Objectifs scientifiques

- Détermination des propriétés fondamentales des étoiles et du milieu interstellaire avec Gaia et les grands surveys pour la modélisation de la Galaxie.
- Détermination des paramètres atmosphériques, des abondances et de la cinématique des étoiles et contraintes sur les modèles galactiques.
- Contribution du milieu interstellaire aux quantités observées.

Comité scientifique

Catherine Turon (présidente), Frédéric Arenou, Misha Haywood, David Katz, Rosine Lallement, Xavier Luri, Alejandra Recio-Blanco, Céline Reylé, Jordi Torra.

Présentations invitées et contributions orales

Lundi 20 Juin - Amphithéâtre Bruxelles

Président de séance : Xavier Luri

- 14h00-14h25 **F. Mignard:** The Gaia mission: status and expected performance
- 14h25-14h50 **R. Ibata:** Constraining the merger history of the Milky Way and its neighbours
- 14h50-15h15 **F. Figueras et al.:** Kinematic imprints from the bar and spiral structures in the Galactic Disk
- 15h15-15h30 **M. Guittet et al.:** The Milky Way Stellar Populations in CFHTLS fields
- 15h30-15h45 **G. Kordopatis et al.:** Probing the thick disc formation scenarios outside the Solar neighborhood
- 15h45-16h00 **A. Robin et al.:** Simulating the Galaxy and applications to the preparation of the Gaia mission
- 16h00-16h30 *Coffee break*

Présidente de séance : Céline Reylé

- 16h30-16h55 **P. Di Matteo:** Chemodynamical modelling of the Galaxy
- 16h55-17h20 **X. Luri & C. Turon:** Luminosity calibrations and distances in the Galaxy and Local Group
- 17h20-17h45 **E. Moraux:** Stellar census and early dynamical evolution of open clusters
- 17h45-18h00 **H. Bouy et al.:** DANCE : Dynamical Analysis of Nearby ClustErs
- 18h15-18h15 **B. Rocca et al.:** Evolution of our Galaxy and others with the high-resolution version of the code PEGASE

Mardi 21 Juin - Amphithéâtre Bruxelles

Présidente de séance : Francesca Figueras

- 14h00-14h25 **C. Turon, F. Arenou & M. Haywood:** A.S. Gaia: 2007-2011 and perspectives
14h25-14h50 **C. Allende-Prieto:** Determination of stellar parameters and their uncertainties
14h50-15h15 **E. Caffau:** Perspective in detailed element abundance determination
15h15-15h30 **T. Decressin et al.:** Building part of the Galactic halo from globular clusters
15h30-15h45 **S. Dib et al.:** The dependence of the galactic star formation laws on metallicity
15h45-16h00 **P. Ocvirk & D. Aubert:** A signature of the internal reionisation of the Milky Way in the radial distribution of its satellites?

16h00-16h30 *Coffee break*

Présidente de séance : Christine Joblin

- 16h30-16h55 **A. Spielfieldel, N. Feautrier et al.:** Collision rates and the determination of atmospheric parameters
16h55-17h20 **D. Valls-Gabaud:** Stellar ages in the context of Gaia
17h20-17h45 **D. Marshall:** Towards a 3D view of the Galactic interstellar medium with Planck, Herschel and Gaia
17h45-18h00 **D. Paradis and the Hi-GAL team:** Galactic dust properties

THE GAIA MISSION: STATUS AND EXPECTED PERFORMANCE

F. Mignard¹

Abstract. The Gaia mission is in a very advanced state of preparation, with the integration of most of the spacecraft subsystems under-way in Toulouse, and a launch scheduled in 2013. Regarding the data processing, the European consortium DPAC is putting in place a massive system able to ingest and process the 40 GB of telemetry expected every day. I will summarise the current mission status and recall the major scientific objectives of the mission and the consolidated performance in astrometry, photometry and spectroscopy, together with an indication of a possible scenario for the release of the results, intermediate or final. I will also explain how the community at large is also preparing the arrival of this huge volume of accurate data, in particular by designing complementary ground based programs.

¹ Cassiopée, OCA, Nice, France

CONSTRAINING THE MERGER HISTORY OF THE MILKY WAY AND ITS NEIGHBOURS

R. Ibata¹

Abstract. Recent studies of the Milky Way and its neighbours in the Local Group have unveiled a complex network of accretion remnants. I will present some on-going surveys to understand these structures, as well as some very recent advances in modelling them, with the particular aim of trying to recover the probability distributions of possible orbits and the distribution of the dark matter. I will discuss our prospects of derive the merger history of nearby galaxies in the Gaia era.

¹ Observatoire de Strasbourg, France

KINEMATIC IMPRINTS FROM THE BAR AND SPIRAL STRUCTURES IN THE GALACTIC DISK

F. Figueras¹, T. Antoja², O. Valenzuela³, M. Romero-Gómez¹, B. Pichardo³ and E. Moreno³

Abstract. At 140 years of the discovery of the moving groups, these stellar streams are emerging as powerful tools to constrain the models for the spiral arms and the Galactic bar in the Gaia era. From the kinematic-age-metallicity analysis in the solar neighbourhood it is now well established that some of these kinematic structures have a dynamical origin, different from the classical cluster disruption hypothesis. Test particle simulations allow us to definitively establish that these local structures can be created by the dynamical resonances of material spiral arms and not exclusively by the Galactic bar. First studies to evaluate the capabilities of the future Gaia data to detect and characterize moving groups at 2-6 kpc from the solar neighborhood are discussed.

Keywords: Galaxy: kinematics and dynamics, solar neighbourhood, spiral structure, Galactic bar

1 Introduction

In the last two decades the study of the Milky Way (MW) has experienced outstanding progress owing to the advent of high-quality observations, better models and methods, and the use of powerful computation facilities (e.g. Turon et al. 2008). In particular, the solar neighbourhood has been studied in depth thanks to the stellar positions and velocities from the Hipparcos mission and its complementary photometric and spectroscopic on-ground surveys. The rich kinematics and stellar chemical distribution in the solar neighbourhood may constitute a set of imprints and fossils left after several Galactic processes. The observations have revealed very interesting properties, one of the most intriguing features being what now is usually called moving groups (MG). These are stellar streams, gravitationally unbound, occupying extended regions of the Galaxy which are seen as overdensities in the velocity space. At present, the origin of these kinematic structures is far from being completely understood although it is more than 140 years since they were discovered (see Antoja et al. 2010a, for a historical review).

Several scenarios to understand their origin and evolution have been proposed since then: 1) cluster and star complex disruption; 2) orbital and resonant effects of the non-axisymmetric structure of the MW (spiral arms and bar): periodic orbits, chaos, precession of periodic orbits, transient spiral structure; 3) tidal debris of past accretion events and, 4) external dynamical effects on the disk resulting from interaction events. A combination of some of these options becomes a complex but fascinating scenario. Here we will comment on the work our team has been undertaken in the last five years, that is, the characterization of what we observe in the solar neighbourhood, how test particle simulations show that MGs can be induced by the MW bar and spiral arms and how the Gaia satellite* will see them in the next decade.

2 What we observe

In Antoja et al. (2008) we applied the Wavelet Denoising technique to an extensive compendium of stars – more than 24000 – in the solar neighbourhood to characterize MGs in the U-V-age-[Fe/H] space. We confirm that the

¹ Dept. d'Astronomia i Meteorologia & Institut de Ciències del Cosmos, Universitat de Barcelona, Martí i Franquès 1, E-08028 Barcelona, Spain.

² Kapteyn Astronomical Institute, University of Groningen, PO Box 800, 9700 AV Groningen, the Netherlands.

³ Instituto de Astronomía, Universidad Nacional Autónoma de México, A.P. 70-264, 04510, México, D.F., México

*<http://sci.esa.int/science-e/www/area/index.cfm?fareaid=26>

dominant kinematic structures in the U-V plane are the branches of Sirius, Coma Berenices, Hyades-Pleiades and Hercules. They all present a negative slope of $\sim 16^\circ$ in the U-V plane. These branches are present in all spatial regions studied and, although our data was well constrained to the solar neighbourhood, we detected for the first time a slight dependence of the kinematic branches on Galactic position. These studies is being now taken up again with a much more extended sample around the Sun using the recently published 3th release of RAVE radial velocity survey (Antoja et al., in prep.).

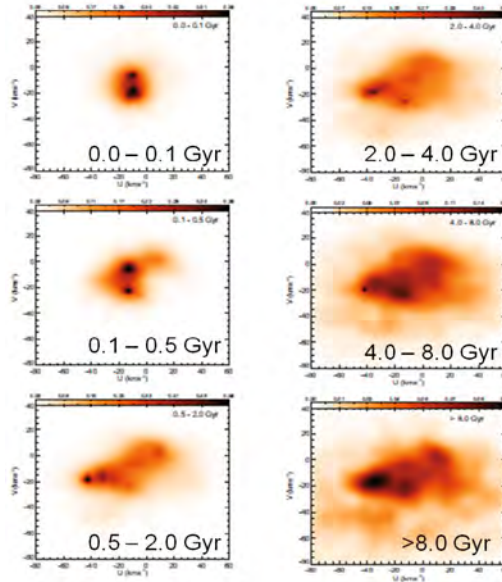


Fig. 1. Velocity distribution for different ages groups. See Antoja et al. (2008) for catalogue compilation.

From the Geneva Copenhagen Survey it is now well established that these kinematic branches have an extended age distribution (see Fig. 1). Even more, very promising recent spectroscopic studies have revealed that most groups are chemically inhomogeneous (Arcturus (Williams et al. 2009); Hercules (Bensby et al. 2007), among others). It is reasonable to think that the four scenarios mentioned above for the origin of MGs can coexist in the solar neighbourhood. HR1614 can be an example of a minor kinematic structure possibly originated from a cluster disruption; it has a low chemical and age scattering and, hence, it does seem to be remnant of a dispersed star-forming event (de Silva et al. 2007). But for sure, the observations available up to now show that many MGs, specially the above mentioned branches, have a large spread in ages and chemical composition indicating that, definitively, we shall rule out those models that propose that these kinematic structures are remnants of disk star clusters.

3 Moving groups induced by MW bar and spiral arms

We have performed numerical integrations of test particle orbits on the Galactic plane (2D), adopting the potential described in Antoja et al. (2011). There we have shown that studies with only spiral arms or only the bar are a valid way to understand the effects of each component in the velocity distribution, and eventually they could be used to constrain the characteristics of the bar and spiral arms.

3.1 Imprints from the Galactic bar

In Antoja et al. (2009) we show how the Galactic prolate bar (Pichardo et al. 2003), with a realistic orientation and density profile, triggers the already known bimodality in the velocity distribution (Kalnajs 1991). This is caused by a thin region of irregular orbits that are probably related to the bar 2:1 OLR. The central node of the bimodality is distorted through positive U. This distortion could be associated with the new observed group found at $(U, V) = (35, -20)$ km/s and with the elongation of the Coma Berenices branch. We also propose that the low angular momentum MGs, including Arcturus, could have two distinct viable origins related to the bar acting on a relatively hot stellar disk: 1) the dynamics of the bar could have a strong influence on the transient

kinematic groups at low angular momentum that are products of the ongoing phase mixing in an un-relaxed disk or 2) the bar also creates kinematic structures at low angular momentum that may be associated entirely with its induced resonant effects on the U-V plane. Bar resonances 3:1, 4:1 and 5:1 could be responsible for these kinematic groups at low angular momentum.

3.2 Imprints from the spiral arms

In Antoja et al. (2011) we studied the spiral arm influence on the solar neighbourhood stellar kinematics. We have seen that the spiral arms induce strong kinematic imprints in the solar neighbourhood for pattern speeds $\Omega_p \sim 15 - 19 \text{ km/s/kpc}$, close to the 4:1 inner resonance (see Fig. 2). No substructure is induced close to corotation or higher order resonances ($m > 6$) which, in the solar neighbourhood, corresponds to pattern speeds of $20 - 30 \text{ km/s/kpc}$.

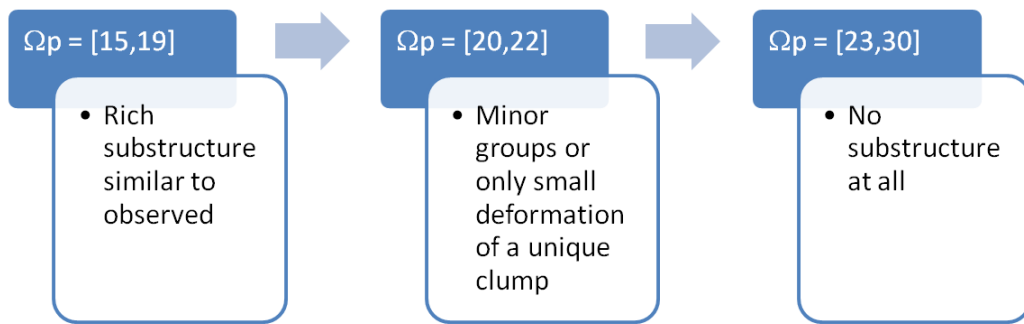


Fig. 2. Scheme of the relation between the MW pattern speed of the spiral arms and the existence of kinematic substructure in the solar neighbourhood.

We have observed that the velocity distribution is less sensitive to the relative spiral phase. More than 2 kpc in galactocentric azimuth are needed to detect a significant change in the velocity space. The strongest effects are detected near the arms. The effects of spiral arm density contrast has been also investigated. We observe that a higher density contrast increases the dispersion but maintains the geometry of the kinematic substructure, so concluding that the strength of the MW spiral pattern will be a parameter difficult to constrain using MGs.

4 Future Gaia capabilities

We can identify several scientific challenges for the coming years as far as MGs are concerned. A combination of chemical tagging, improved large-scale Galactic dynamics studies and cosmological simulations applied to the MW are required in order to disentangle the origin of the kinematic structures in the Galactic disk. New theoretical and observational strategies to approach the problem are needed in preparation for the upcoming Gaia and complementary surveys. A first attempt to evaluate how far Gaia will go in providing precise 3D velocity distributions was presented in Antoja et al. (2010b). We analyzed two regions, the Scutum Centaurus tangency $(l, b) = (305^\circ, 0^\circ)$ at $\sim 7 \text{ kpc}$ and the Perseus arm at the anticenter direction, at $\sim 2 \text{ kpc}$. Working in the space of the observables we confirm that the unprecedented Gaia accuracy in proper motions will allow to clearly identify the rich kinematic substructure in the Perseus arm at $\sim 2 \text{ kpc}$ from the Sun. That is Gaia errors hardly change or hide the kinematic structure obtained from our test particle simulations in this region. Concerning the detection of kinematic substructure in the Scutum Centaurus tangency, K giants in this far region will have a relative error in Gaia parallax of $\sim 60\%$, therefore IR photometric distances will be required. Looking again in the observable plane of radial velocities and proper motions, we checked that errors in radial velocity not larger than $2 - 3 \text{ km/s}$ are needed to detect the rich resonant kinematic structure in this region. The study of the phase space in those regions is critical to understand the kinematic behaviour and nature of the spiral pattern.

5 Conclusions

Our analysis of the observational sample and the test particle simulations indicates that it is very feasible that some of the MGs observed in the solar neighbourhood have a dynamical origin related with the effects induced by the spiral arms and the bar. However, several improvements are needed in order to definitively characterize the chemistry and the evolutionary state of the different kinematic groups. This is a statistical study which requires a large number of stars with accurate ages and chemical composition. Data from Multi-Object Spectrographs currently available and/or in preparation are promising for the analysis of chemical inhomogeneities in the kinematic groups. More complex is the derivation of accurate stellar ages, where large errors are present. Future Gaia data will require complementary age determinations from new tools like asteroseismology (Poretti et al. 2011) or stellar chronology with white dwarfs in wide binary systems (Garces et al. 2012), among others.

From our test particle studies we can confirm that MW spiral arms in the range of the observed spiral arms parameters favour the triggering of kinematics groups such as the ones observed in the solar neighbourhood. But can we at present constrain the spiral arms using the MGs? Our analysis demonstrates that groups such as the observed ones in the solar vicinity can be reproduced by different combinations of parameters, i.e. a degeneracy is present. Thus, data from velocity distributions at larger distances are needed for a definitive constraint. Work is in progress to map the evolution of these MGs at large scale on the Galactic disk both from test particle and N-body simulations.

Preliminary analysis of Gaia capabilities confirm that the stellar streams are emerging as powerful tools to constrain the models for the spiral arms and the Galactic bar in the Gaia era. It is mandatory to analyze carefully our modelled velocity distributions at large scale in the Galactic disk so as to find strategic places where the kinematic structures are particularly rich to discriminate among models and to constrain the spiral arm and the Galactic bar parameter space.

We acknowledge funding support from MICINN (Spanish Ministry of Science and Innovation) - FEDER through grant AYA2009-14648-C02-01 and CONSOLIDER CSD2007-00050, the European Research Council under ERC-StG grant GALACTICA-24027, Some of the simulations were run at the HP CP 4000 cluster (KanBalam) in the DGSCA/UNAM.

References

- Antoja, T., Figueras, F., Fernández, D., Torra, J., 2008, *A&A*, 490, 135
- Antoja, T., Valenzuela, O., Pichardo, B., Moreno, E., Figueras, F., Fernández, D., 2009, *ApJ*, 700, L78
- Antoja, T., Figueras, F., Torra, J., Valenzuela, O., Pichardo, B., 2010, *LNEA*, 4, 13
- Antoja, T., Figueras, F., Monguió, M., 2011, *EAS*, 45, 309
- Antoja, T., Figueras, F., Valenzuela, O. et al. 2011, *MNRAS*, arXiv:1106.1170
- Antoja, T., 2011, in “Kinematic groups across the MW disk: insights from models and from the RAVE catalogue” , proceedings of *Assembling the Puzzle of the Milky Way*, Editors: Céline Reylé, Annie Robin and Mathias Schultheis, *European Physical Journal*.
- Bensby, T., Oey, M. S., Feltzing, S., Gustafsson, B., 2007, *ApJ*, 655, L89
- De Silva, G. M., Freeman, K. C., Bland-Hawthorn, J., Asplund, M., Bessell, M. S., *AJ*, 133, 694
- Garces, A., Catalán, S., Ribas, I. <http://xxx.unizar.es/abs/1105.0287>
- Kalnajns, A.J., 1991, *Dynamics of Disk Galaxies*, ed. B. Sundelius, 323
- Pichardo, B., Martos, M., Moreno, E., Espresate, J., 2003, *ApJ*, 582, 230
- Poretti et al., 2011, <http://xxx.unizar.es/abs/1102.3085>
- Turon, C., Primas, F., Binney, J., et al., 2008, Report N. 4, ESA-ESO working Group, *Galactic Populations, Chemistry and Dynamics* vii, 3
- Williams, M. E. K., Freeman, K. C., Helmi, A., the RAVE collaboration, 2009, in “The Arcturus Moving Group: Its Place in the Galaxy” *The Galaxy Disk in Cosmological Context*, Proceedings of the International Astronomical Union, IAU Symposium, Volume 254. Edited by J. Andersen, J. Bland-Hawthorn, and B. Nordström, p. 139-144

THE MILKY WAY STELLAR POPULATIONS IN CFHTLS FIELDS

M. Guittet¹, M. Haywood¹ and M. Schultheis²

Abstract. We investigate the characteristics of the thick disk in the Canada – France – Hawaii – Telescope Legacy Survey (CFHTLS) fields, complemented at bright magnitudes with Sloan Digital Sky Survey (SDSS) data. The $([\text{Fe}/\text{H}], Z)$ distributions are derived in the W1 and W3 fields, and compared with simulated maps produced using the Besançon model. It is shown that the thick disk, represented in star-count models by a distinct component, is not an adequate description of the observed $([\text{Fe}/\text{H}], Z)$ distributions in these fields.

Keywords: the Galaxy, the thick disk, $[\text{Fe}/\text{H}]$ abundance.

1 Introduction

Our knowledge of the characteristics of the thick disk remains limited in practically every aspects. Its structure on large scales ($> \text{kpc}$) is not well defined, either clumpy or smooth, and its connections with the collapsed part of the halo or the old thin disk are essentially not understood. The spectrum of possible scenarios proposed to explain its formation is still very large and really discriminant constraints are rare. The SDSS photometric survey has provided a wealth of new informations on the thick disk, see in particular Ivezić et al. (2008), Bond et al. (2010) and Lee et al. (2011). However, the data have barely been directly confronted to star-count models, and little insights have been given on how the thick disk in these models really represents the survey data. In the present work, we initiate such comparisons by comparing the Besançon model with metallicity and distance information in the W1 and W3 CFHTLS fields, and provide a brief discussion of our results.

2 Data description

Among the four fields that make the Wide Survey, W1 and W3 cover larger angular surfaces (72 and 49 square degrees) than W2 and W4 (both having 25 square degrees). They point towards higher latitudes (-61.24° and 58.39° respectively) and are consequently less affected by dust extinction, and contain a larger relative proportion of thick disk stars. We will therefore focus on W1 and W3. CFHTLS photometry starts at a substantially fainter magnitude than the SDSS, missing a large part of the thick disk. We complemented the CFHTLS catalogue at the bright end with stars from the SDSS not present in the CFHTLS fields. In the final catalogues, W1 contains $\sim 139\,000$ stars, with 16% from the SDSS, while $\sim 132\,000$ stars are found in W3 field, with 31% coming from the Sloan.

W1 and W3 are at large distances above the galactic plane. The dust extinction is very small at these latitudes. For example the Schlegel map (Schlegel et al. 1998) estimates for W1 an absorption coefficient A_v of 0.087 while Jones et al. (2011) give $A_v=0.113$. The extinction models of Arenou et al. (1992) or Hakkila et al. (1997) estimate A_v values to 0.1 and 0.054 respectively. We briefly discuss the effect of extinction on distance determination and metallicities in 4.1.

¹ GEPI, Observatoire de Paris, CNRS, Université Paris Diderot; 5 Place Jules Janssen, 92190 Meudon, France

² Observatoire de Besançon; 41 bis, avenue de l'Observatoire, 25000 Besançon, France

3 Comparisons between the Besançon model and CFHTLS/SDSS data: Hess diagrams

3.1 The Besançon model

Simulations were made using the Besançon model (Robin et al. (2003), Haywood et al. (1997), Bienayme et al. (1987)) online version. The model includes four populations: the bulge, the thin disk, the thick disk and the halo. The metallicities of the thick disk and the halo in the online version of the model (-0.78 and -1.78 dex respectively) were shifted (to -0.6 dex and -1.5 dex) to comply with more generally accepted values, and in particular with values derived from the Sloan data (see Lee et al. (2011), who shows that the thick disk have a metallicity $[Fe/H] = -0.6$ dex roughly independent of vertical distances, and (Ivezić et al. (2008), Bond et al. (2010), Sesar et al. (2011), Carollo et al. (2010) or de Jong et al. (2010) for the inner halo metallicity, estimated to be about -1.5 dex). The thick disk has a scale height of 800 pc and a local stellar density ρ_0 of 6.8 % of the local thin disk, while the stellar halo is described by a power law with a flattening and a local density of 0.6%. Simulations were made assuming photometric errors as described in the SDSS.

3.2 Hess diagrams

The distributions of CFHTLS/SDSS and model stars in the g versus $u-g$ color magnitude diagram (CMD) are shown in Fig. 1. For both diagrams, faint blue stars ($u-g \sim 0.9$, $g > 18$) are clearly discernible and correspond to the galactic halo. The concentration of stars at $g < 18$, $u-g \sim 1.1$, corresponds to disk stars and in particular thick disk stars. Because of the SDSS saturation at $g=14$ which does not allow to have a representative sample of thin disk stars, our data sample is mainly composed of thick disk and halo stars. The Besançon model shows a distinct separation between thin disk stars ($u-g \sim 1.3$, $g < 14-15$) and thick disk stars ($u-g \sim 1.1$, $15 < g < 18$) which cannot be checked with the present data.

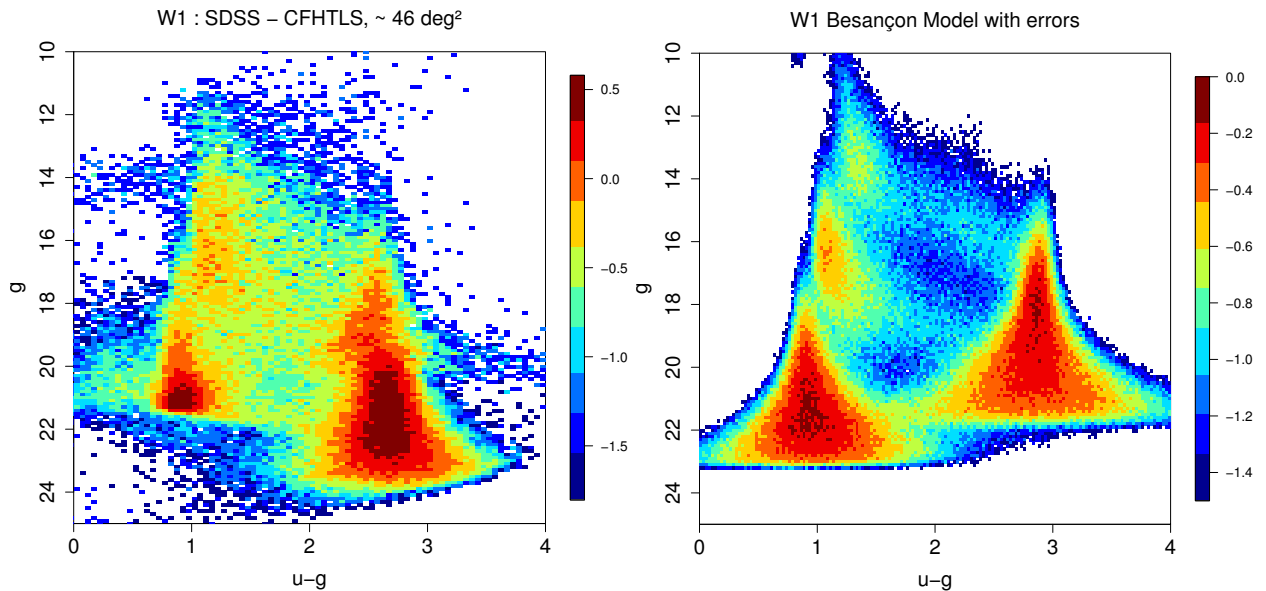


Fig. 1. Left: CFHTLS/SDSS $u-g$ Hess diagram in W1 field. **Right:** The same as the left graphic but for the Besançon model stars to which observational errors from SDSS data have been added. The successive ridge lines due to the thin disk, thick disk and the halo main sequence stars are clearly distinguishable between $0.7 < u-g < 1.5$.

4 Comparisons between the Besançon model and CFHTLS/SDSS data: ([Fe/H], Z) distributions

4.1 Metallicity and photometric distance determinations

Jurić et al. (2008) and Ivezić et al. (2008) have published calibrations of the metallicity and photometric parallax as a function of $ugri$ magnitudes. The metallicity calibration has been revised in Bond et al. (2010) :

$$[\text{Fe}/\text{H}] = A + Bx + Cy + Dxy + Ex^2 + Fy^2 + Gx^2y + Hxy^2 + Ix^3 + Jy^3 \quad (4.1)$$

where $x = u - g$, $y = g - r$ and $(A-J) = (-13.13, 14.09, 28.04, -5.51, -5.90, -58.58, 9.14, -20.61, 0.0, 58.20)$. This relation has been determined for F and G stars and is consequently applicable in the range : $0.2 < g - r < 0.6$ and $-0.25 + 0.5(u - g) < g - r < 0.05 + 0.5(u - g)$. This calibration only extends to -0.2 dex. Observed vertical distances Z have been calculated using $Z = D \sin(b)$, b being the latitude of the star. Photometric distances D , such as $m_r - M_r = 5 \log(D) - 5$, were determined using the absolute magnitude calibration of Ivezić et al. (2008) which depends on the metallicity and on $g - i$ colors.

For the highest extinction values given by Jones et al. (2011), the impact on metallicities, as can be estimated using Eq. 4.1 and the absolute magnitude relation of Ivezić et al. (2008) are at most of 0.15 dex near $g-r=0.5$ at solar metallicities and 0.1 dex at $[\text{Fe}/\text{H}] = -1$ dex. Distances will be affected at most by about 20% at solar metallicities and 15% at $[\text{Fe}/\text{H}] = -1$ dex at $g-r$ near 0.40-0.45.

4.2 ([Fe/H], Z) distributions

We generated catalogues with the model in the direction of W1 and W3, deriving the Z height above the plane from simulated distances and metallicities from the assumed metallicity distributions of each population. In Fig. 2 we present $([\text{Fe}/\text{H}], Z)$ distributions for both the data and the model. The dotted line is the median metallicity per bin of 0.5 kpc. The continuous line is the median metallicity for disk stars as shown by Bond et al. (2010) and follows rather well the disk distribution in our data. We find similar results as Bond et al. (2010) : the halo dominates the star counts above 3 kpc with a mean metallicity of about -1.5 dex. Sesar et al. (2011) studied the four CFHTLS Wide fields but with magnitudes corrected for ISM extinction. They found the mean halo metallicity in the range between -1.4 and -1.6 dex. Our estimate of the extinction effect would shift metallicities to about 0.15 dex at most, and shows that our mean halo metallicity is in good agreement with their estimates.

The interesting point worth of notice is the conspicuous, distinct, pattern that represents the thick disk in the model and which clearly is absent in the data. As expected, the standard thick disk model dominates the counts between 1 and 4 kpc, while in the data, the thick disk seems to be less extended, and does not appear as a distinct component between the thin disk and the halo. The vertical resolution of the observed distribution prevents any clear statement concerning the transition from the thin to thick disk, although it is apparent that the model is at variance with the data. This result raises the interesting question of the connections (or lack of) between the thin and thick disks. Almost since its discovery, it has been suggested that the thick disk is more akin to an extended thin disk (Norris 1987). Our knowledge of the thick disk more than twenty years later does not permit us to draw any firm conclusion on that point.

5 Conclusion

Investigation of the $([\text{Fe}/\text{H}], Z)$ distribution in the CFHTLS Wide fields does not seem to show a thick disc component as prominent and distinct as predicted by standard star-count models. The mean halo metallicity found to be -1.5 dex is in agreement with previous studies (e.g Bond et al. (2010), Sesar et al. (2011)). The behavior of models must be studied on more extensive data sets in order to assess the necessary adjustments and to better characterize the thick disk.

References

- Arenou, F., Grenon, M., & Gomez, A. 1992, *A&A*, 258, 104
 Bienayme, O., Robin, A. C., & Creze, M. 1987, *A&A*, 180, 94
 Bond, N. A., Ivezić, Ž., Sesar, B., et al. 2010, *ApJ*, 716, 1

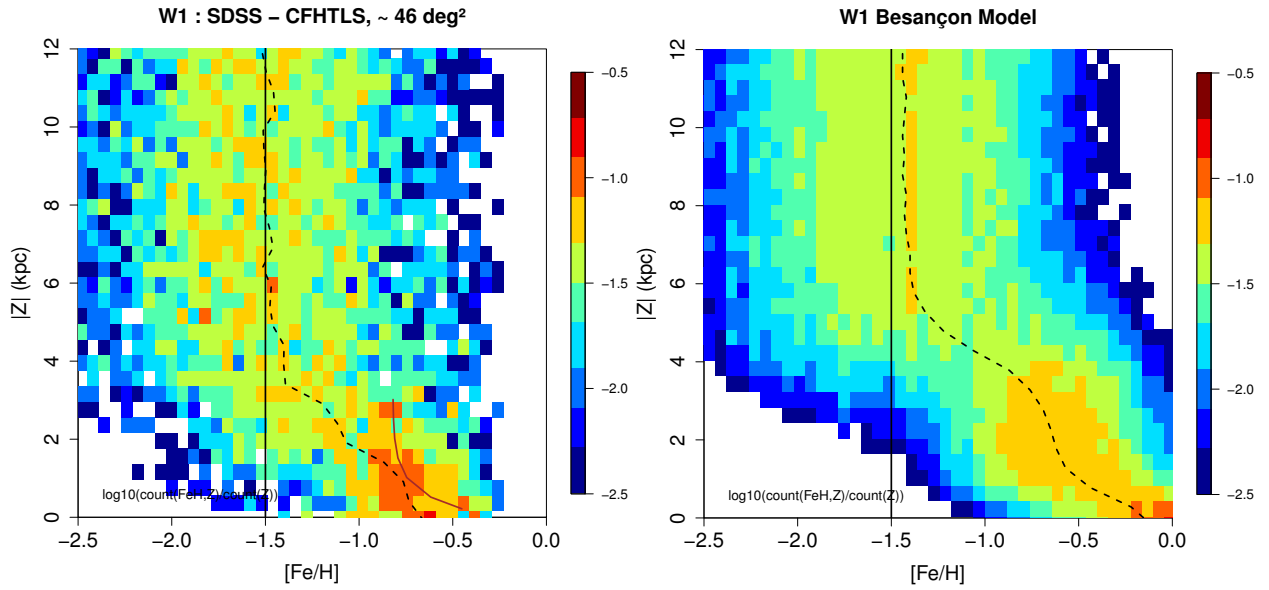


Fig. 2. Left: $([Fe/H], Z)$ distribution for CFHTLS/SDSS data in W1 field. **Right:** Besançon model $([Fe/H], Z)$ distribution in W1 field. The continuous line on the left plot shows the median metallicity formula (A2) derived by Bond et al. (2010). The dotted line represents the median metallicity per bin of 0.5 kpc.

- Carollo, D., Beers, T. C., Chiba, M., et al. 2010, *ApJ*, 712, 692
 de Jong, J. T. A., Yanny, B., Rix, H.-W., et al. 2010, *ApJ*, 714, 663
 Hakkila, J., Myers, J. M., Stidham, B. J., & Hartmann, D. H. 1997, *AJ*, 114, 2043
 Haywood, M., Robin, A. C., & Creze, M. 1997, *A&A*, 320, 428
 Ivezić, Ž., Sesar, B., Jurić, M., et al. 2008, *ApJ*, 684, 287
 Jones, D. O., West, A. A., & Foster, J. B. 2011, *AJ*, 142, 44
 Jurić, M., Ivezić, Ž., Brooks, A., et al. 2008, *ApJ*, 673, 864
 Lee, Y. S., Beers, T. C., An, D., et al. 2011, *ApJ*, 738, 187
 Norris, J. 1987, *ApJ*, 314, L39
 Robin, A. C., Reylé, C., Derrière, S., & Picaud, S. 2003, *A&A*, 409, 523
 Schlegel, D. J., Finkbeiner, D. P., & Davis, M. 1998, *ApJ*, 500, 525
 Sesar, B., Jurić, M., & Ivezić, Ž. 2011, *ApJ*, 731, 4

PROBING THE THICK DISC FORMATION SCENARIOS OUTSIDE THE SOLAR NEIGHBOURHOOD

G. Kordopatis¹, A. Recio-Blanco¹, P. de Laverny¹, G. Gilmore², V. Hill¹, R. F. G. Wyse³, A. Helmi⁴, A. Bijaoui¹, C. Ordenovic¹, M. Zoccali⁵ and O. Bienaymé⁶

Abstract. The origin and evolution of the Milky Way remains one of the key unanswered questions in astrophysics. From a sample of roughly 700 stars selected in order to probe the galactic thick disc outside the solar neighborhood, we investigate the radial scale length and scale height of this structure, based on the spectroscopic measurement of its star members. Estimations of the scale height and scale lengths for different metallicity bins result in consistent values, with $h_R \sim 3.4 \pm 0.7$ kpc and $h_Z \sim 694 \pm 45$ pc, showing no evidence of relics of destroyed massive satellites and challenging the radial migration mechanisms as being the most important processes of creation of the thick disc.

Keywords: Galaxy: evolution – Galaxy: kinematics and dynamics – stars: abundances – methods: observational

1 Introduction

The existence of a thick disc for the Milky Way (Gilmore & Reid 1983), and for other disc galaxies (Yoachim & Dalcanton 2006) is rather clearly established nowadays. Nevertheless, its creation mechanisms still remain a riddle in the paradigm of a cold dark matter dominated Universe. For instance, Abadi et al. (2003) propose that the stars forming the thick disc mostly come from disrupted satellites, whereas Villalobos & Helmi (2008) predict that the pre-existing thin disc has been heated rapidly from successive accretions. On the other hand, Brook et al. (2004) suggest that a gas rich merger brought the necessary gas to form *in situ* the thick disc stars, before the gas have had completely settled into a thin disc. Finally, the simulations of Schönrich & Binney (2009) manage to form a thick disc without any external stimulus: stars migrate to larger heights from the inner parts of the Galaxy, due to resonances with the spiral arms and the central bar.

Typical F, G and K main sequence stars are particularly useful to study galactic evolution, since they are both numerous and long-lived, and their atmospheres reflect their initial chemical composition. However, a direct measurement of their spatial distribution requires accurate estimates of stellar distances, which is a delicate step involving (if the parallax is not available) the determination of precise stellar parameters (effective temperatures T_{eff} , surface gravities $\log g$, and metal content $[M/H]$).

In order to put more constraints on the thick disc properties, we explore spectroscopically the stellar contents outside the solar neighborhood, owing to an extensive use of the Ojha et al. (1996) catalogue in which are published the proper motions (μ_l , μ_b) and U,B,V colors of several thousand stars. Here, based on the spectroscopic observations of 700 of these stars towards the galactic coordinates $l \sim 277^\circ$, $b \sim 47^\circ$, we present a kinematic and chemical characterization of the thick disc.

¹ Université de Nice Sophia Antipolis, CNRS, Observatoire de la Côte d’Azur, Cassiopée UMR 6202, BP 4229, 06304 Nice, France

² Institute of Astronomy, University of Cambridge, Madingley Road, Cambridge CB3 0HA, UK

³ Johns Hopkins University, Baltimore, MD, USA

⁴ Kapteyn Astronomical Institute, University of Groningen, PO Box 800, 9700 AV Groningen, The Netherlands

⁵ Departamento de Astronomía y Astrofísica, Pontificia Universidad Católica de Chile, Av. Vicuña Mackenna 4860, Casilla 306, Santiago 22, Chile

⁶ Université de Strasbourg, Observatoire Astronomique, Strasbourg, France

2 The star sample

The target stars were selected having $14 \leq m_V \leq 18.5$ mag in order to probe the galactic thick disc and an acceptable signal-to-noise ratio ($S/N > 20$). According to the published values of Ojha et al. (1996), the magnitude precisions range from 0.02 mag for the brightest, to 0.05 mag for the faintest stars. Associated errors for the proper motions are estimated to be 2 mas/year.

The observations were obtained with VLT/FLAMES feeding the GIRAFFE spectrograph with the LR08 grating (8206-9400 Å, $R \sim 6500$). This setup contains the Gaia/RVS wavelength range (8475-8745 Å), and is similar to its low-resolution mode. In that wavelength range, the IR CaII triplet is predominant for most of the spectral types and luminosity classes as well as for very metal-poor stars. In addition, these strong features are still detectable even at low S/N, allowing a good radial velocity (V_{rad}) derivation and, combined with the other available lines, a good overall metallicity estimation.

Radial velocities have been derived by cross-correlating the spectra with a binary template of a K0 type star, reaching a mean estimated error of 4.7 km s^{-1} . We used the pipeline presented in Kordopatis et al. (2011a) to obtain the T_{eff} , $\log g$ and $[M/H]$ for our sample. This pipeline combines a local multi-linear regression method, MATISSE (Recio-Blanco et al. 2006), and an oblique decision-tree, DEGAS (Bijaoui et al. 2010) in order to normalize iteratively the spectra and derive accurately the stellar atmospheric parameters. The method has been tested on a set of 8×10^4 synthetic spectra, in order to establish the relative errors of our algorithm on the effects of the S/N and possible radial velocity shifts. We found that for an intermediate metallicity dwarf star, at $S/N \sim 50 \text{ pixel}^{-1}$ (which is the mean S/N of our spectra), accuracies of $\sim 108 \text{ K}$, 0.17 dex and 0.12 dex are achieved for T_{eff} , $\log g$ and $[M/H]$, respectively. In addition, the algorithm has been applied on two observed stellar libraries, the S^4N (Allende Prieto et al. 2004) and the CFLIB one (Valdes et al. 2004), showing no particular biases according to the S/N, the spectral type of the star or the metallic content.

2.1 Derivation of the stellar distances and velocities

At least until the ESA/Gaia mission, stellar distances for FGK targets far from the solar neighborhood have to be determined spectroscopically or photometrically. For instance, the atmospheric parameters determined in the previous section can be projected on a set of theoretical isochrones to derive the absolute magnitudes of the stars. Then, the line-of-sight distances can be derived, using the distance modulus.

We generated our own set of isochrones by using the *YYmix2* interpolation code, based on the Yonsei-Yale models (version 2, Demarque et al. 2004) combined with the Lejeune et al. (1998) colour table. To obtain the absolute magnitude M_V , the method of Zwitter et al. (2010) was used. This procedure consists in finding the most likely values of the stellar parameters, given the measured atmospheric ones, and the time spent by a star on each region of the H–R diagram.

The availability of the distances (D) then allows to estimate their galactic-centred cylindrical coordinates, which, combined with proper motions and radial velocities, provide the information required to calculate the full space motions of any star in the Galaxy. For our sample, the radial velocities are derived from the observed spectra, whereas magnitudes, colors and proper motions are taken from Ojha et al. (1996).

The errors on these kinematic data are estimated as follows: for each star, we make 5×10^3 Monte-Carlo realisations for D , μ_l , μ_b and V_{rad} , assuming Gaussian distributions around their adopted values, with a dispersion according to their estimated errors. For every realization, 6d phase-space parameters are computed, taking as a final value the mean of all the realisations, and as an error the standard deviation (see Kordopatis et al. 2011b).

3 Derivation of the radial scale lengths and scale heights

In what follows, we considered as thin disc the stars below 800 pc from the galactic plane, and as thick disc the stars between 1 and 3 kpc, in order to avoid a strong contamination from the other components. Supposing that the thick disc and the thin disc are in equilibrium, the velocity ellipsoids that were derived (corrected from the observational errors as in Jones & Walker 1988), can be used with the Jeans equation in order to infer an estimation of their radial scale lengths (h_R) and scale heights (h_Z). In cylindrical coordinates, the radial and azimuthal components of the Jeans equation are:

$$v_c^2 - \overline{v_\phi}^2 = \sigma_{V_R}^2 \left(\frac{\sigma_{V_\phi}^2}{\sigma_{V_R}^2} - 1 - \frac{\partial \ln(\rho \sigma_{V_R}^2)}{\partial \ln R} - \frac{r}{\sigma_{V_R}^2} \frac{\partial \sigma_{V_{R,Z}}^2}{\partial Z} \right) \quad (3.1)$$

$$\rho K_Z = \frac{\partial \rho \sigma_{V_Z}^2}{\partial Z} + \frac{1}{R} \frac{\partial R \rho \sigma_{V_{R,Z}}^2}{\partial R} \quad (3.2)$$

where ρ is the density of the considered galactic component, $V_c = 220 \text{ km s}^{-1}$ is the circular velocity at the solar radius, $\overline{V_\phi}$ is the mean rotational velocity of the stars having the $\sigma_{V_R}, \sigma_{V_\phi}, \sigma_{V_Z}$ velocity dispersions, $\sigma_{V_{R,Z}}^2 = \overline{V_R V_Z} - \overline{V_R} \overline{V_Z}$, and K_Z is the vertical galactic acceleration.

3.1 Radial scale lengths

We consider that $\rho(R) \propto \exp(-R/h_R)$, and that $\sigma_{V_R}^2$ has the same radial dependence as ρ (as in Carollo et al. 2010). Therefore, $\sigma_{V_R}^2 \propto \exp(-R/h_R)$. In addition, one can assume that the galactic potential is dominated by a centrally concentrated mass distribution and that the local velocity ellipsoid points towards the galactic centre (Gilmore et al. 1989; Siebert et al. 2008). In that case, the last term of Eq. 3.1 becomes:

$$\frac{r}{\sigma_{V_R}^2} \frac{\partial \sigma_{V_{R,Z}}^2}{\partial Z} \approx 1 - \frac{\sigma_{V_Z}^2}{\sigma_{V_R}^2} \quad (3.3)$$

Equation 3.1 can then be re-written as follows:

$$\frac{\sigma_{V_\phi}^2}{\sigma_{V_R}^2} - 2 + \frac{2R}{h_R} - \frac{v_c^2 - \overline{v_\phi}^2}{\sigma_{V_R}^2} + \frac{\sigma_{V_Z}^2}{\sigma_{V_R}^2} = 0 \quad (3.4)$$

Each of the terms of Eq. 3.4 have been measured in our data, leaving as the only free variable, the radial scale length h_R of the discs. With the values derived for the thick disc of $(\sigma_{V_R}; \sigma_{V_\phi}; \overline{V_\phi}) = (66 \pm 5; 57 \pm 4; -167 \pm 3) \text{ km s}^{-1}$, we find $h_R \sim 3.4 \pm 0.7 \text{ kpc}$. This results is found to be the upper end of the values cited in the literature (ranging from 2.2 kpc (Carollo et al. 2010) up to 3.6 kpc (Jurić et al. 2008), or even 4.5 kpc in the case of Chiba & Beers (2001)).

As far as the thin disc is concerned, using $(\sigma_{V_R}; \sigma_{V_\phi}; \overline{V_\phi}) = (43 \pm 2; 33 \pm 1; -204 \pm 1) \text{ km s}^{-1}$, we find that it has a smaller, though comparable radial extent (within our uncertainties) as the thick disc, with $h_R = 2.9 \pm 0.2 \text{ kpc}$. A smaller thin disc has been suggested by other recent observations (see Jurić et al. 2008), but once more, the value we derive is at the upper end of the previously reported values in the literature. Nevertheless, such an extended thin disc is plausible, since our data probe mainly the old thin disc, which is likely to be more extended than its younger part.

3.2 Scale heights

We assume that the last term of Eq. 3.2 is negligible, since we are far from the galactic centre, and that $\rho(Z) \propto \exp(-Z/h_Z)$. Equation 3.2 hence becomes:

$$\frac{\partial \ln \sigma_{V_Z}^2}{\partial Z} - \frac{1}{h_Z} + \frac{K_Z}{\sigma_{V_Z}^2} = 0 \quad (3.5)$$

We use $K_Z = 2\pi G \times 71 M_\odot \text{ pc}^{-2}$ derived by Kuijken & Gilmore (1991) at $|Z| = 1.1 \text{ kpc}$, but we note however, that this value of K_Z might differ at the distances where our targets are observed. We also use for the thick disc the value derived from our data of $\partial \sigma_{V_Z}^2 / \partial Z = 15 \pm 7 \text{ km s}^{-1} \text{ kpc}^{-1}$ and $\sigma_{V_Z} = 53 \pm 3 \text{ km s}^{-1}$. Hence, for the thick disc, we find $h_Z \sim 694 \pm 45 \text{ pc}$.

As far as the thin disc is concerned, we found that $\partial \sigma_{V_Z}^2 / \partial Z = 19 \pm 10 \text{ km s}^{-1} \text{ kpc}^{-1}$ and $\sigma_{V_Z} = 25 \pm 1 \text{ km s}^{-1}$, resulting in $h_Z = 216 \pm 13 \text{ pc}$. The derived values for both components are in good agreement with, for example, Jurić et al. (2008), who suggested a thin disc with $h_Z = 300 \text{ pc}$, and a thick disc having $h_Z = 900 \text{ pc}$.

4 Discussion

We computed the radial scale lengths and scale heights of the thick disc for different metallicity bins, using Eq. 3.4 and Eq. 3.5. The results are shown in Table 1, where the metallicity bins have been selected in order to include at least 30 stars each. Though we found that both h_R and h_Z increased with decreasing metallicity (except for the most metal poor bin), this trend is not strong enough to stand out significantly from the errors. We conclude that, within the errors, the same scale lengths and scale heights are found, which could be the

Table 1. Kinematic parameters, radial scale lengths and scale heights for different metallicity bins of the thick disc targets.

| $[M/H]$ (dex) | N | $\overline{V_R}$ (km s ⁻¹) | σ_{V_R} (km s ⁻¹) | $\overline{V_\phi}$ (km s ⁻¹) | σ_{V_ϕ} (km s ⁻¹) | $\overline{V_Z}$ (km s ⁻¹) | σ_{V_Z} (km s ⁻¹) | h_R (kpc) | h_Z (pc) |
|------------------|----|---|---|--|--|---|---|----------------|---------------|
| -1.14 | 36 | -5± 9 | 58± 11 | -137± 11 | 61± 7 | -7± 8 | 59± 7 | 1.9± 0.7 | 934± 166 |
| -0.67 | 26 | -3± 17 | 85± 17 | -161± 11 | 54± 11 | -4± 12 | 54± 8 | 4.0± 1.3 | 804± 181 |
| -0.40 | 56 | 5± 8 | 81± 8 | -168± 6 | 52± 5 | -17± 6 | 45± 4 | 3.8± 0.9 | 610± 90 |
| -0.11 | 37 | 6± 9 | 64± 8 | -171± 7 | 50± 6 | -18± 7 | 45± 5 | 3.1± 0.9 | 620± 97 |

signature of only one population. Indeed, if an important amount of relics of a destroyed massive satellite would exist in our line-of-sight, as suggested by Gilmore et al. (2002), one would expect them to have a different spatial distribution compared to the canonical thick disc, which we do not observe. Unless, of course, the satellite debris provides the dominant stellar population in the thick disc.

This result can also be discussed in the frame of a thick disc formed according to a radial migration scenario. In that case, the older stars being at the solar radius have come from the inner parts of the Galaxy, and are expected to have a higher vertical velocity dispersion and a different metallicity, and therefore, should exhibit scale heights dependent on metallicity. In particular, the model of Schönrich & Binney (2009) predicts a smaller scale height for the metal poor thick disc, compared to its metal rich counter part. Such a trend is not seen in our data (if it exists, it should be rather small), which challenges the migration scenario as being the most important process of creation of the galactic thick disc.

The authors would like to thank the MESOCENTRE de l'Observatoire de la Cote d'Azur, for computing the grid of synthetic spectra. We are grateful to B. Plez for his molecular line-lists and M. Irwin for letting us use the routine of sky subtraction. Finally, G.K. would like to thank the Centre National d'Etudes Spatiales (CNES) and the Centre National de Recherche Scientifique (CNRS) for the financial support.

References

- Abadi, M. G., Navarro, J. F., Steinmetz, M., & Eke, V. R. 2003, *ApJ*, 591, 499
- Allende Prieto, C., Barklem, P. S., Lambert, D. L., & Cunha, K. 2004, *A&A*, 420, 183
- Bijaoui, A., Recio-Blanco, A., de Laverny, P., & Ordenovic, C. 2010, in *ADA 6 - Sixth Conference on Astronomical Data Analysis*
- Brook, C. B., Kawata, D., Gibson, B. K., & Freeman, K. C. 2004, *ApJ*, 612, 894
- Carollo, D., Beers, T. C., Chiba, M., et al. 2010, *ApJ*, 712, 692
- Chiba, M. & Beers, T. C. 2001, *ApJ*, 549, 325
- Demarque, P., Woo, J.-H., Kim, Y.-C., & Yi, S. K. 2004, *ApJS*, 155, 667
- Gilmore, G. & Reid, N. 1983, *MNRAS*, 202, 1025
- Gilmore, G., Wyse, R. F. G., & Kuijken, K. 1989, *ARA&A*, 27, 555
- Gilmore, G., Wyse, R. F. G., & Norris, J. E. 2002, *ApJ*, 574, L39
- Jones, B. F. & Walker, M. F. 1988, *AJ*, 95, 1755
- Jurić, M., Ivezić, Ž., Brooks, A., et al. 2008, *ApJ*, 673, 864
- Kordopatis, G., Recio-Blanco, A., de Laverny, P., et al. 2011a, *ArXiv:1109.6237*
- Kordopatis, G., Recio-Blanco, A., de Laverny, P., et al. 2011b, *A&A*, submitted, *arXiv:1110.5221*
- Kuijken, K. & Gilmore, G. 1991, *ApJ*, 367, L9
- Lejeune, T., Cuisinier, F., & Buser, R. 1998, *A&AS*, 130, 65
- Ojha, D. K., Bienayme, O., Robin, A. C., Creze, M., & Mohan, V. 1996, *A&A*, 311, 456
- Recio-Blanco, A., Bijaoui, A., & de Laverny, P. 2006, *MNRAS*, 370, 141
- Schönrich, R. & Binney, J. 2009, *MNRAS*, 399, 1145
- Siebert, A., Bienaymé, O., Binney, J., et al. 2008, *MNRAS*, 391, 793
- Valdes, F., Gupta, R., Rose, J. A., Singh, H. P., & Bell, D. J. 2004, *ApJS*, 152, 251
- Villalobos, Á. & Helmi, A. 2008, *MNRAS*, 391, 1806
- Yoachim, P. & Dalcanton, J. J. 2006, *AJ*, 131, 226
- Zwitter, T., Matijević, G., Breddels, M. A., et al. 2010, *A&A*, 522, A54

SIMULATING THE GALAXY AND APPLICATIONS TO THE PREPARATION OF THE GAIA MISSION

A. C. Robin¹, C. Reylé¹, CU2 and Gaia-DPAC consortium

Abstract. The preparation of the Gaia mission requires simulations of the stellar content of the Galaxy with detailed estimates of the intrinsic properties of the stars, as well as the overall structure of the Galaxy. We present a few distribution in luminosity class and spectral type of the stars visible by Gaia instruments and a new development of the model concerning the populations in the Galactic bulge.

Keywords: Galaxy:stellar content, Galaxy:evolution, Galaxy:structure

1 Introduction

The Gaia mission will give a detailed view, with unprecedented accuracy, of the stellar content of the Galaxy. It will encompass any model that we can make at the time being. However models are still useful to prepare the mission, for providing simulations of the intermediate and final catalogues of the mission, to test algorithms in good conditions before launch, and to provide testbeds for the data analysis methods. In order to achieve Gaia simulations, a coordination unit (CU2) has been established inside the Gaia Data Processing and Analysis Consortium (Gaia-DPAC) in order to provide to other members of the consortium the necessary simulations. CU2 has to implement the simulators which are three at this time : GIBIS, generating images, GASS, generating telemetry data, and GOG for intermediate and final catalogues simulations. All three simulators use two models to simulate the data : the Universe Model and the Instrument Model. One important aspect of the Universe Model concern the stellar content of the Milky Way, which will provide more than 90% of the sources in the Gaia instrument.

CU2 has chosen to base its Galaxy model on the Besançon Galaxy Model (Robin et al. 2003). However the DPAC needed more detailed simulations than in this standard model and improvements have been introduced in the scheme, like the simulation of binary and multiple stars, intrinsic and extrinsic (microlensing) stellar variabilities, simulations of extended objects (HII regions, planetary nebulae) and varying backgrounds (zodiacal light), as well as stars with exoplanets. An overall description of the Universe model can be found in Robin et al. (2011a).

The Gaia simulators have been used to estimate the number of stars of different kinds which are expected in the Gaia telescopes. Examples of these numbers are given here. These numbers are still subject to change before launch because our knowledge evolves and we shall attempt to introduce as much as reality as possible in the simulations in order that people trying to exploit the data can rely on it. The typical usages of these simulations are to test the softwares, in particular the classification schemes, that can be very sensitive to the frequency of the type of objects to classify.

In this paper we summarize the typical star count expectations in the Gaia instruments. In Sect. 2 we present the way the Galaxy stellar content is simulated for the Gaia preparation. In Sect. 3, we show estimations of the numbers and properties of stars that Gaia will see. And in Section 4 we show on-going work for improving the modelling of the Galaxy in the bulge region.

¹ Institut Utinam, CNRS UMR6213, Université de Franche-Comté, Observatoire de Besançon, Besançon, France

Table 1. Number of stars of each luminosity class over 1/8th of the sky up to limiting magnitude $G \leq 20$ and $G_{RVS} \leq 12$. Level 0 concerns single stars only. Level 1 is for objects in star systems with at least two components.

| Luminosity class | $G \leq 20$ | | | $G_{RVS} \leq 12$ | | |
|------------------|-------------|----------|----------|-------------------|---------|---------|
| | Level 0 | Level 1 | Total | Level 0 | Level 1 | Total |
| Supergiants | 14 | 32 | 46 | 14 | 32 | 46 |
| Bright giants | 15653 | 54492 | 70145 | 6595 | 21443 | 28038 |
| Giants | 1832214 | 3236786 | 5069000 | 220641 | 538672 | 759313 |
| Subgiants | 3253211 | 4526679 | 7779890 | 60142 | 114217 | 174359 |
| Main Sequence | 33223926 | 33752099 | 66976025 | 118576 | 189104 | 307680 |
| PreMain sequence | 41616 | 42429 | 84045 | 3067 | 5619 | 8686 |
| White dwarfs | 29140 | 59881 | 89021 | 7 | 3832 | 3839 |
| Total | 38395774 | 41672398 | 80068172 | 409042 | 872919 | 1281961 |

2 Modelling what Gaia will see

The Universe Model developed for the simulation of the mission is a set of algorithms for computing the positions at any time and observational properties of any objects expected to be observed by the Gaia instruments.

The distributions of these objects and the statistics of observables should be as realistic as possible for simulations to be usable for estimating telemetry, testing software, simulating images, etc. The algorithms have to be optimised in order that the simulations can be performed in reasonable time and can be redone when necessary. The complexity of the model increases with time during the preparation of the mission. The numbers presented here have been obtained from the cycle 10 version of the simulator (2011).

Simulated objects are: solar system objects (planets, satellites, asteroids, comets), Galactic objects (stars, nebulae, stellar clusters, diffuse light), extragalactic objects (galaxies resolved in stars, unresolved but extended galaxies, quasars and active galactic nuclei, supernovae). For each of these simulated objects one needs to have their full 3D spatial distribution together with their spectral characteristics (to be able to compute photometry and spectroscopy, stable or variable in time), and their motions (for astrometric computations and for spectral corrections).

In order to simulate the sky content, the sky is subdivided in small regions with a Hierarchical Triangular Mesh (HTM, see <http://skyserver.org/htm/>). The Universe Model presently uses the 3D extinction model from Drimmel & Spergel (2011). A complete description of the Universe Model used for Gaia simulations can be found in Robin et al. (2011a).

3 Estimations of the stellar content in the Gaia mission

From the Universe Model and from the generators of the final catalog (GOG) it is possible to evaluate the number of each kind of astronomical sources that Gaia will see. We here give a few numbers from a simulation of 1/8th of the sky with version 10 of the simulator. It concerns only stars in the Galaxy, excluding stars in neighbourhood galaxies and other astronomical sources. More up to date numbers for the whole sky will be presented in a forth coming paper (Robin et al., in prep). Table 1 gives the number of stars of each luminosity class and Table 2 the distribution in spectral type. The numbers are given for each hierarchy level. Level 0 concerns single stars only. Level 1 is for objects in star system with at least two components. Numbers are given for two limiting magnitude. At $G < 20$, the stars will have photometry and astrometry measured. At $G_{RVS} \leq 12$, stars will have very accurate radial velocity and abundance measurements from the spectrograph RVS. At the limiting magnitude of the RVS (between 16 and 17 depending on the spectral type) stars will have a rough estimate of the radial velocity and a metallicity index but no elemental abundances.

4 Recent model improvements : the bulge/bar population

Continuing our efforts to improve the realism of the model, and to find constraints on the formation scenario for each of the galactic components, we have turned our eyes towards the bulge/bar region to find out whether it is possible to deduce such constraints from large surveys. The first step is to establish the distribution of the light in 3D from analysis of 2MASS near infrared star counts. The mass distribution will be straightforwardly

Table 2. Number of stars of each spectral type over 1/8th of the sky up to limiting magnitude $G=20$, to $G_{RVS}=17$, and $G_{RVS}=12$. Level 0 concerns single stars only. Level 1 is for objects in star system with at least two components. L dwarf counts are included only up to L5.

| Sp. Type | $G \leq 20$ | | | $G_{RVS} \leq 17$ | | | $G_{RVS} \leq 12$ | | |
|----------|-------------|----------|----------|-------------------|----------|----------|-------------------|---------|---------|
| | Level 0 | Level 1 | Total | Level 0 | Level 1 | Total | Level 0 | Level 1 | Total |
| O | 0 | 5 | 5 | 0 | 5 | 5 | 0 | 5 | 5 |
| B | 22957 | 88754 | 111711 | 16358 | 77367 | 93725 | 2681 | 15250 | 17931 |
| A | 424842 | 1186894 | 1611736 | 331214 | 963217 | 1294431 | 20679 | 66433 | 87112 |
| F | 7490020 | 9580207 | 17070227 | 3415861 | 5038394 | 8454255 | 80922 | 159564 | 240486 |
| G | 12864111 | 14079527 | 26943638 | 5153553 | 6186141 | 11339694 | 91053 | 170381 | 261434 |
| K | 12086280 | 12183767 | 24270047 | 4179879 | 4964899 | 9144778 | 176810 | 408939 | 585749 |
| M | 5477126 | 4480471 | 9957597 | 1549717 | 1324498 | 2874215 | 36211 | 45288 | 81499 |
| L | 12 | 12 | 24 | 4 | 7 | 11 | 0 | 0 | 0 |
| AGB | 516 | 361 | 877 | 503 | 346 | 849 | 426 | 271 | 697 |
| Other | 29910 | 72400 | 102310 | 1682 | 21028 | 22710 | 260 | 6788 | 7048 |
| Total | 38395774 | 41672398 | 80068172 | 14648771 | 18575902 | 33224673 | 409042 | 872919 | 1281961 |

deduced from it. Further, metallicities and kinematics can be attached to each population to understand the chemo-dynamical history of its formation. For doing so, we extended the approach made by Picaud & Robin (2004) to a wider area of the bulge ($-20^\circ < l < 20^\circ$ and $-10^\circ < b < 10^\circ$). A Monte-Carlo scheme is used to explore the multidimensional space of model parameters. These model parameters are the density function of the bulge population (a triaxial Ferrer ellipsoid defined by 3 scale lengths, 3 orientation angles, 2 parameters for the boxyness, a normalisation factor, and a cutoff radius), plus 2 parameters for the thin disc, which is a really important population in the plane towards the bulge. The thin disc is parametrized by a Einasto (1979) density law, with a scale length, and a scale length for the inner hole, as in Robin et al. (2003). The following equations give the shapes of the fitted bulge population which have been tested : $\rho_S = \rho_0 \operatorname{sech}^2(-R_s)$ or $\rho_E = \rho_0 \exp(-R_s)$ or $\rho_G = \rho_0 \exp(-R_s)^2$ with

$$R_s^{C_\parallel} = \left[\left| \frac{X}{x_0} \right|^{C_\perp} + \left| \frac{Y}{y_0} \right|^{C_\perp} \right]^{C_\parallel/C_\perp} + \left| \frac{Z}{z_0} \right|^{C_\parallel} \quad (4.1)$$

where (X,Y, Z) are the cartesian coordinates in the referential of the triaxial structure (X being the major axis, Y the second axis and the Z the third). The parameters C_\parallel and C_\perp are important to explore a wide range of shapes, from diskly to boxy. This allows a great flexibility : one can even have a diskly shape in the plane, together with a boxy projection vertically.

The counts are simulated assuming a bulge population of age 8 Ga from Padova isochrones Girardi et al (2002) for different metallicities. The age is not a very sensitive parameters in star counts from broad band photometry. For the simulation we use the Marshall et al (2006) 3D extinction model. The simulated counts are compared with observed counts in bins in the space ($K, J-K$) and a likelihood is computed. While attempting to fit a unique bulge population with a single shape, we realized that the resulting fit was not satisfactory in all the studied region. We then attempted to fit the population with the sum of two ellipsoids and find out a much better global fit over the whole bulge region. The counts and residuals from the data, and from the simulated counts for the 1-ellipsoid model and from the best fit model are given in Figure 1. We clearly see that the best 1-ellipsoid fit does not reproduce enough the boxyness of the bulge region, while the 2-ellipsoid model does.

5 Conclusions and further developments

The Gaia simulator using a Universe Model is able to predict the counts and the properties of the objects that Gaia will see during its mission. The total number will be about 1 billion of stars. This number depends on assumptions in the model, particularly on the assumed binary fraction and on the 3D extinction map. More detailed predictions will be provided in a forthcoming paper (Robin et al., in prep).

In parallel to providing simulations from the standard Galactic model, we attempt to improve the model and particularly towards the bulge region. We presented a new model which reproduces the 2MASS star counts in the region $-20^\circ < l < 20^\circ$ and $-10^\circ < b < 10^\circ$. This model is made of the sum of two Ferrer's ellipsoids, the first

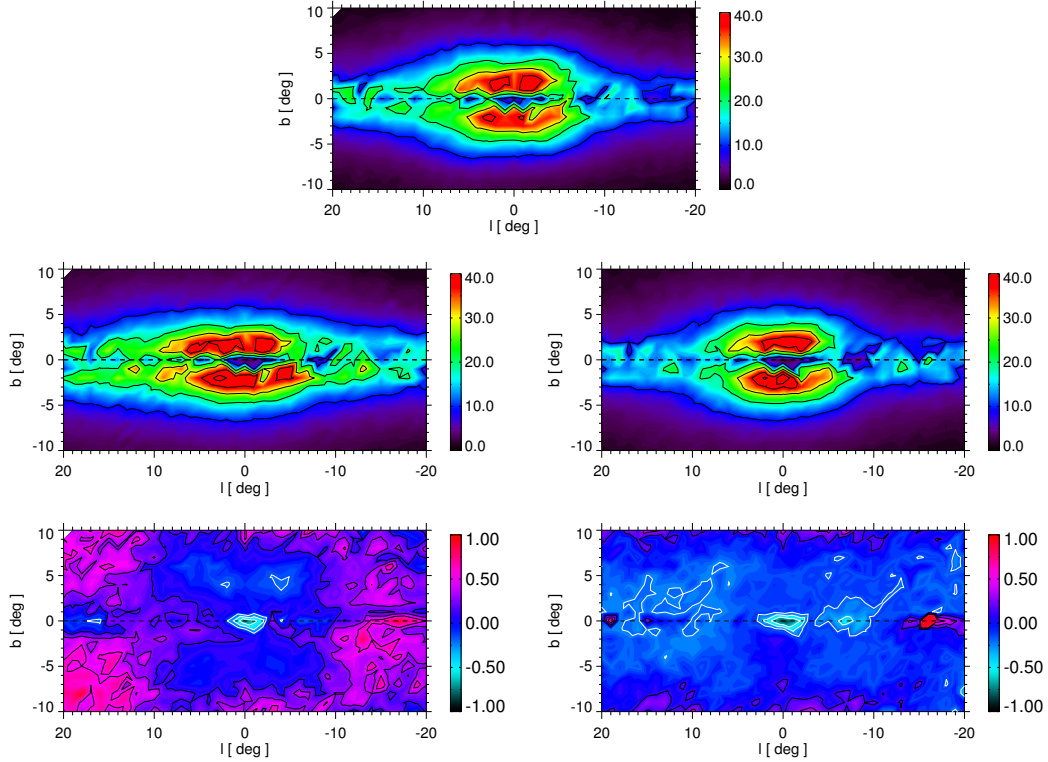


Fig. 1. Star counts up to limiting magnitude K_S from 2MASS data (top) compared with fitted 1 ellipsoid model (middle left), residuals $(N_{mod}-N_{obs})/N_{obs}$ (bottom left), 2-ellipsoids model (middle right) and its residuals (bottom right). In the residual map, contours are drawn at intervals of 20% model overestimate (black) and 20% model underestimate (white). Near the Galactic centre the nuclear bar population is missing in the model and thus appears in the residuals.

ellipsoid having a major axis pointing with an angle of about 13° with the sun-center axis and the scale lengths are 1.46/0.49/0.39 kpc. The second component is less massive (about 4% of the first one) and has larger scale lengths 4.44/1.31/0.80 kpc, but significantly contributes at medium latitudes. The agreement between this new models in terms of colour magnitude diagrams is very good. We also show that assuming that the first ellipsoid is inhabited by a population of solar metallicity and the second ellipsoid is a population of metallicity of -0.35 dex, we can very well reproduce the metallicity gradient which is found in Zoccali et al. (2008) along the minor axis of the bulge. From a preliminary comparison with kinematical data, we find out that the main component is the Galactic bar, and the second component can be either a classical bulge, or a population made from relics of merging, possibly related to the inner thick disc. The complete analysis and discussion can be found in Robin et al. (2011b).

References

- Drimmel, R. and Spergel, D. N., 2001, ApJ 556, 181
 Einasto J., 1979, IAU Symp. 84, The Large Scale Characteristics of the Galaxy, ed. W.B. Burton, p. x
 Ferrers, N. M., 1877, Quart. J. Pure Appl. Math., 14, 1
 Girardi, L., Bertelli, G., Bressan, A., Chiosi, C., Groenewegen, M.A.T., Marigo, P., Salasnich, B., Weiss, A. 2002, A&A, 391, 195
 Marshall D. J., Robin A. C., Reylé C., Schultheis M., Picaud S., 2006, A&A, 453, 635
 Picaud, S., Robin, A.C., 2004, A&A 428, 891
 Robin, A.C., Reylé, C., Arenou, F., et al, 2011, Gaia livelink GAIA-C2-TN-LAOB-AR-004-10
 Robin, A.C., Reylé, C., Derrière, S., Picaud S. 2003, A&A, 409, 523
 Robin, A.C, Marshall, D.J., Schultheis, M., Reylé, C., 2011, A&A, submitted
 Zoccali, M., Hill, V., Lecureur, A., Barbuy, B., Renzini, A., Minniti, D., Gómez, A., Ortolani, S. 2008, A&A, 486, 177

CHEMODYNAMICAL MODELLING OF THE GALAXY

P. Di Matteo¹

Abstract. We are entering a new era in the study of our Galaxy. Current and future surveys (like Gaia) will enlarge significantly the horizon we know, from few hundreds of parsecs (the so called "solar neighborhood") to a global vision of the Milky Way, up to tens of kiloparsecs from the Sun. The large amount of data soon available requires to be interpreted at the galactic scale, through models that have to take into account the complex interplay between dynamical and chemical processes, between secular evolution and the role of the environment.

In this talk I will review the most recent results N-body simulations have achieved in the effort to understand the formation of the different galactic components, discussing some possible directions for future models, to be robustly compared to the Gaia data.

¹ GEPI-UMR CNRS 8111, Observatoire de Paris, 92190 Meudon, France

GAIA: LUMINOSITY CALIBRATIONS AND DISTANCES IN THE GALAXY AND LOCAL GROUP

X. Luri¹ and C. Turon²

Abstract. The upcoming availability of the Gaia mission data will prompt a significant advancement in many areas of astrophysics and will specially have a huge impact in the determination of luminosity calibration and distances, thanks to the availability of very precise parallaxes.

Already the Hipparcos mission made a huge improvement in these areas with respect to the previous eras, but the advent of Gaia will represent an even larger improvement: the Gaia catalogue will contain about a billion objects, with more than 100 million of them with distances known to better than 10%, all over the Galaxy. All stellar distance indicators will be directly measured in very large number, providing a direct calibration of their luminosity and making possible detailed studies of the impacts of various effects linked to chemical element abundances or cluster membership. Furthermore, Gaia astrometry will be precise enough to reach the Large and Small Magellanic Clouds, allowing for the first time a direct parallax estimation of its distances.

In this paper we will review with the help of simulations the potential contributions of Gaia in these areas.

Keywords: Gaia, astrometry, luminosity calibration, distance scale

1 Introduction

The ESA Gaia astrometric mission has been designed for solving one of the most difficult yet deeply fundamental challenges in modern astronomy: to create an extraordinarily precise 3D map of about a billion stars throughout our Galaxy and beyond (Perryman et al. 2001).

The survey aims for completeness to $V_{lim} \sim 20-25mag$ depending on the color of the object, with astrometric accuracies of about $10\mu as$ at $15mag$ (see figure 1). In the process, it will map the stellar motion and provide the detailed physical properties of each star observed: characterizing their luminosity, temperature, gravity and elemental composition.

Additionally, it will perform the detection and orbital classification of tens of thousands of extra-solar planetary systems, and a comprehensive survey of some $10^5 - 10^6$ minor bodies in our solar system; furthermore, it will also include galaxies in the nearby Universe and distant quasars.

This massive stellar census will provide the basic observational data to tackle an enormous range of important problems related to the origin, structure and evolutionary history of our Galaxy and new tests of general relativity and cosmology, and in particular will make a substantial contribution to the determination of luminosity calibrations and the distance scale.

2 The Gaia simulator

Gaia will acquire an enormous quantity of complex and extremely precise data that will be transmitted daily to a ground station. By the end of Gaia's operational life, around 150 terabytes (10^{14} bytes) will have been transmitted to Earth: some 1,000 times the raw volume from the related Hipparcos mission.

¹ Dept. Astronomia i Meteorologia, Universitat de Barcelona, ICCUB/IEEC, 08028 Barcelona, Spain, xluri@am.ub.es

² GEPI - UMR 8111, Observatoire de Paris, CNRS, Université Paris Diderot, 5 Place Jules Janssen, 92190 Meudon, France, catherine.turon@obspm.fr

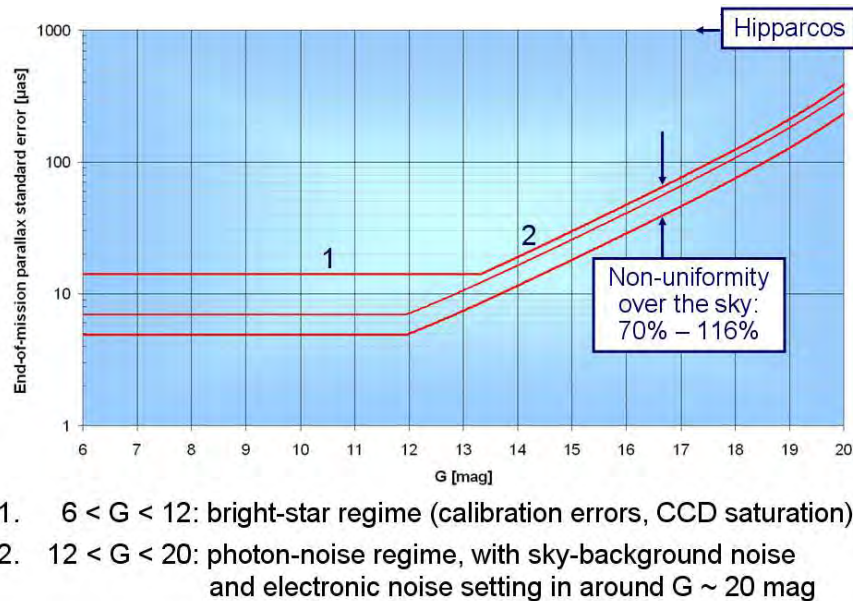


Fig. 1. End of life Gaia parallax errors (courtesy J. de Bruijne, ESA)

An extensive and sophisticated Gaia data processing mechanism is being developed to yield meaningful results from collected data. To allow its development and testing a system has been developed to generate the simulated Gaia data, the Gaia simulator.

The Gaia simulator has been organized around a common tool box (named GaiaSimu library) containing a universe model, an instrument model and other utilities, such as numerical methods and astronomical tools. This common tool box is used by several specialized components and one of its main components is the so-called Universe Model. It allows the simulation of the characteristics of all the different types of objects that Gaia will observe: their spatial distribution, photometry, kinematics and spectra. The universe model is designed to generate lists of astronomical sources whose distributions and the statistics of its observables are as realistic as possible.

The object generation process is divided into three main modules, Solar System, the Milky Way and extra-galactic objects. We will not deal here with the first and third modules and we present below a short summary of the second. For more details see (Robin et al. 2011).

2.1 The galaxy model

Galactic objects are generated from a model based on Besançon Galaxy Model (BGM) (Robin et al. 2003) which provides the distribution of the stars, their intrinsic parameters and their motions. The stellar population synthesis combines:

- Theoretical considerations such as stellar evolution, galactic evolution and dynamics.
- Observational facts such as the local luminosity function, the age-velocity dispersion relation, the age-metallicity relation.

The result is a comprehensive description of the stellar components of the Galaxy with their physical characteristics (e.g. temperature, mass, gravity, chemical composition and motions).

The Galaxy model is formed by four stellar populations constructed with different model parameters:

- The thin disc: young stars with high metallicities. It is additionally divided in seven isothermal components of ages varying from 0-0.15 Gyr for the youngest to 7-10 Gyr for the oldest. For computing the

scale height at the solar position as a function of age (Bienaymé et al. 1987), the Boltzmann equation (first moment at the first order with the plane parallel approximation) is used assuming an age-velocity dispersion relation deduced from Hipparcos observations (Gómez et al. 1997).

- The thick disc: in terms of metallicity, stars are at half-way between the thin disc and the stellar halo.
- The stellar halo (spheroid): old and metal poor stars.
- The outer bulge: old stars with metallicities similar to the ones in the thick disc.

The distribution in the Hess diagram split into several age bins is obtained from an evolutionary model which starts with a mass of gas, generates stars of different masses assuming an Initial Mass Function and a star formation rate history, and makes these stars evolve along evolutionary tracks. The evolution model is described in Haywood et al. (1997a,b). The evolutionary model produces a file describing the distribution of stars per element volume in the space (M_V, T_{eff}, Age). Similar Hess diagrams are also produced for the bulge, the thick disc and the spheroid populations, assuming a single burst of star formation and ages of 10 Gyr, 11 Gyr and 14 Gyr respectively.

The stellar luminosity function is the one of primary stars (single stars, or primary stars in multiple systems) in the solar neighborhood Reid et al. (2002).

It is worth noting that white dwarf (WD) are taken into account separately but self-consistently. Additionally, some rare objects such as Be stars, peculiar metallicity stars and Wolf Rayet stars have also been added.

In the end, each star from the generated catalogue has assigned intrinsic attributes (age, effective temperature, bolometric magnitude, U,V,W velocities, distance) and observational parameters (apparent magnitudes, colors, proper motions, radial velocities, etc) affected by the implemented 3D extinction model from Drimmel et al. (2003).

3 Simulation overview

The universe model generates a total number of 1,000,000,000 galactic objects at $G < 20$ of which 49% are single stars and 51% stellar systems formed by stars with planets and binary/multiple stars. Individually, the model has created 1,600,000,000 stars where 31.66% of them are single stars with magnitude G inferior to 20 (potentially observable by Gaia) and 68.34% correspond to stars in multiple systems. This last group is formed by stars that have magnitude G inferior to 20 as a system but, in some cases, its isolated components can have magnitude G superior to 20 and will not be individually detectable by Gaia.

3.1 Spatial distribution

Based on these simulations, the Gaia catalogue will sample a large fraction of the galactic volume, thoroughly mapping the solar neighborhood, providing large numbers of objects for a substantial part of the disk and reaching the central parts of the Galaxy although not the centre itself. In figure 2 the sampling of the Galaxy is depicted based on the simulation results.

3.2 The HR diagram

On the other hand, the stars in the catalogue will also fully cover the HR diagram, sampling even the regions with the rarest types of objects. This coverage is depicted in figure 3; the densest regions contain tens of millions of objects and even the rarest types (bottom of the main sequence, brightest giants) are represented with some hundreds of objects.

4 Consequences for the Luminosity calibrations and distance scale

Even though Hipparcos was a major improvement with respect to earlier ground-based astrometric observations, *only* about 30 000 stars (compared to a few hundreds before Hipparcos) obtained a relative precision on the trigonometric parallax better than 10 %, all of them are in the solar neighborhood, and very few standard candles are among them. On the other hand, many different photometric and spectroscopic systems have been used, resulting in the non-uniformity of the color or abundances scales, and have been compared with many different

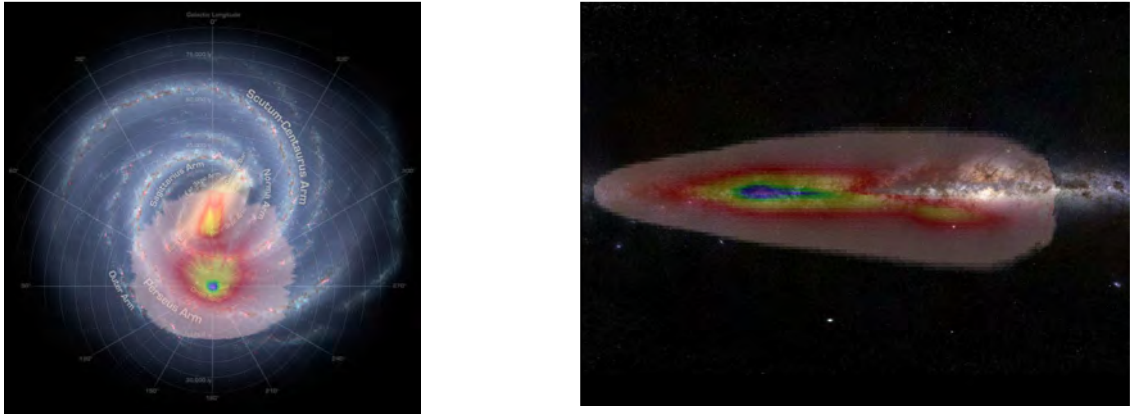


Fig. 2. These images show the expected 3D distribution in the Milky Way of the contents of the Gaia catalogue. They are an overlay of an artistic top view of our galaxy (NASA/JPL-Caltech/R. Hurt) and an illustration of a side view of the Galaxy (right, Gigagalaxy zoom, ESO/S. Brunier/S. Guisard: the Milky Way as seen from ESO, Chile) with the results of a simulation of the contents of the Gaia catalogue. The colors of the overlaid simulation show the expected density of the one-billion stars in the catalogue in different regions of the Milky Way, ranging from purple-blue very high densities around the Sun to pink low densities farther from it. The “spikes” pointing away from the Sun are due to windows in the interstellar extinction, allowing deeper observations. Notice in particular the region in yellow and red, just below the galactic center. It corresponds to the high-density bulge visible through an extinction window around the galactic central region. See http://www.rssd.esa.int/index.php?project=GAIA&page=picture_of_the_week&pow=141 for the full-resolution images.

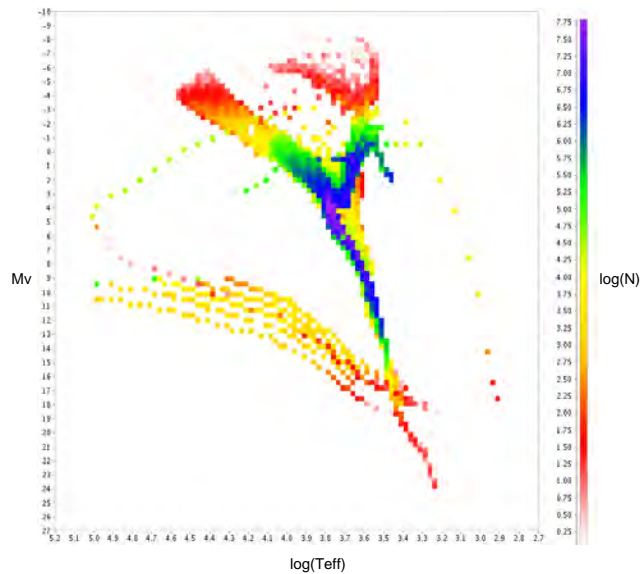


Fig. 3. The Gaia HR diagram. The figure shows the expected density of catalogue objects in the different regions of the HR diagram (single stars and components of systems alike). The color scale gives the decimal logarithm of the number of objects for each $[0.025K \times 0.37mag]$ box in the diagram; to properly interpret this figure it is important to take into account that the logarithmic scale strongly enhances the visibility of low-density areas that will be represented in the Gaia catalogue, which makes it somewhat unfamiliar compared with the usual HR diagrams.

models of stellar atmosphere, resulting in various transformations from color to the effective temperature and various estimations of the bolometric correction. Finally, it is difficult to safely compare observations between

Table 1. Luminosity calibrations: from Hipparcos to Gaia (adapted from Turon & Perryman 1999, and updated)

| | Hipparcos (a) | Hipparcos re-reduction (b) | GAIA |
|--|---|-------------------------------|--|
| $\sigma_\pi/\pi < 0.1\%$ | - | 3 | $\sim 100\,000$ stars |
| $\sigma_\pi/\pi < 1\%$ | 442 stars | 719 stars | $\sim 11 \times 10^6$ stars up to 1 – 2 kpc ($M_v < 0$) up to 0.5– 1 kpc ($M_v < 5$) |
| $\sigma_\pi/\pi < 10\%$ | 22 396 stars | 30 579 stars | $\sim 150 \times 10^6$ stars up to 10–15 kpc ($M_v < -5$) up to 7–10 kpc ($M_v < 0$) up to 2– 3 kpc ($M_v < 5$) |
| Error on M_v ($V = 10$) due to error on π | 0.5 mag at 100 pc | | 0.002-0.007 mag at 100 pc 0.2-0.7 mag at 10 kpc |
| Stellar populations | mainly disk | | all populations, even the rarest |
| HR diagram $< 10\%$ | $-4 < M_v < 13$ $-0.2 < B - V < 1.7$ | | all magnitudes all colors |

(a)(Perryman et al. 1997; Perryman & ESA 1997)

(b)(van Leeuwen & Fantino 2005; van Leeuwen 2007)

themselves and with theoretical isochrones.

The remaining major sources of uncertainty are the location of the principal sequences of the Hertzsprung-Russell diagram (main sequence, subgiant branch, turn-off stars, red clump stars, blue supergiants) versus metallicity, age or detailed element abundances, the calibration of the period-luminosity(-color) relations of pulsating variable stars with respect to all effects likely to affect their absolute luminosity, the distance (and depth) of the Large Magellanic Cloud, whose Cepheids are often used as reference to derive relative distances to other galaxies.

As we have seen in the previous section the Gaia catalogue will abundantly cover all the above mentioned regions of the HR diagram, and will do it with much more precise astrometry than Hipparcos, as shown in table 1.

Therefore, a huge amount of extremely accurate trigonometric parallaxes will be available for very large samples of all galactic populations, allowing the direct distance determination of large samples of all kinds of stellar candles, and may even provide the first direct test of the universality of the period-luminosity(-color) relations. It will also provide a systematic diagnostic of the duplicity (multiplicity) of all observed targets and reliable abundances and ages for very large samples of field and cluster stars.

Furthermore, Gaia will also observe about 7.5 million stars in the Large Magellanic Cloud and about 1.5 million stars in the Small Magellanic Cloud. Although most of the individual parallaxes will have too large errors to be useful to determine the distance of the individual stars (see figure 4) taking all the millions of individual parallaxes together will allow to determine the mean parallax of the LMC with a relative error of about 0.5%, and that of the SMC with a relative error of about 1.5%. Even more, for the brightest objects in the clouds (including Cepheids) the Gaia parallax error will be still small enough (50% - 100%) to obtain useful distance estimations, allowing for the first time to directly study the 3D distribution of these objects.

5 Conclusions

The precise knowledge of distances is an essential clue to the calibration of the luminosities of stellar candles used to estimate the distances in the Universe, very far beyond the Local Group of galaxies. Hipparcos was a major step forward and the next, spectacular, step will be Gaia, with orders of magnitude improvement in the number of observed targets (from 118 000 for Hipparcos to 1 billion for Gaia) and in the accuracy (from 1 mas for Hipparcos to 10 μ as for Gaia), as well as its full coverage of the HR diagram and its direct reaching of the

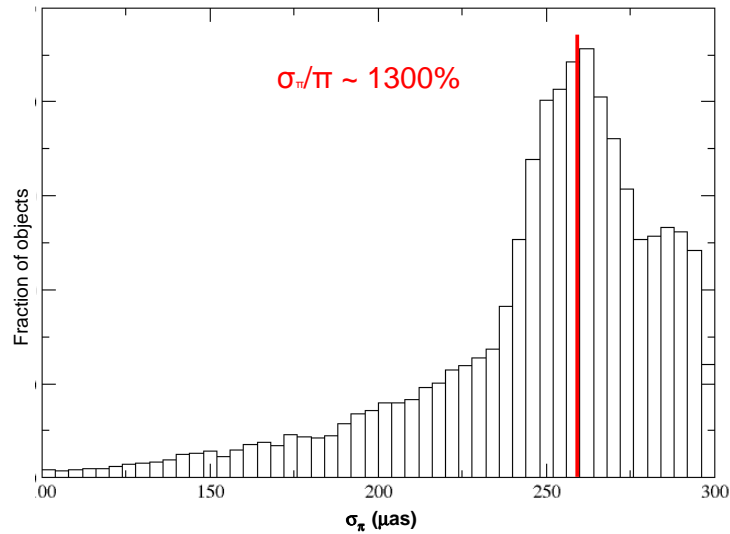


Fig. 4. Distribution of the errors in parallax for the simulated LMC objects. Notice that the maximum is at a relative error of 1300%, but that there is a significant tail of objects reaching low relative errors.

Large and Small Magellanic Clouds.

Finally, the other – also essential – characteristic of Gaia is its capability to obtain photometric and spectroscopic observations quasi-simultaneously with astrometric data. This is a key possibility for a complete study of stellar candles, especially because of the importance of metallicity effects on their luminosity, and holds the promise for a significant advance in the determination of luminosity calibrations and, with them, the distance scale of the universe.

This work was supported by the MICINN (Spanish Ministry of Science and Innovation) - FEDER through grant AYA2009-14648-C02-01 and CONSOLIDER CSD2007-00050. The simulations presented in this paper have been done in the supercomputer MareNostrum at Barcelona Supercomputing Center - Centro Nacional de Supercomputación (The Spanish National Supercomputing Center)

References

- Bienaymé, O., Robin, A. C., & Crézé, M. 1987, *A&A*, 180, 94
 Drimmel, R., Cabrera-Lavers, A., & Lopez-Corredoira, M. 2003, *A&A*, 409, 205
 Gómez, A. E., Grenier, S., Udry, S., et al. 1997, in *ESA Special Publication*, Vol. 402, *ESA Special Publication*, 621–624
 Haywood, M., Robin, A. C., & Creze, M. 1997a, *A&A*, 320, 428
 Haywood, M., Robin, A. C., & Creze, M. 1997b, *A&A*, 320, 440
 Perryman, M. A. C., de Boer, K. S., Gilmore, G., et al. 2001, *A&A*, 369, 339
 Perryman, M. A. C. & ESA, eds. 1997, *ESA Special Publication*, Vol. 1200, *The HIPPARCOS and TYCHO catalogues. Astrometric and photometric star catalogues derived from the ESA HIPPARCOS Space Astrometry Mission*
 Perryman, M. A. C., Lindegren, L., Kovalevsky, J., et al. 1997, *A&A*, 323, L49
 Reid, I. N., Gizis, J. E., & Hawley, S. L. 2002, *AJ*, 124, 2721
 Robin, A., Luri, X., & et al. 2011, submitted to *A&A*
 Robin, A. C., Reylè, C., Derrière, S., & Picaud, S. 2003, *A&A*, 409, 523
 Turon, C. & Perryman, M. A. C. 1999, in *Astronomical Society of the Pacific Conference Series*, Vol. 167, *Harmonizing Cosmic Distance Scales in a Post-HIPPARCOS Era*, ed. D. Egret & A. Heck, 1–12
 van Leeuwen, F. 2007, *A&A*, 474, 653
 van Leeuwen, F. & Fantino, E. 2005, *A&A*, 439, 791

STELLAR CENSUS AND EARLY DYNAMICAL EVOLUTION OF OPEN CLUSTERS

E. Moraux¹

Abstract. In this talk, I will present recent results of the mass function (MF) in open clusters down to the substellar and planetary mass domain. Down to 30 Jupiter masses, the IMF seems to be universal while at lower masses the tendency is not so clear.

I will then discuss how the cluster dynamical evolution may affect the shape of the MF, even at young ages, and especially in the low mass domain. This needs to be taken into account if we want to obtain reliable estimate of the IMF and I will discuss how Gaia and complementary kinematic follow-up will improve the situation.

¹ Institut de Planétologie et d'Astrophysique de Grenoble, France

DANCE: DYNAMICAL ANALYSIS OF NEARBY CLUSTERS

H. Bouy¹ and E. Bertin, E. Moraux, J.C. Cuillandre, J. Bouvier

Abstract. Le projet DANCE (Dynamical Analysis of Nearby ClustErs) a pour objectif de faire une étude systématique de la cinématique et de la dynamique des amas et associations jeunes proches, et de compléter la future mission GAIA dans les régions à forte extinction et jusqu'au domaine des masses planétaires.

En utilisant des images d'archives et des images obtenues plus récemment, nous parvenons à mesurer le mouvement propre de millions de sources sur des régions couvrant plusieurs dizaines et parfois centaines de degrés carrés, avec précision.

¹ CAB - CSIC

EVOLUTION OF OUR GALAXY AND OTHERS WITH THE HIGH-RESOLUTION VERSION OF THE CODE PÉGASE

B. Rocca-Volmerange¹, A. Sourie¹, A. Karampelas², M. Kontizas² and P. Tsalmanza²

Abstract. With the high performances of the Radial Velocity Spectrograph (RVS) on board of the ESA/Gaia mission, Gaia will detect nuclei and the contrasted zones of a large number of galaxies. With the resolution $R \sim 11500$ and the wavelength domain of the RVS (847nm – 874 nm) the main evolutionary parameter is the metallicity traced by the Ca triplet, Fe and Paschen lines. We propose to use the Munari et al., (2005) library with the galaxy evolution code PÉGASE, to constrain the star formation histories and to solve the degeneracy age-metallicity. High-resolution synthetic spectra might be used for educating the Support Vector Machine (SVM) allowing the automatic classification of observed targets.

Keywords: unresolved galaxies, Galaxy, galaxy nuclei, high resolution, metallicity, Calcium triplet

1 Introduction

For several years, an extended library of synthetic spectra of galaxies (Tsalmanza et al., 2009 and references therein) was built for training and testing the classification system (SVM) at the low resolution ($R \sim 200$) of Gaia prisms (BP/RP instruments). The significant fits of this library with the SDSS observations are shown in Fig. 1 for a series of classical types (elliptical, spiral, irregular) and Quenched Star-Forming Galaxies. The evolution code PÉGASE used for this library, in its available version PÉGASE.2 (www.iap.fr/pegase, Fioc & Rocca-Volmerange 1997), is based on the spectral stellar library BaSeL 2.2 suitable for the low resolution instruments of Gaia.

Then a first version of the code at high resolution: PÉGASE-HR (Le Borgne et al, 2004) was built with the observational stellar library ELODIE (Prugniel & Soubiran, 2004) including metallicity effect. The spectral resolution is $R = 10000$ and the optical range $\lambda = 400\text{--}680$ nm. The ELODIE library takes advantage of a fairly complete coverage of the Hertzsprung-Russell (HR) diagram on the range $[\text{Fe}/\text{H}] = -2$ to $+0.4$. PÉGASE-HR is a tool for exploring signatures of metallicity, age, and kinematics. Unhappily it does not cover the wavelength range of the RVS/Gaia.

We intend to improve the resolution of the synthetic library of galaxies computed with the code PÉGASE, on the wavelength domain of the RVS to interpret observations and to test the coherency at low and high resolutions.

2 The high resolution stellar library

The high resolution stellar library (Munari et al, 2005) is based on Kurucz's codes, extended on the wavelength range from 2500–10500 Å at the resolution of 1 Å/pix. The global library maps the whole HR diagram, but is limited to stars with $T_{eff} > 3500\text{K}$. We extract a selection of parameters (T_{eff} , gravity, $[\text{M}/\text{H}]$ and others). The entire library of synthetic spectra is accessible via the web, gently complemented for a given α/Fe range by R. Sordo and A. Vallenari (private communication). The contribution of cold stars to this library is in development.

¹ Institut d'Astrophysique de Paris, 98bis Bld Arago, 75014 Paris, France

² University of Athens, Greece

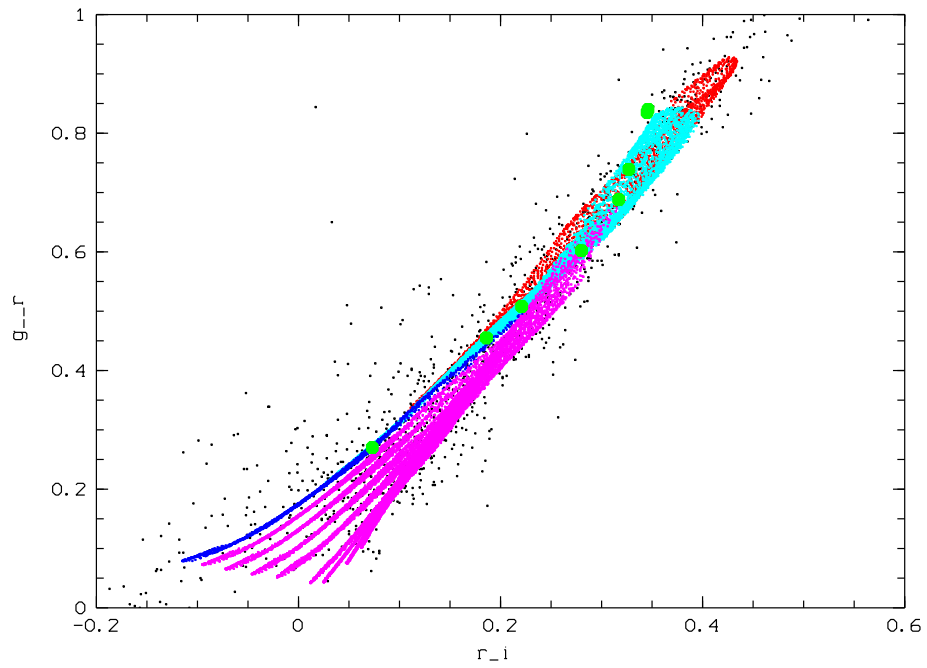


Fig. 1. The synthetic library of galaxies by types for Gaia compared to observations of the SDSS $g-r/r-i$ diagram.

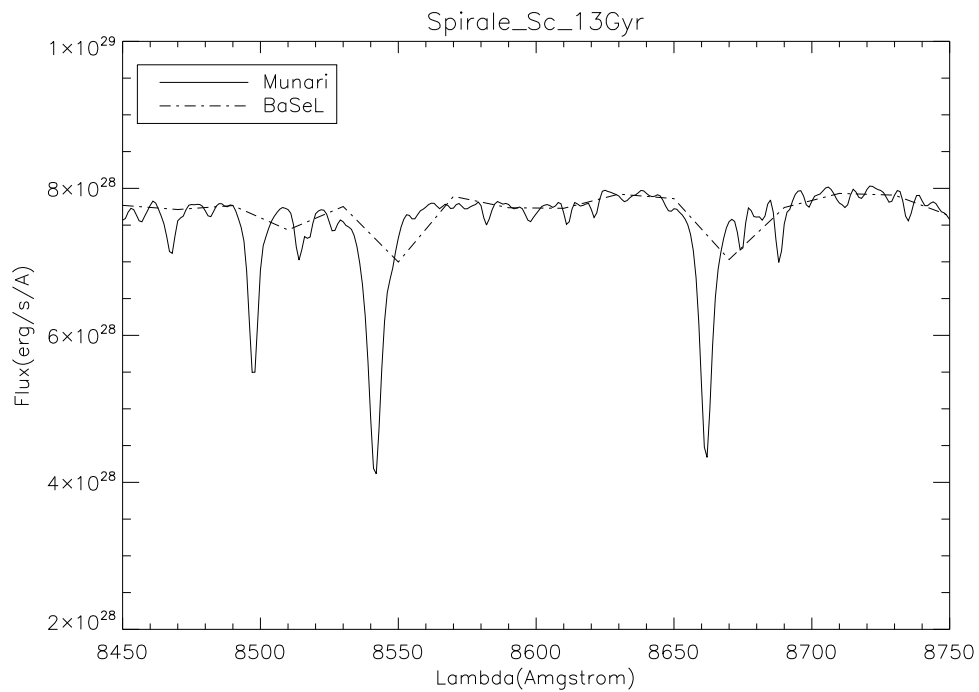


Fig. 2. Sc spiral SEDs at 13 Ga predicted by the code PÉGASE at low and high resolution through the RVS window.

3 Present status of the code PÉGASE-HR2

The new version of PEGASE-HR2, based on the theoretical library described in the previous section computes high-resolution single stellar populations (SSPs) from 10^7 to 2.10^{10} a. Evolution scenarios of galaxies are computed by a combination of SSPs giving predictions of Spectral Energy Distributions (SEDs) by types at all ages. The wavelength domain covers the RVS domain, allowing to follow the evolution of the Calcium triplet, Fe and Paschen H lines. The star formation laws are those adopted for the Gaia synthetic library at low resolution (Tsalmantza et al, 2009). They are fitting at best SEDs of the $z=0$ templates by galaxy types.

After checking the coherency of flux calibration between the code PÉGASE and the library by Munari et al, (2005), we compute SEDs for various galaxy types.

Fig. 2 compares the two SEDs at low and high resolutions for a typical spiral Sc galaxy of 13 Ga old. The lack of cold stars is hard to evaluate but its effect on the equivalent widths of absorption lines will be improved in the near future by a complement of cold star spectra. Predictions are extended to evolved populations from globular clusters, starbursts, spirals Sd to Sa and elliptical galaxies.

References

- Fioc, M., Rocca-Volmerange, B. 1997, A&A, 326, 950
Le Borgne, D., Rocca-Volmerange, B., Prugniel, P., Lançon, A., Fioc, M., Soubiran, C., 2004, A&A, 425, 881
Munari, U., Sordo, R., Castelli, F., Zwitter, T., 2005, A&A, 442, 1127
Prugniel, Ph., Soubiran, C., 2004, arXiv:astro-ph/0409214
Tsalmantza, P., Kontizas, M., Rocca-Volmerange, B., Bailer-Jones, C.A.L., et al., 2009, A&A, 504, 1071

A.S. GAIA: 2007-2011 AND PERSPECTIVES

C. Turon¹, F. Arenou¹ and M. Haywood¹

Abstract. The Action Spécifique Gaia (A.S. Gaia) has been created mid-2007 by the French National Institute for the Sciences of the Universe (INSU) with the aim of coordinating the French activities related to Gaia, the next ESA cornerstone mission, planned for launch by mid-2013. Various actions have been conducted in order to support 1) studies and ground-based observations mandatory for the calibration of Gaia instruments and for Gaia data analysis and 2) preparatory modelling and observations in view of enhancing the scientific return expected from Gaia data. Perspectives for the coming years are presented.

Keywords: Space observatory, Astrometry, Surveys, Galaxy: structure and evolution, Stars: fundamental parameters, ISM: 3-D structure, Minor planets and asteroids: orbits and fundamental parameters.

1 Introduction

Based on the experience gained with Hipparcos, the first space astrometry mission, launched by ESA in 1989 (Perryman et al. 1997), Gaia, the next ESA cornerstone mission, due for launch in 2013, continues the pioneering tradition of Europe space astrometry (Perryman et al. 2001). However, Gaia will surpass its predecessor by several orders of magnitude in terms of accuracy, limiting magnitude and volume of data. While Hipparcos had a predefined observing program, Gaia will systematically survey the sky, observing all objects brighter than magnitude 20, providing an unbiased view of the sky within a well-defined limit in flux. This combination of a complete census capability with an extreme astrometric accuracy and the simultaneous astrophysical characterisation of the observed objects by multi-epoch spectrophotometric and radial-velocity measurements makes Gaia a unique observatory with a very wide range of science goals. Detailed overviews of these science expectations and of the various questions raised by the huge mass of data expected from Gaia are available, among other references, in the proceedings of the Conference *Gaia at the Frontiers of Astrometry* (Turon et al. 2011).

Gaia is raising two types of challenge: the data processing (devoting one second per star would mean 30 years of data processing ...) and the data scientific exploitation: one billion objects will be repeatedly observed (about 74 observations per objects over the mission duration) with the astrometric, spectrophotometric and spectroscopic instruments on-board Gaia, with an extreme astrometric accuracy and an unprecedented homogeneity. While ESA is funding the satellite in its entirety - including the payload and operations - data reduction is mainly in charge of Member States, as is, of course, the data scientific exploitation. Since 2006, the Gaia Data Processing and Analysis Consortium (DPAC) has been appointed by ESA to process the raw data that will arrive from the Gaia satellite. It is a consortium of over 400 scientists all over Europe, chaired by François Mignard (Observatoire de la Côte d'Azur) and France is its first contributor with about 25 % of the members and manpower. In parallel, in many countries, national structures have been created to coordinate the national activities related to Gaia and prepare their respective astronomical communities for the exploitation of this unique and huge set of data. In France, the Action Spécifique Gaia (A.S. Gaia) has been created mid-2007 by the CNRS National Institute for the Sciences of the Universe (INSU). Also a European network, GREAT= Gaia Research for European Training, is being supported by ESF over the period 2010-2015.

The role of A.S. Gaia is multiple: to prepare the French astronomers, in strong co-operation with European and worldwide colleagues, to best exploit Gaia scientific data in their various domains of application (information about Gaia performance, support to related theory and modelling, support to complementary ground-based observations, including the design of new instrumentations); to support initiatives of dedicated workshops and international meetings; to support ground-based observations required by the Gaia data analysis and not otherwise funded; to represent the French Gaia community towards our National funding authorities and contribute to their roadmaps.

¹ GEPI, Observatoire de Paris, CNRS, Université Paris Diderot ; 5 Place Jules Janssen, 92190 Meudon, France

2 Meetings and workshops

2.1 Plenary meetings

After a kick-off meeting in December 2007, the annual meetings of SF2A are the occasion either of plenary meetings of A.S. Gaia or of common workshops with other *Programmes Nationaux* and other European professional astronomical societies: A.S. Gaia and complementarity with optical surveys (2008); A.S. Gaia and complementarity with asteroseismology (2009); Common workshops 1) *Stellar populations and modelling of the Galaxy: now and after Gaia and complementary ground-based observations*, A.S. Gaia - PNCG, 2) *Resolved Stellar Populations*, SF2A - Società Astronomica Italiana - PNCG - PNPS - A.S. Gaia (2010); Common workshop *Stellar and Interstellar physics for the modelling of the Galaxy and its components*, A.S. Gaia - SF2A - Sociedad Española de Astronomía - PNPS - PNCG - PCMI * (2011). In addition, SF2A plenary meetings have been the occasion to present various domains of application of Gaia: *The Solar System seen by Gaia: new perspectives for asteroid science* by P. Tanga (2008), *Applications de Gaia à la métrologie, la relativité et la physique fondamentale* by F. Mignard (2009), *Gaia : promises and expectations in the field of galactic astronomy* by M. Haywood (2010), and *Stellar physics with Gaia* by B. Plez (2011).

2.2 Topical workshops

Many topical workshops have been organised with the support of A.S. Gaia, in the various fields of application of Gaia data, with the aim of presenting the performance of Gaia astrometry, photometry and spectroscopy. The goals are to make the community well aware of the enormous potential of the mission and to encourage and coordinate efforts in modelling and ground-based observations, including the design of new instruments (for example wide-field multiplex spectrographs) and the establishment of networks of Observatories (e.g. for tracking solar system objects, particularly near-Earth objects), in view of a fruitful scientific exploitation of Gaia data. Information on these workshops, their program and the presentations are available from the A.S. Gaia website (<http://wwwhip.obspm.fr/AS/>).

- 2008: *Reference systems and QSOs*, Bordeaux Observatory, P. Charlot & G. Bourda, 24/10/2008. *Earth-based support to Gaia Solar System science*, Beaulieu sur Mer, P. Tanga & W. Thuillot, 27-28/10/2008.
- 2009: *Multiplex spectroscopy in complement to Gaia*, Nice Observatory, A. Recio-Blanco & V. Hill, 19-20/02/2009. *The Milky Way*, Besançon Observatory, A. Robin, C. Reylé & M. Shulteis, 5-6/11/2009.
- 2010: *Extragalactic Science with Gaia*, Institut d'Astrophysique de Paris, E. Slezak & J. Souchay, 14-16/06/2010. *Milieu Interstellaire*, Paris Observatory, R. Lallement & D. Marshall, 25-26/11/2010. *Gaia Follow-Up Network for the Solar System Objects*, Paris Observatory, W. Thuillot, P. Tanga & D. Hestroffer, 29/11- 01/12/2010 (proceedings: Tanga & Thuillot 2011).
- 2011: *Alertes Gaia*, Institut d'Astrophysique de Paris, M. Dennefeld, 27/05/2011. *Orbiting couples: 'Pas de deux' in the Solar System and the Milky Way*, Paris Observatory, F. Arenou & D. Hestroffer, 10-12/10/2011. *Relevés spectroscopiques en accompagnement à Gaia*, Paris Observatory, P. Bonifacio & C. Babusiaux, 17-18/11/2011.

Beside these workshops and plenary meetings, A.S. Gaia provides some support to a few international conferences organised by French colleagues in France or elsewhere in Europe.

3 Support to ground-based observations

Two categories of ground-based observations, or projects for new instrumentations, are being supported by A.S. Gaia: observations necessary for the data analysis to ensure the precision and accuracy of the future Gaia data (in the context of DPAC) and observations expected to complement Gaia data, with the aim of enhancing the scientific return.

*PNCG = Programme National Cosmologie et Galaxies, PNPS = Programme National de Physique Stellaire, PCMI = Programme National de Physique et Chimie du Milieu Interstellaire

3.1 Ground-based observations in support to Gaia data analysis

A.S. Gaia is supporting two types of ground-based observations in this category: observations for the calibration of the RVS, the Radial Velocity Spectrometer aboard Gaia, and astrometric observations:

- There is no calibration source on board the RVS and the zero-point of radial velocities has to be defined using reference stars and asteroids. The radial velocity stability of these objects must be assured to within 300 m s^{-1} until the end of the mission. 1420 candidate stars were selected and observed in both hemispheres (Crifo et al. 2010). The Northern part (with the Sophie spectrograph at Observatoire de Haute Provence (OHP) and Narval at Observatoire du Pic du Midi) is supported by PNPS and PNCG. The Southern part (with Coralie on the Swiss telescope at La Silla) is supported by A.S. Gaia.
- Astrometric observations of WMAP are performed as a test of the possibility to obtain the position of Gaia on its orbit (also at L2 and with a very similar expected magnitude) with an uncertainty of 150 m in position and 2.5 mm/s in velocity (Taris et al. 2008). Observations of QSOs and compact extragalactic objects are made to enlarge the catalogue of radio sources to be used for aligning the International Celestial Reference System (ICRF) to the Gaia reference system: search for new suitable sources observed in VLBI and observations in the optical wavelengths to detect any variability (Charlot 2011). A.S. Gaia is supporting the observations made in OHP for these two programmes.

3.2 Ground-based observations in support to the preparation of Gaia data scientific exploitation

Most activity in this area is concentrated in two domains: high resolution spectroscopy for galactic archeology (support to observations with existing spectrographs and to the design of new multiplex wide-field spectroscopic instruments), and observations of minor bodies in the Solar System.

- *Galactic archeology.* With its unprecedented astrometric, photometric and spectroscopic survey of all stellar populations, Gaia will revolutionise our knowledge of Galactic and stellar evolution. However, *only* medium resolution spectroscopy ($R = 11\,500$) will be available from the RVS (Radial Velocity Spectrometer) on-board Gaia, and *only* for the brightest 10 million stars, leading to a huge but incomplete knowledge of the abundances and stellar atmospheric parameters. It has long been emphasised that high-resolution spectroscopy would be an essential complement to Gaia data and that Europe should consider the importance of large programmes of ground-based observations using existing instruments, and of designing wide angle high multiplex spectrograph(s) to be mounted on a dedicated ground-based telescope (de Zeeuw & Molster 2007; Turon et al. 2008). This resulted in the setting up of a Working Group on Galactic archeology within the GREAT ESF network, in the proposal of a Gaia-ESO public spectroscopic survey (accepted by ESO in June 2011), and in various projects for new dedicated instrumentations. A.S. Gaia is supporting the participation and contributions of French astronomers to all these actions.
- Observations of minor bodies in the Solar System. Gaia will detect and provide very precise astrometric and photometric measurements for a large number of asteroids. However, a ground-based follow-up is essential to confirm the new detections, to improve the determination of the orbits and to obtain a maximum of information about the physics of the objects observed by Gaia. A Gaia Follow Up Network of Solar System Objects (Gaia-FUN-SSO) is being established, involving observatories of very many countries around the globe (Tanga & Thuillot 2011). In this context, various astrometric, photometric, or spectroscopic observations are considered. This action is accompanied by a theoretical and modelling effort to interpret the results in term of Solar System formation and evolution.

4 Support to modelling and theoretical activities

As for ground-based observations, modelling activities are of two kinds: necessary for data analysis, in the context of DPAC, and in preparation for the exploitation of Gaia data.

4.1 Modelling and theoretical activities in support to Gaia data analysis

Gaia will observe all objects down to magnitude $V = 20$, i.e. a wide variety of stars, solar system bodies, and compact extragalactic objects. To be able to identify, classify and characterise them, it is essential to have a reliable modelling of how these objects will be seen through the Gaia optical system. With one billion objects,

all types of objects, even the rarest, will be observed in large quantity and classification algorithms should be extremely efficient and tested in advance for all possible cases. Many actions in this direction have already been supported by A.S. Gaia during the past four years and these efforts will continue in the coming years.

Among them: modelling of massive atmospheres of hot stars with emission lines with test and improvement of classification algorithms; simulation of globular clusters and multiple star systems and observability with Gaia; estimation of the performance of the RVS for the chemical analysis of giant stars (test on ground-based data); modelling of double stars and estimation of the uncertainties on the astrometric parameters; simulation of the detection and observation of binary asteroids; simulation of the observation of extended objects; development of a library of synthetic spectra of galaxies for the automatic classification of galaxies unresolved by Gaia; simulation and analysis of a catalogue of quasars and AGN for the definition of the Gaia reference system.

4.2 *Modelling and theoretical activities in support to the preparation of Gaia data scientific exploitation*

As already emphasised above, Gaia will observe in a systematic way all objects down to magnitude $V = 20$, thus achieving a complete census of stars in a large part of the Galaxy and of their stellar or planetary companions in the solar neighbourhood. It will provide an unbiased sampling of all stellar populations of the Galaxy, and of the brightest stars in galaxies of the Local Group. Optimum use of this mass of data requires new methods and models and A.S. Gaia has regularly allocated a high priority to such requests. This is also an effort that should be continued in order to obtain a scientific return at the level of the major investment made by France in Gaia preparations.

A list of the various studies supported within this framework is given here: kinematics and modelling of the Galactic bulge; kinematics and structure of the Galactic disk; 3D NETL modelling of stellar chromospheres in order to improve the determination of atmospheric parameters and abundances; calculation of collision rates for the NLTE modelling of stellar atmospheres; modelling of the observation of metal-poor giant stars and test with ground-based measurements; development of criteria for the taxonomic classification and the determination of the absolute magnitude and spectral characteristics of asteroids; modelling of the shape of asteroids from observations of stellar occultations by asteroids; prediction of close encounters of asteroids and determination of their masses; thermophysical modelling of asteroids; observability of comets with Gaia and modelling of the effect of non-gravitational forces on their orbits; preparation of the alignment of ICRF with the Gaia reference system; tests of relativity using Hipparcos, radar and Gaia data.

5 Perspectives

Since 2007, A.S. Gaia has played a strong role in the coordination of actions related to Gaia in France. During that period, the scientific and observational context has changed, with the increasing importance of systematic sky surveys (in photometry up to now) to detect and map halo streams, and of detailed spectroscopic analysis to better understand the evolution of all Galactic stellar populations. Also, the European astronomical community got organised to prepare for the scientific exploitation of Gaia data. The period 2011-2015 will cover the final preparations for the processing of Gaia data, hopefully the launch of the satellite, and the preparation for the first tests on real data. In addition to an increased support to programmes in preparation to Gaia data scientific exploitation, support to actions related to the preparation of the publication of the catalogue will become essential.

References

- Charlot, P. 2011, EAS Publications Series, Volume 45, 345
 Crifo, F., Jasniewicz, G., Soubiran, C. et al. 2010, A&A, 524, A10
 de Zeeuw, P.T. & Molster, F.J. (eds) 2007, Astronet Science Vision for European Astronomy
 Perryman, M.A.C., Lindgren, L. Kovalevsky, J. et al. 1997, A&A, 323, L49
 Perryman, M.A.C., de Boer, K. S., Gilmore, G. et al. 2001, A&A, 369, 339
 Tanga, P. & Thuillot, W. (eds) 2011, Gaia Follow-up Network for the Solar System Objects
 Taris, F. et al. 2008, Proceedings of the Annual meeting of SF2A, C. Charbonnel, F. Combes and R. Samadi (eds), p. 39
 Turon, C., Meynadier, F. & Arenou, F. (Eds) 2011, ELSA Conference 2010: Gaia at the Frontiers of Astrometry, EAS Pub. Series, Vol. 45
 Turon, C., Primas, F., Binney, J. et al. 2008, ESA-ESO WG report No.4, Galactic Populations, Chemistry and Dynamics

DETERMINATION OF STELLAR PARAMETERS AND THEIR UNCERTAINTIES

C. Allende Prieto¹

Abstract. A number of ongoing and planned large surveys of Milky Way stars require efficient algorithms to derive stellar parameters from photometry, spectra, astrometry, or a combination. This talk will give an overview of the strategies in use or under consideration, and the possible pitfalls for their successful application.

¹ Instituto de Astrofísica de Canarias, Spain

PERSPECTIVE IN DETAILED ELEMENT ABUNDANCE DETERMINATION

E. Caffau¹

Abstract. Observed spectra of stars betray the presence of elements in stellar atmospheres by the presence of absorption/emission lines. To quantify the amount of a certain element in a particular stellar atmosphere, knowledge of atomic/molecular data and a physical model of the photosphere are necessary. Depending on the quality of the spectra the requested precision in the knowledge changes. In the analysis of low resolution, low signal-to-noise spectra, traditional 1D-LTE analysis is sufficient for most purposes. There are some particular situations in which we think that the use of 3D models is to be preferred over the use of traditional 1D model atmospheres. To make few examples I worked on 1. The abundance investigation of the solar photosphere. 2. The ${}^6\text{Li}/{}^7\text{Li}$ isotopic ratio. 3. Detailed abundances in metal-poor stars. Also deviations from local thermal equilibrium in high quality spectra sometimes cannot be neglected. I will consider the analysis of low resolution and high resolution spectra, according my experience.

¹ ZAH - Landessternwarte Heidelberg

BUILDING PART OF THE GALACTIC HALO FROM GLOBULAR CLUSTERS

T. Decressin, C. Charbonnel, G. Meynet¹ and H. Baumgardt, P. Kroupa²

Abstract. Globular clusters are known to harbor several populations of stars which differ from their chemical composition. A first generation of stars shows similar chemical pattern than halo field stars. Besides stars of second generation display strong variations in light elements (C to Al) while they have similar abundances in heavy elements than first generation stars. This chemical pattern can be explain by a pollution of the intercluster medium by massive stars of first generation during the birth of the proto-globular cluster. One important feature of globular clusters observed today is that 50 to 80% of the low mass stars still evolving in the cluster are second generation stars whereas, with a standard IMF, these stars should be at most 10% of the cluster stars. This strong discrepancy can be solved if the proto-globular clusters were more massive (up to a factor 20-30) and mass-segregated during their formation. In this case a strong loss of first generation stars occupying the outer part of the cluster is possible through the dynamical history of the cluster. Those escaping stars now populate the halo of the Galaxy.

¹ Geneva Observatory, Switzerland

² Argelander Institute for Astronomy, Bonn, Germany

THE DEPENDENCE OF THE GALACTIC STAR FORMATION LAWS ON METALLICITY

S. Dib¹, L. Piau², S. Mohanty¹ and J. Braine³

Abstract. We describe results from semi-analytical modelling of star formation in protocluster clumps of different metallicities. In this model, gravitationally bound cores form uniformly in the clump following a prescribed core formation efficiency per unit time. After a contraction timescale which is equal to a few times their free-fall times, the cores collapse into stars and populate the IMF. Feedback from the newly formed OB stars is taken into account in the form of stellar winds. When the ratio of the effective energy of the winds to the gravitational energy of the system reaches unity, gas is removed from the clump and core and star formation are quenched. The power of the radiation driven winds has a strong dependence on metallicity and it increases with increasing metallicity. Thus, winds from stars in the high metallicity models lead to a rapid evacuation of the gas from the protocluster clump and to a reduced star formation efficiency, as compared to their low metallicity counterparts. We derive the metallicity dependent star formation efficiency per unit time in this model as a function of the gas surface density Σ_g . This is combined with the molecular gas fraction in order to derive the dependence of the surface density of star formation Σ_{SFR} on Σ_g . This feedback regulated model of star formation reproduces very well the observed star formation laws in galaxies extending from low gas surface densities up to the starburst regime. Furthermore, the results show a dependence of Σ_{SFR} on metallicity over the entire range of gas surface densities, and can also explain part of the scatter in the observations.

Keywords: Stars: massive, winds; ISM: clouds, galaxies: star formation: star clusters

1 Introduction

Over the last two decades, the dependence of the star formation rate surface density (Σ_{SFR}) on the gas surface density (Σ_g) and eventually on other physical quantities has been extensively investigated both observationally (e.g., Kennicutt 1998; Wong & Blitz 2002; Boissier et al. 2003; Bigiel et al. 2008; Blanc et al. 2009; Onodera et al. 2010; Tabatabaei & Berkhuijsen 2010; Heiner et al. 2010; Schrubba et al. 2011; Bolatto et al. 2011) as well as theoretically and numerically (e.g., Tutukov 2006; Krumholz & Thompson 2007; Fuchs et al. 2009; Silk & Norman 2009; Krumholz et al. 2009a; Papadopoulos & Pelupessy 2010; Gnedin & Kravtsov 2011; Narayanan et al. 2011; Feldmann et al. 2011; Vollmer & Leroy 2011; Braun & Schmidt 2011; Monaco et al. 2011; Kim et al. 2011; Dib 2011a,b). Determining the rate of star formation in a given tracer of the gas surface density requires quantifying the fraction of that tracer as a function of the global gas surface density and a description of the efficiency at which the star forming gas is converted into stars per unit time. The relationship between Σ_{SFR} and the surface density of the molecular hydrogen gas Σ_{H_2} is given by:

$$\Sigma_{SFR} = \Sigma_g f_{H_2} \frac{SFE_\tau}{\tau}, \quad (1.1)$$

where $f_{H_2} = \Sigma_{H_2}/\Sigma_g$ is the molecular hydrogen mass fraction, SFE_τ is the star formation efficiency over the timescale τ . Krumholz & McKee (2005) proposed a theory in which supersonic turbulence is the dominant agent that regulates star formation in giant molecular clouds (GMCs). They derived a core formation efficiency per unit free-fall time, CFE_{ff} , which is given by $CFE_{ff} =$

¹ Astrophysics Group, Blackett Laboratory, Imperial College London, London SW7 2AZ; s.dib@imperial.ac.uk

² LATMOS, 11 Boulevard d'Alembert, 78280 Guyancourt, France

³ Laboratoire d'Astrophysique de Bordeaux, Université de Bordeaux, OASU CNRS/INSU, 33271 Floirac, France

$0.15\alpha_{vir}^{-0.68}\mathcal{M}^{-0.32}$, where α_{vir} and \mathcal{M} are the virial parameter and the *rms* sonic Mach number of the GMC, respectively*. By assuming that only a fraction of the mass of the cores ends up in the stars, this CFE_{ff} can be converted into a star formation efficiency $SFE_{ff} = \eta \times CFE_{ff}$ ($\eta \leq 1$). An alternative theory has been recently proposed by Dib et al. (2011) and Dib (2011a,b) in which the star formation rate in protocluster clumps is primarily regulated by feedback from massive stars and in particular through energy injection in the clumps by stellar winds. In the following sections, we briefly describe the main constituents of this model.

2 Feedback regulated star formation

The model follows the formation of dense gravitationally bound cores in a protocluster clump. Cores form in the clump with a given core formation efficiency per unit time and follow a local mass distribution that is the result of the gravo-turbulent fragmentation of the clump. In their series of models, Dib et al. (2011) varied the core formation efficiency per unit free-fall time (CFE_{ff}) between 0.1 and 0.3. This is consistent with the range of CFE_{ff} measured in numerical simulations which describe the gravo-turbulent fragmentation of magnetised, turbulent, and self-gravitating molecular clouds (e.g., Dib et al. 2008; Dib et al. 2010a). The gravitationally bound cores that are generated at every epoch have a mass distribution that is given by the gravo-turbulent fragmentation model of Padoan & Nordlund (2002). In this work, we leave out, for simplicity, the role played by gas accretion and coalescence in modifying the mass distribution of the cores. The interested reader is referred to Dib et al. (2007) and Dib et al. (2010b) for such models. Cores contract over a lifetime which is a few times their free-fall time before collapsing to form stars. Feedback from the most massive stars ($M_{\star} \geq 5 M_{\odot}$) is taken into account in the form of stellar winds. The formation of cores in the protocluster clump, and consequently star formation, are terminated whenever the fraction of the wind energy stored into motions that oppose gravity exceeds the gravitational energy of the clump. In order to calculate reliable estimates of the feedback generated by metallicity dependent stellar winds, we proceed in two steps. In the first step, we use a modified version of the stellar evolution code CESAM (see appendix 1 in Piau et al. 2011) to calculate a grid of main sequence stellar models for stars in the mass range [5-80] M_{\odot} (with steps of 5 M_{\odot}) at various metallicities $Z/Z_{\odot} = [1/10, 1/6, 1/3, 1/2, 1, 2]$ ($Z_{\odot} = 0.0138$). The evolution of massive stars is followed using the CESAM code for ~ 1 Myr, on the main sequence. The characteristic stellar properties, which are the effective temperature T_{eff} , the luminosity L_{\star} , and the stellar radius R_{\star} are then used in the stellar atmosphere model of Vink et al. (2001) in order to calculate the stellar mass loss rate \dot{M}_{\star} . Vink et al. (2001) did not derive the values of the terminal velocities of the winds (v_{∞}), therefore, we use instead the derivations of v_{∞} obtained by Leitherer et al. (1992).

The power of the stellar winds is given by $\dot{M}_{\star}v_{\infty}^2$. This quantity is displayed in Fig. 1 for the models with different metallicities. The values of $\dot{M}_{\star}v_{\infty}^2$ are fitted with fourth order polynomials (overplotted to the data) and whose coefficients are provided in Dib et al. (2011). The $\dot{M}_{\star}v_{\infty}^2 - M_{\star}$ relations displayed in Fig. 1 allow for the calculation of the total wind energy deposited by stellar winds. The total energy from the winds is given by:

$$E_{wind} = \int_{t'=0}^{t'=t} \int_{M_{\star}=5 M_{\odot}}^{M_{\star}=120 M_{\odot}} \left(\frac{N(M_{\star})\dot{M}_{\star}(M_{\star})v_{\infty}^2}{2} dM_{\star} \right) dt'. \quad (2.1)$$

We assume that only a fraction of E_{wind} will be transformed into systemic motions that will oppose gravity and participate in the evacuation of the bulk of the gas from the proto-cluster clump. The effective kinetic wind energy is thus given by:

$$E_{k,wind} = \kappa E_{wind}, \quad (2.2)$$

where κ is a quantity ≤ 1 (in this work, we use $\kappa = 0.1$ for all models). $E_{k,wind}$ is compared at every timestep to the absolute value of the gravitational energy, E_{grav} , which is calculated as being:

$$E_{grav} = -\frac{16}{3}\pi^2 G \int_0^{R_c} \rho_c(r)^2 r^4 dr. \quad (2.3)$$

*Padoan & Nordlund (2011) found a different dependence of the SFR on α_{vir} and \mathcal{M} . The results of their numerical simulations suggest that the SFR decreases with increasing α_{vir} but also that it increases with increasing \mathcal{M} .

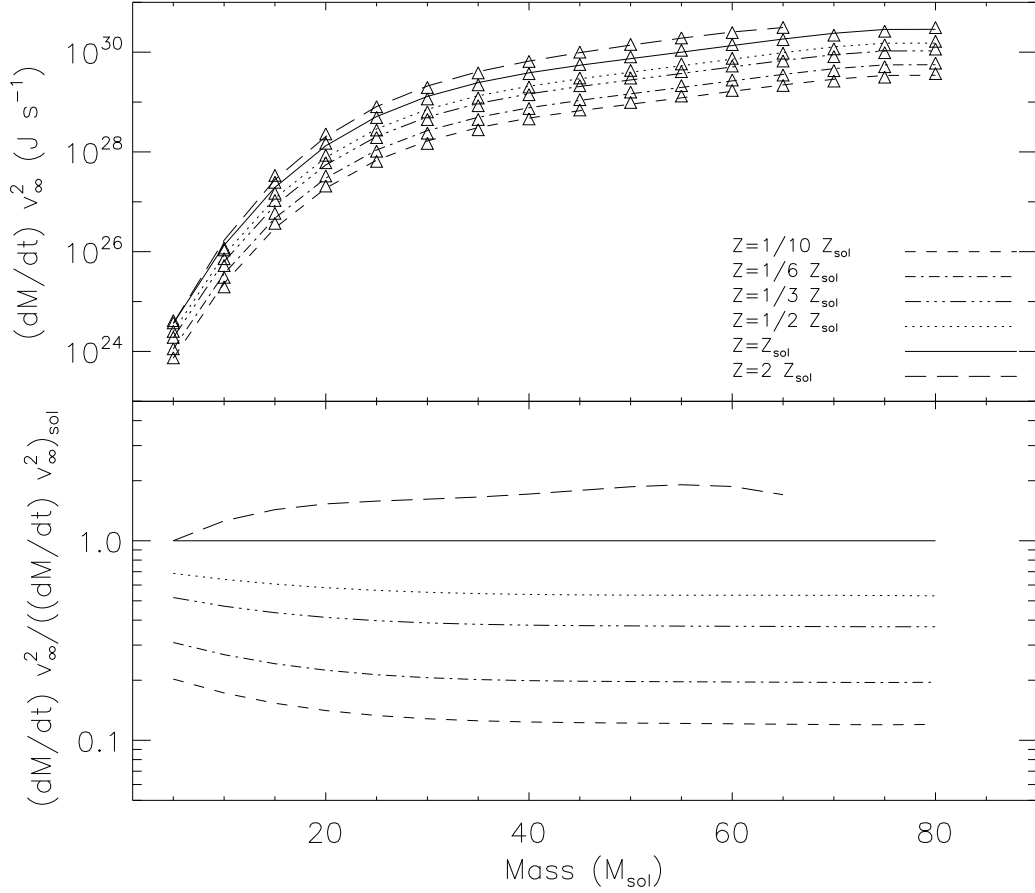


Fig. 1. The power of the stellar winds, or wind luminosities, for stars in the mass range 5–80 M_{\odot} on the main sequence, and for various metallicities. The stellar mass loss rates have been calculated using the stellar characteristics (effective temperature, stellar luminosity and radius) computed using the stellar evolution code CESAM coupled to the stellar atmosphere model of Vink et al. (2001). The values of v_{∞} have been calculated using the derivation by Leitherer et al. (1992). Over-plotted to the data are fourth order polynomials. The parameters of the fit functions can be found in Dib et al. (2011). Adapted from Dib et al. (2011).

Since higher metallicity stellar winds deposit larger amounts of energy in the clump than their lower metallicity counterparts, this leads them to evacuate the gas from the clump on shorter timescales. This in turn quenches the process of core and star formation earlier and sets a smaller final star formation efficiency, SFE_{exp} . Fig. 2 displays the dependence of SFE_{exp} and of the expulsion time, t_{exp} (expressed in units of the free-fall time t_{ff}), as a function of metallicity for clumps of various masses.

3 Metallicity dependent star formation laws

Using the above described model, it is possible to derive the dependence of Σ_{SFR} on Σ_g . The star formation rate surface density in the feedback regulated mode of star formation is given by:

$$\Sigma_{SFR} = \Sigma_g f_{H2} \frac{\langle SFE_{exp} \rangle}{\langle t_{exp} \rangle}, \quad (3.1)$$

where $\langle SFE_{exp} \rangle$ and $\langle t_{exp} \rangle$ are, respectively, the characteristic SFE_{exp} and the epoch at which gas is expelled from the protocluster region for the clump mass distribution associated with a given Σ_g . Writing $\langle t_{exp} \rangle$ in terms of the clump free-fall time $\langle t_{ff} \rangle$, Eq. 3.1 becomes:

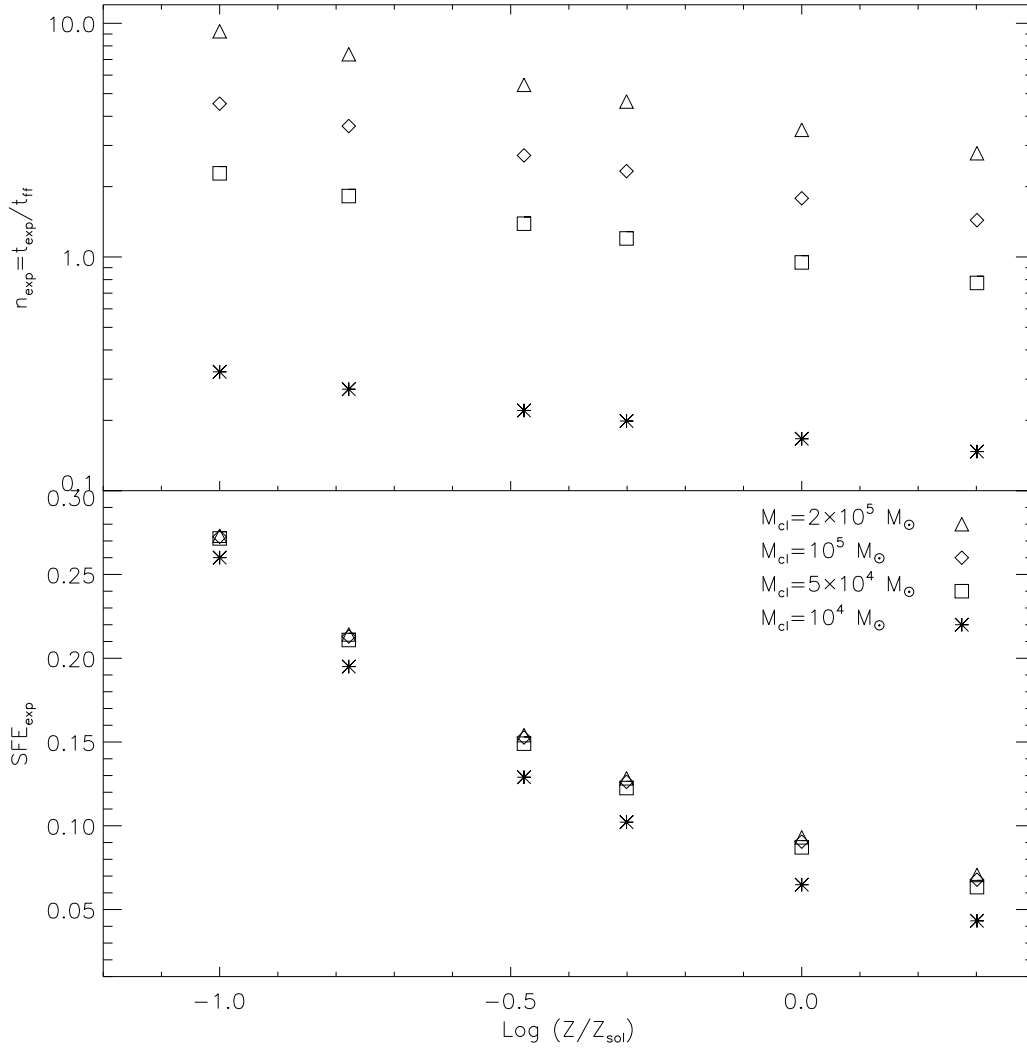


Fig. 2. Dependence of the quantities SFE_{exp} (final star formation efficiency) and $n_{exp} = t_{exp}/t_{ff}$ (ratio of the expulsion time to the free-fall time) for selected values of the protocluster forming clump masses and metallicities. These results are based on the models of Dib et al. (2011).

$$\begin{aligned} \Sigma_{SFR} &= \Sigma_g f_{H_2} \frac{\langle SFE_{exp} \rangle}{\langle n_{exp} \rangle} \frac{1}{\langle t_{ff} \rangle} \\ &= \Sigma_g f_{H_2} \frac{\langle f_{*,ff} \rangle}{\langle t_{ff} \rangle}. \end{aligned} \quad (3.2)$$

where $f_{*,ff}$ is the dimensionless star formation efficiency and which corresponds to the mass fraction of the molecular gas that is converted into stars per free-fall time t_{ff} of the clumps. $\langle f_{*,ff} \rangle$ and $\langle t_{ff} \rangle$ represent characteristic values of $f_{*,ff}$ and t_{ff} for the spectrum of clump masses found in the GMC for a given value of Σ_g . The quantity f_{H_2} is the mass fraction of the total gas that is in molecular form. In this work, we use the functional form of f_{H_2} obtained by Krumholz et al. (2009b) who derived f_{H_2} as a function of the gas surface density and metallicity (see their paper or Dib 2011 for the detailed formula). $\langle t_{ff} \rangle$ can be approximated by the free-fall time of the clump with the characteristic mass $t_{ff}(M_{char}) = 8 \Sigma_{cl}^{-3/4} M_{char,6}^{1/4}$ Myr where $M_{char,6} = M_{char}/10^6 M_{\odot}$. The characteristic mass M_{char} is given by :

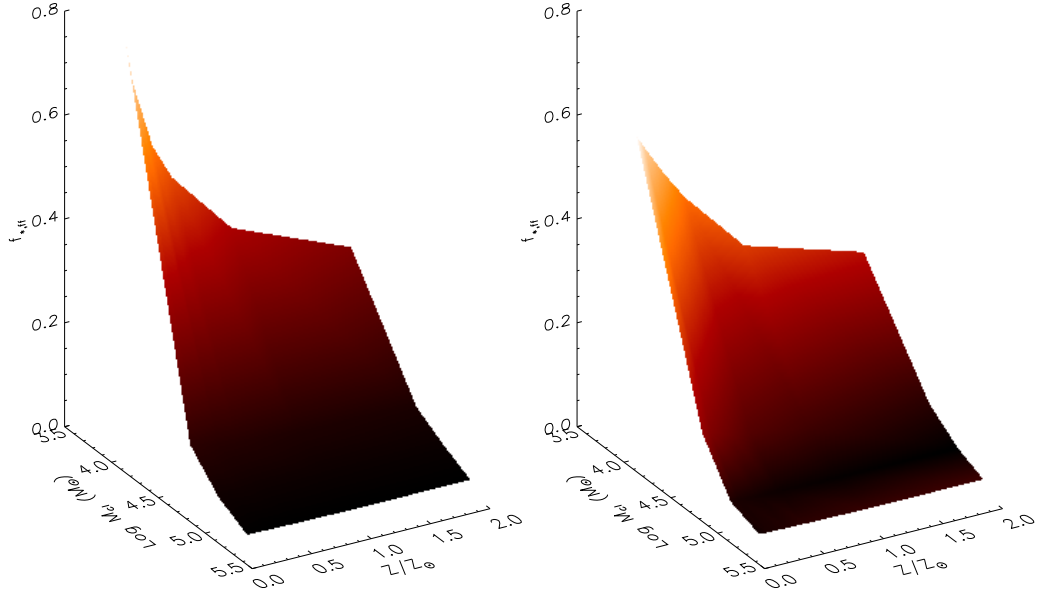


Fig. 3. Star formation efficiency per unit free-fall time in the protocluster clump in the metallicity-dependent feedback model. The star formation efficiencies per free-fell use a core-to-star efficiency conversion factor of 1/3. The left panel displays $f_{*,ff}$ as a function of both M_{cl} and $Z' = Z/Z_{\odot}$ in the original data, while the right panel displays the analytical fit function to this data set given in Eq. 3.5. Adapted from Dib (2011a).

$$M_{char} = \int_{M_{cl,min}}^{\max(M_{cl,max}, M_{GMC})} M_{cl} N(M_{cl}) dM_{cl}, \quad (3.3)$$

where $N(M_{cl})$ is the mass function of protocluster forming clumps which we take to be $N(M_{cl}) = A_{cl} M_{cl}^{-2}$, and A_{cl} is a normalisation coefficient given by $A_{cl} \int_{M_{cl,min}}^{\max(M_{cl,max}, M_{GMC})} N(M_{cl}) dM_{cl} = \epsilon$, where $0 < \epsilon < 1$ is the mass fraction of the GMCs that is in protocluster clumps at any given time. In this work we use $\epsilon = 0.5$. The minimum clump mass $M_{cl,min}$ is taken to be $2.5 \times 10^3 M_{\odot}$ (this guarantees, for final SFEs in the range of 0.05-0.3 a minimum mass for the stellar cluster of $\sim 50 M_{\odot}$) and the maximum clump mass is $10^8 M_{\odot}$. The characteristic GMC mass is determined by the local Jeans mass and is given by:

$$M_{GMC} = 37 \times 10^6 \left(\frac{\Sigma_g}{85 M_{\odot} \text{ pc}^{-2}} \right) M_{\odot}. \quad (3.4)$$

Fig. 4 (top) displays M_{char} as a function of Σ_g . The quantity $f_{*,ff} = SFE_{exp}/n_{exp}$ is displayed in Fig. 3 (left panel) as a function of mass and metallicity ($Z' = Z/Z_{\odot}$). These models use a value of $CFE_{ff} = 0.2$ and standard clump and core parameters (see Dib et al. 2001 and Dib 2011a,b for more detail). A fit to the (M_{cl}, Z') data points with a 2-variables second order polynomial yields the following relation shown in Fig. 3, right panel:

$$\begin{aligned} f_{*,ff}(M_{cl}, Z') = & 11.31 - 4.31 \log(M_{cl}) + 0.41 [\log(M_{cl})]^2 \\ & - 8.28 Z' + 3.20 Z' \log(M_{cl}) - 0.32 Z' [\log(M_{cl})]^2 \\ & + 2.30 Z'^2 - 0.89 Z'^2 \log(M_{cl}) + 0.08 Z'^2 [\log(M_{cl})]^2. \end{aligned} \quad (3.5)$$

Using Eq. 3.5, it is then possible to calculate $\langle f_{*,ff} \rangle$:

$$\langle f_{*,ff} \rangle (Z', \Sigma_g) = \int_{M_{cl,min}}^{\max(M_{cl,max}, M_{GMC})} f_{*,ff}(M_{cl}, Z') N(M_{cl}) dM_{cl}. \quad (3.6)$$

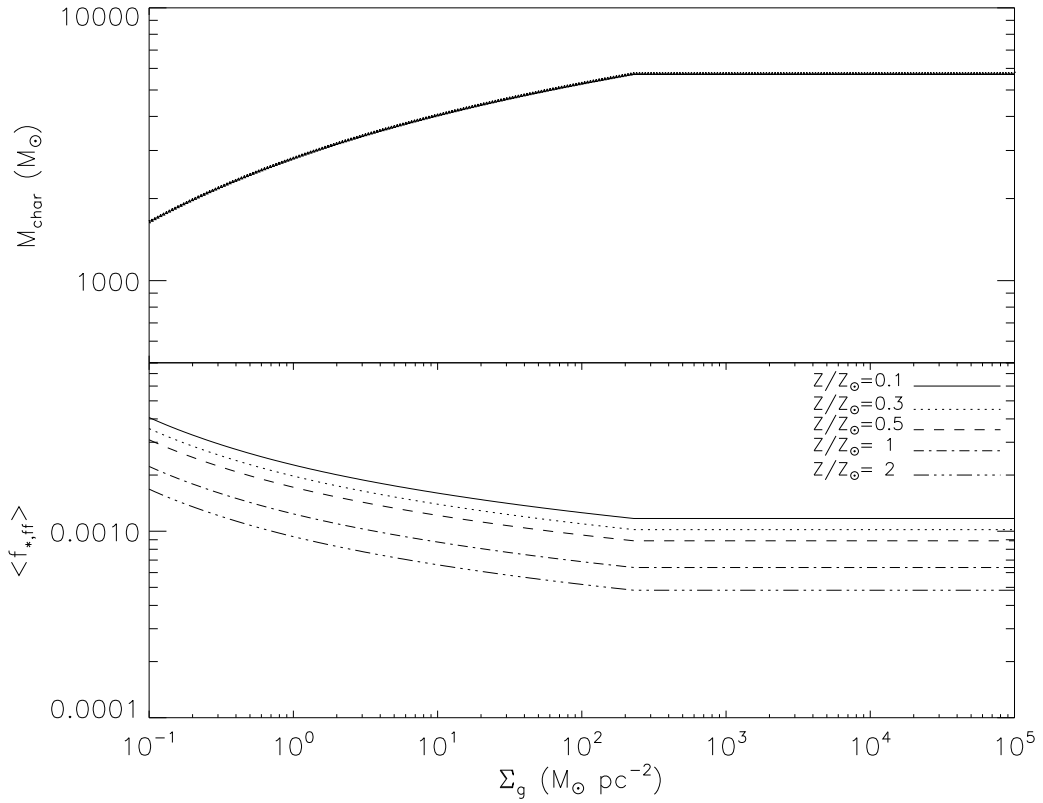


Fig. 4. Characteristic clump mass as a function of the gas surface density (Eq. 3.3, top panel) and the star formation efficiency per unit free-fall time in this feedback regulated model of star formation (lower panel). Adapted from Dib (2011a).

Fig. 4 (bottom) displays $\langle f_{*,ff} \rangle (Z', \Sigma_g)$ for values of Z' in the range $[0.1 - 2]$. We assume that there is a critical value of $\Sigma_g = 85 \text{ M}_\odot \text{ pc}^{-2}$ below which clumps are pressurised by their internal stellar feedback, such that $\Sigma_{cl} = \Sigma_{g,crit}$ where $\Sigma_g < \Sigma_{g,crit}$ and $\Sigma_{cl} = \Sigma_{GMC} = \Sigma_g$ when $\Sigma_g \geq \Sigma_{g,crit}$. With the above elements, the star formation law can be re-written as:

$$\Sigma_{SFR} = \frac{8}{10^6} f_{H_2}(\Sigma_g, c, Z') \Sigma_g \times \left\{ \begin{array}{l} \frac{\langle f_{*,ff} \rangle (Z')}{M_{char,6}^{1/4}} \quad ; \frac{\Sigma_g}{85 \text{ M}_\odot \text{ pc}^{-2}} < 1 \\ \frac{\langle f_{*,ff} \rangle (Z')}{M_{char,6}^{1/4}} \left(\frac{\Sigma_g}{85 \text{ M}_\odot \text{ pc}^{-2}} \right)^{3/4} \quad ; \frac{\Sigma_g}{85 \text{ M}_\odot \text{ pc}^{-2}} \geq 1 \end{array} \right\}, \quad (3.7)$$

where Σ_{SFR} is in $\text{M}_\odot \text{ yr}^{-1} \text{ kpc}^{-2}$, M_{char} is given by Eq. 3.3, and $\langle f_{*,ff} \rangle$ by Eqs. 3.5 and 3.6. Fig. 5 displays the results obtained using Eq. 3.7 for Σ_g values starting from low gas surface densities up to the starburst regime. The results are calculated for the metallicity values of $Z' = [0.1, 0.3, 0.5, 1, 2]$. The results are compared to the sub-kpc data of Bigiel et al. (2008,2010) and to the normal and starburst galaxies results of Kennicutt (1998). The models fits remarkably well the observational results over the entire range of surface densities. Furthermore, the segregation by metallicity extends beyond the low surface density regime up to the starburst regime where a segregation in metallicity of ~ 0.5 dex is observed.

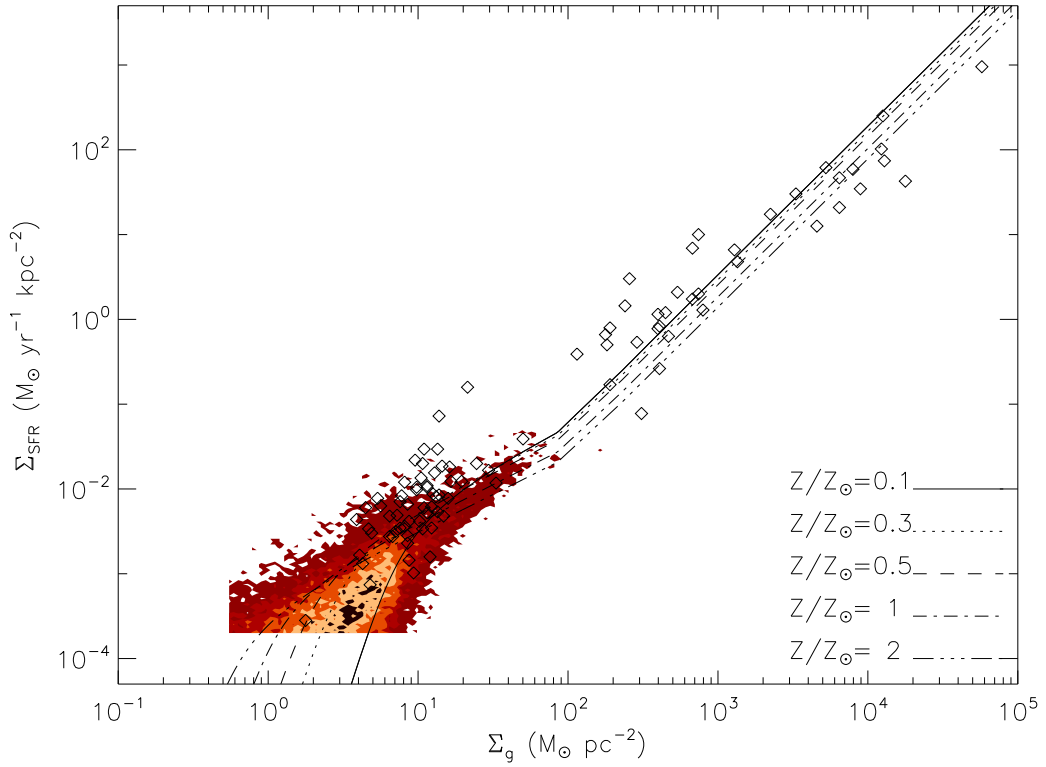


Fig. 5. Star formation laws in the feedback-regulated star formation model. Overplotted to the models are the normal and starburst galaxies data of Kennicutt (1998) and the combined sub-kpc data (4478 subregions) for 11 nearby galaxies from Bigiel et al. (2008,2010). The Bigiel et al. data is shown in the form of a 2D histogram with the colour coding corresponding, from the lighter to the darker colours to the 1,5,10,20, and 30 contour levels. The displayed theoretical models cover the metallicity range $Z' = Z/Z_{\odot} = [0.1, 2]$.

4 Conclusions

We have presented a model for star formation in protocluster clumps of different metallicities. The model describes the co-evolution of the dense core mass function and of the IMF in the clumps. Cores form uniformly over time in the clumps following a prescribed core formation efficiency per unit time. Cores contract over timescales which are a few times their free fall time before they collapse to form stars. Feedback from the newly formed OB stars ($> 5 M_{\odot}$) is taken into account and when the ratio of the cumulated effective kinetic energy of the winds to the gravitational energy of the system (left over gas+stars) reaches unity, gas is expelled from the clump and further core and star formation are quenched. The radiation driven winds of OB stars are metallicity dependent. Metal rich OB stars inject larger amount of energy into the clump than their low metallicity counterparts and thus help expel the gas on shorter timescales. This results in reduced final star formation efficiencies in metal rich clumps in comparison to their low metallicity counterparts. Both the final star formation efficiency and the gas expulsion timescales are combined for a grid of clump models with different masses and metallicities in order to calculate the star formation efficiency per unit time ($f_{*,ff}$) in this feedback regulated model of star formation. We calculate the characteristic value of $f_{*,ff}$ for a clump mass distribution associated with a gas surface density, Σ_g . This is combined with a description of the molecular mass fraction as a function of Σ_g and the assumption that there is a critical surface gas density ($\Sigma_g = 85 M_{\odot} \text{ pc}^{-2}$) above which the protocluster clumps and their parent giant molecular clouds switch from being pressurised from within by stellar feedback to being confined by the external interstellar medium pressure. The combination of these three elements allows us to construct the star formation laws in galaxies going from low gas surface densities up to the starburst regime. Our models exhibit a dependence on metallicity over the entire range of considered gas surface densities and fits remarkably well the observational data of Bigiel et al. (2008,2010) and Kennicutt (1998). This dependence on metallicity of the KS relation may well explain the scatter (or part of it) that is seen in the observationally derived relations.

I would like to thank the organizers of the workshop *Stellar and Interstellar physics for the modelling of the Galaxy and its components* for the opportunity to speak, and would like to acknowledge the generous financial support from the SF2A. S.D. and S.M. acknowledge the support provided by STFC grant ST/H00307X/1.

References

- Bigiel, F., Leroy, A., Walter, F. et al. 2008, *AJ*, 136, 2846
- Bigiel, F., Leroy, A., Walter, F. et al. 2010, *AJ*, 140, 1194
- Blanc, G. A., Heiderman, A., Gebhardt, K., Evans, N. J. II, & Adams, J. 2009, *ApJ*, 704, 842
- Boissier, S., Prantzos, N., Boselli, A., & Gavazzi, A. 2003, *MNRAS*, 346, 1215
- Bolatto, A. D., Leroy, A. K., Jameson, K. et al. 2011, *ApJ*, accepted, (arXiv:1107.1717)
- Boquien, M., Lisenfeld, U., Duc, P.-A. et al. 2011, *A&A*, 533, 19
- Braun, H., & Schmidt, W. 2011, *MNRAS*, submitted, (arXiv:1104.5582)
- Dib, S., Kim, J., & Shadmehri, M. 2007, *MNRAS*, 381, L40
- Dib, S., Brandenburg, A., Kim, J., Gopinathan, M., & André, P. 2008, *ApJ*, 678, L105
- Dib, S., Hennebelle, P., Pineda, J. E., Csengeri, T., Bontemps, S., Audit, E., & Goodman, A. A. 2010a, *ApJ*, 723, 425
- Dib, S., Shadmehri, M., Padoan, P., Maheswar, G., Ojha, D. K., & Khajenabi, F. 2010b, *MNRAS*, 405, 401
- Dib, S., Piau, L., Mohanty, S., & Braine, J. 2011, *MNRAS*, 415, 3439
- Dib, S. 2011a, *ApJ*, 737, L20
- Dib, S. 2011b, in *Stellar Clusters and Associations- A RIA workshop on GAIA*, (arXiv:1107.0886)
- Feldmann, R., Gnedin, N. Y., & Kravtsov, A. V. 2011, *ApJ*, 732, 115
- Fuchs, B., Jahrreiß, H., & Flynn, C. 2009, 137, 266
- Gnedin, N. Y., & Kravtsov, A. V. 2011, *ApJ*, 728, 88
- Heiner, J. S., Allen, R. J., & van der Kruit 2010, *ApJ*, 719, 1244
- Kennicutt, R. C. Jr. 1989, *ApJ*, 344, 685
- Kennicutt, R. C. Jr. 1998, *ApJ*, 498, 541
- Kim, C.-G., Kim, W.-T., Ostriker, E. C. 2011, *ApJ*, accepted, (arXiv:1109.0028)
- Krumholz, M. R. & McKee, C. F. 2005, *ApJ*, 630, 250
- Krumholz, M. R., & Thompson, T. A. 2007, *ApJ*, 669, 289
- Krumholz, M. R., McKee, C. F., & Tumlinson, J. 2009, *ApJ*, 699, 850
- Krumholz, M. R., McKee, C. F., & Tumlinson, J. 2009, *ApJ*, 693, 216
- Leitherer, C., Robert, C., & Drissen, L. 1992, *ApJ*, 401, 596
- Monaco, P., Murante, G., Borgani, S., & Dolag, K. 2011, *MNRAS*, accepted, (arXiv:1109.0484)
- Narayanan, D., Cox, T. J., Hayward, C. C., Hernquist, L. 2011, *MNRAS*, 412, 287
- Onodera, S., Kuno, N., Tosaki, T. et al. 2010, *ApJ*, 722, 127
- Padoan, P., & Nordlund, Å. 2002, *ApJ*, 576, 870
- Padoan, P., & Nordlund, Å. 2011, *ApJ*, 730, 40
- Papadopoulos, P. P. & Pelupessy, F. I. 2010, *ApJ*, 717, 1037
- Piau, L., Kervella, P., Dib, S., & Hauschildt, P. 2011, *A&A*, 526, 100
- Schruba, A., Leroy, A. K., Walter, F. et al. 2011, *AJ*, 142, 37
- Silk, J., & Norman, C. 2009, *ApJ*, 700, 262
- Tabatabaei, F. & Berkhuijsen, E. M. 2010, *A&A*, 517, 77
- Tutukov, A. V. 2006, *ARep*, 50, 526
- Vink, J. S., de Koter, A., & Lamers, H. J. G. L. M. 2001, *A&A*, 369, 574
- Vollmer, B., & Leroy, A. K. 2011, *AJ*, 141, 24
- Wong, T. & Blitz, L. 2002, *ApJ*, 569, 157

A SIGNATURE OF THE INTERNAL REIONISATION OF THE MILKY WAY IN THE RADIAL DISTRIBUTION OF ITS SATELLITES?

P. Ocvirk & D. Aubert¹

Abstract. We present a new semi-analytical model of the population of satellite galaxies of the Milky Way, aimed at estimating the effect of the geometry of reionisation at galaxy scale on the radial distribution of the satellites. In this model reionisation can be either: (1) externally driven by a bright but remote source such as the progenitor of Virgo, or (2) internally-driven, by the most massive progenitor of the Milky-Way. In scenario (1), satellites see a uniform UV background, while in scenario (2), the intensity of the UV background decreases with the distance to the center of the Milky Way. As a consequence, the gas of the inner satellites photo-evaporates faster than in the outer halo. We use simple recipes to model star formation, photo-evaporation and observational biases as in Kopusov et al. (2009). Both scenarios yield a model satellite population that matches the observed luminosity function and mass-to-light ratios. However, the predicted population for scenario (2) is significantly more externally distributed than for scenario (1) by about 0.1-0.2 dex in radius, resulting in a better match to the observations. This shows that the present radial distribution of satellites still bears the signature of the structure of the local UV field at reionisation. Therefore it is a promising tool for studying the reionisation epoch at galaxy-scale in the Milky Way and nearby galaxies resolved in stars with forthcoming large surveys.

¹ Observatoire astronomique de Strasbourg, France

COLLISION RATES AND THE DETERMINATION OF ATMOSPHERIC PARAMETERS

A. Spielfiedel¹, N. Feautrier¹, M. Guitou² and A. K. Belyaev^{1,3}

Abstract. Non-LTE modelisation of stellar atmospheres requires an accurate knowledge of collisional rate coefficients (mainly with H atoms) that compete with radiative rates to populate the atomic levels. In the framework of the SAM-GAIA project, we carry out, with colleagues from Uppsala, St. Petersburg and Nice, an interdisciplinary work combining quantum chemistry, collision physics and astrophysical modeling. Present studies concern collisional excitation of Mg and O by H-atoms. In the particular case of Mg, 15 electronic states of the MgH molecule as well as the associated couplings that mix the states during the collision were calculated. The resulting cross sections and rate coefficients point out the sensitivity of the results with the quantum chemistry data. Our detailed calculations show that the usual approximate formulae (Drawin, Kaulakys) lead to errors by factors up to 10^6 . Consequences on atmospheric parameters are analyzed.

Keywords: atomic data, line: formation, stars: abundances

1 Introduction

Non-LTE modeling implies a competition between radiative and collisional processes. The radiative data are well known thanks to the Opacity and the Iron projects. The influence of inelastic hydrogen atom collisions dominant in cold atmospheres on non-LTE spectral line formation has been, and remains to be, a significant source of uncertainty for stellar abundance analyses, due to the difficulty in obtaining accurate data for such low-energy collisions, either experimentally or theoretically. For lack of a better alternative, the classical so-called Drawin formula is often used. The question is: does the Drawin formula provide reasonable estimates of this process? After a brief presentation of the different steps used to obtain accurate quantum calculations for collisions with H atoms (Section 2), the comparison with the approximate formulae is made in section 3. Finally, preliminary conclusions on stellar abundance determination are drawn.

2 Quantum mechanical calculations

There are two steps to compute collisional rate coefficients : the first one is the calculation of the interaction potentials between the studied atom and H atom and the determination of the couplings between these potentials which allow collisional transitions. This concerns quantum chemistry, and the main difficulty is to build large basis sets adapted to the study of high excited states : it is a real challenge for quantum chemistry. Dynamics using these molecular data constitutes the second step. Accurate collisional cross sections and rate coefficients are obtained using the quantum close-coupling approach. In order to account for the so-called electron translation effect, the coupled-channel equations are solved by means of the reprojecion method (Belyaev 2010). Calculations were recently done for Li (Belyaev & Barklem 2003) and Na (Belyaev et al. 2010). Mg-H collisions and molecular interactions between O and H atoms are under study. Future work will be devoted to study H-collisions for atomic Ca, Ca^+ ion and possibly iron.

When the two colliding atoms come close together, they form temporarily a molecule whose electronic symmetry

¹ LERMA, Paris Observatory, 92195 Meudon

² MSME, Paris-Est University, 77454 Marne-la-Vallée

³ Department of Theoretical Physics, Herzen University, 191186 St Petersburg, Russia

and spin multiplicity depend on the electronic states of the two partners. In the case of magnesium we have considered all states up to the 1D and now 3D states. This gives more than twenty molecular states to be calculated. Fig. 1 displays the corresponding $^2\Sigma^+$ potentials as function of the internuclear distance R . The more interesting aspect for these potentials is the existence for the $^2\Sigma^+$ states of a strong mixing with the Mg^+-H^- ionic state. This leads to an ion-pair production channel for Mg in collision with H atoms and to the reverse reaction. For the Π and Δ states, no such perturbation occurs. This perturbation may lead to large coupling terms among the $^2\Sigma^+$ states, mainly at large R distances between high excited states (Guitou et al. 2010). So large cross sections and rate coefficients between Mg excited states are expected (Guitou et al. 2011), as well as Mg^+ formation through ion-pair production (Barklem et al. 2011). Preliminary results* show that the dominant rates are those between the closest final states, large rates between atomic levels of different spin symmetry and an important contribution of ion-pair production are found.

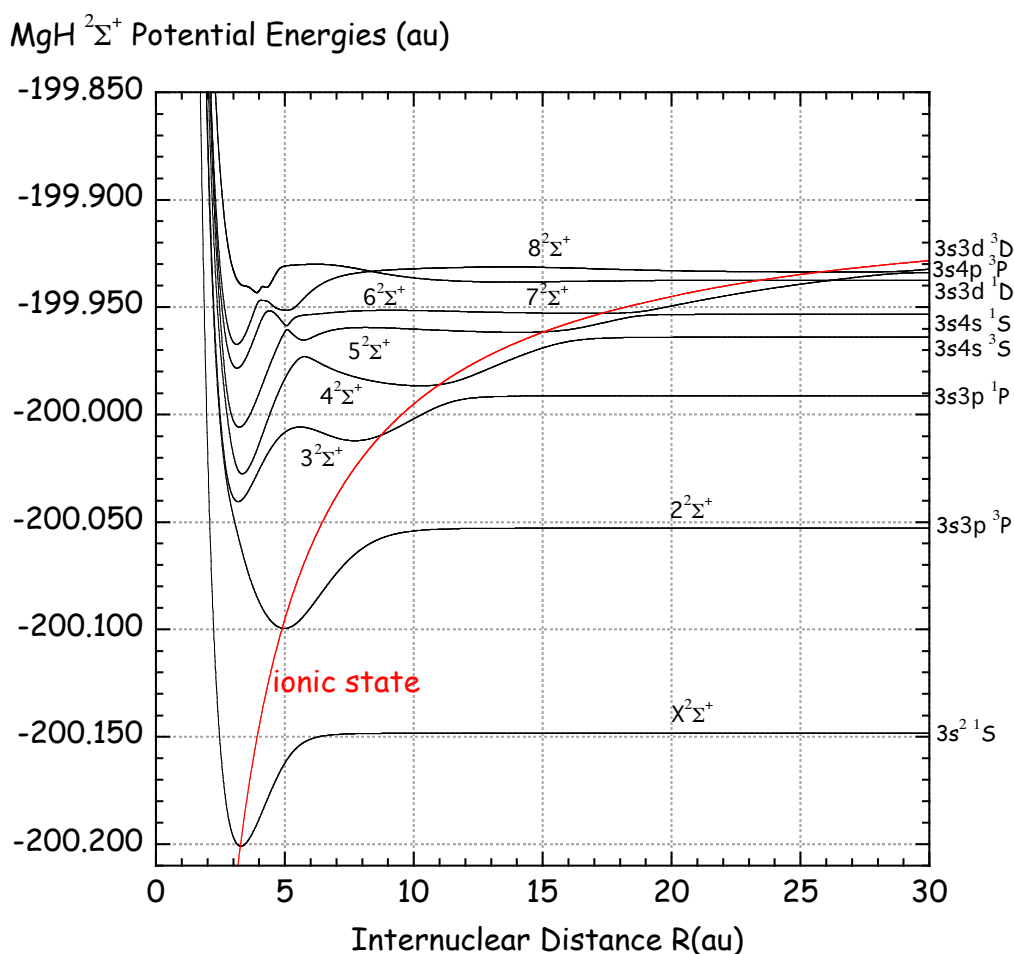


Fig. 1. $^2\Sigma^+$ electronic states as function of the internuclear distance. In red is displayed the ionic state

3 Comparison with approximate methods

It is important to compare accurate quantum rates with the results obtained using approximate formulae: the well known Drawin (1969) formula, which is an extension of the classical formula for ionization of atoms by electron impact, and the Kaulakys (1991) formula based on the free electron model applicable to Rydberg atoms. The Drawin formula gives rates proportional to the atomic oscillator strength (and thus equal to zero for spin

*Guitou, Belyaev, Barklem, Spielfiedel, Feautrier, unpublished 2011

forbidden transitions). In Fig. 2, which concerns collisions with Na atom (Lind et al. 2011), are plotted as function of the energy difference of the levels the ratio between Drawin and Kaulakys rates (right) and Drawin and quantum rates (left). Both approximate formulae give results far from the quantum one. This is expected as the detailed physics of the interactions is not at all introduced in the two models (Barklem et al. 2011). The same trends are found for collisions between H and Li and Mg atoms. The Drawin formula overestimates the rates by several orders of magnitude (up to 10^6). This is now well known, so in some modeling works the Drawin rates are multiplied by a corrective factor S_H ($0 \leq S_H \leq 1$). Comparison with accurate quantum results shows that S_H is different for different processes.

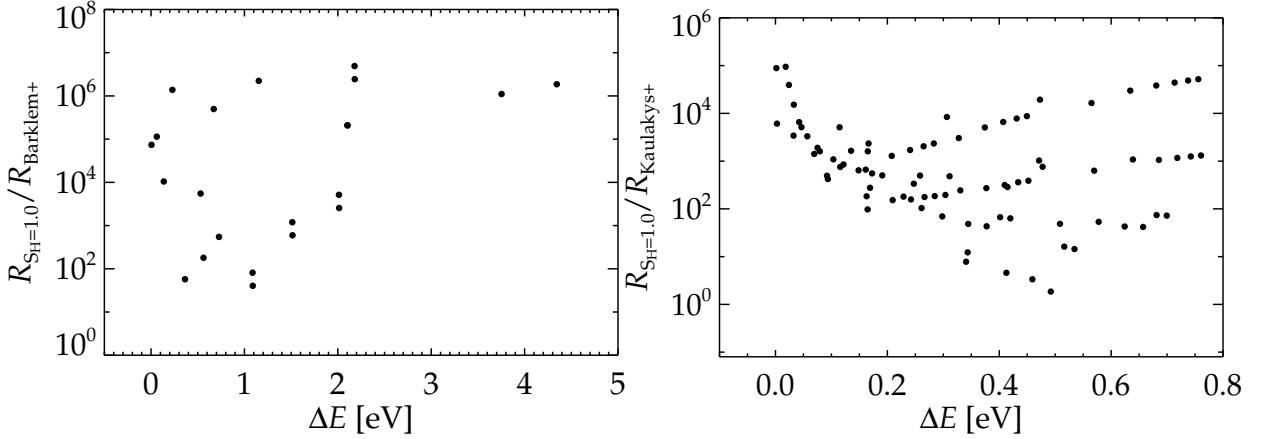


Fig. 2. Left: Drawin/quantum rates. **Right:** Drawin/Kaulakys rates.

4 Consequences on star atmosphere modeling

To date, no general conclusion on the effect of the new H-collisional rates seems possible as collisions compete with radiative processes for both excitation/deexcitation and ion-pair production of the species. As a consequence, the abundances depend non-linearly on many parameters: the physical conditions of the star atmosphere (temperature, gravity, metallicity), the number of atomic states included in the model, the radiative transfer and 1D or 3D modeling, the line considered for the diagnostics. However, some trends are available from recent studies on lithium, sodium, carbon and oxygen lines.

In a study relative to the Sun and to a sub giant metal-poor star, Barklem et al. (2003) show that H-collisions have a relatively small influence on the non-LTE predicted equivalent width of the resonance line for the Sun and larger effects for the metal-poor star. This is expected as collisional rate coefficients between the first atomic levels are very small and H atoms are not abundant in the Sun atmosphere. For a metal-poor star with low metallicity, the larger collisional effect is mainly due to mutual neutralisation with H^- which overpopulates the first levels. This last effect seems smaller for Na lines (Lind et al. 2011). In the absence of accurate H-collision rate coefficients for carbon and oxygen, Fabbian et al. (2006) and Fabbian et al. (2009) consider non-LTE abundance corrections using the Drawin formula with $S_H = 0$ (no collisions) and $S_H = 1$ (with H collisions). Both studies consider infra red lines, and large non-LTE effects (probably overestimated) are found for low metallicity stars.

5 Concluding remarks

H collisions play an important role for abundance determination of low metallicity stars when the diagnostics is obtained using lines between excited states. We note the importance of the 3D modeling. Preliminary results concerning lithium, sodium and magnesium show a large overestimation of the rate coefficients using the Drawin formula and the importance of ion-pair production by collisions with H atoms. These trends should be confirmed by studies on other atomic systems: work on oxygen is in progress and future work on neutral and ionized calcium is planned.

We would like to acknowledge support from French «Action Spécifique Gaia, Programme PNPS of the CNRS», the Chemical Institute of the CNRS, as well as collaboration with Paul Barklem (Uppsala, Sweden) and the SAM/GAIA team.

References

- Barklem, P., Belyaev, A., & Asplund, M. 2003, *A&A*, 409, L1
- Barklem, P., Belyaev, A., Feautrier, N., et al. 2011, *A&A*, 530, A94
- Belyaev, A. 2010, *Phys. Rev. A*, 82, 060701(R)
- Belyaev, A. & Barklem, P. 2003, *Phys. Rev. A*, 68, 062703
- Belyaev, A., Barklem, P., Dickinson, A., & Gadéa, F. 2010, *Phys. Rev. A*, 81, 032706
- Drawin, H. 1969, *Zeitschrift fur Physik*, 225, 483
- Fabbian, D., Asplund, M., Barklem, P., Carlsson, M., & Kiselman, D. 2009, *A&A*, 500, 1221
- Fabbian, D., Asplund, M., Carlsson, M., & Kiselman, D. 2006, *A&A*, 458, 899
- Guitou, M., Belyaev, A., Barklem, P., Spielfiedel, A., & Feautrier, N. 2011, *J. Phys. B*, 44, 035202
- Guitou, M., Spielfiedel, A., & Feautrier, N. 2010, *Chem. Phys. Letters*, 488, 145
- Kaulakys, B. 1991, *J. Phys. B*, 24, L127
- Lind, K., Asplund, M., Barklem, P., & Belyaev, A. 2011, *A&A*, 528, A103

STELLAR AGES IN THE CONTEXT OF GAIA

D. Valls-Gabaud¹

Abstract. After a short review on past and current techniques, the Bayesian statistical framework for the inference of stellar parameters –such as ages– is presented and applied to the three key cases of single stars, detached binaries, and stellar clusters. The role of prior probability distribution functions in parameters which are not measured for some subsets of the catalogue is illustrated through simulated samples and discussed.

¹ Observatoire de Paris

TOWARDS A 3D VIEW OF THE GALACTIC INTERSTELLAR MEDIUM WITH PLANCK, HERSCHEL AND GAIA

D.J. Marshall¹

Abstract. Thanks to the spatial missions Planck and Herschel, we are currently exploring a previously unknown part of the Galaxy: the cold and dense interstellar medium (ISM). The interpretation of these results requires detailed knowledge of the spatial distribution of its dust and gas, as well as the surrounding stars. Accurate distance and extinction measurements from the Gaia satellite will allow us for the first time to truly explore the ISM, and therefore stellar birthplaces, in three dimensions.

¹ Institut de Recherche en Astrophysique et Planétologie, Toulouse, France

GALACTIC DUST PROPERTIES

D. Paradis^{1,2} and the Hi-GAL team

Abstract. Recent studies have shown evidence for variations in the dust emissivity law with temperature and wavelength. A recent dust emission model, called TLS model (for two-level systems), based on the description of the disordered internal structure of the amorphous dust grains has been developed to interpret observations in the far-infrared/submillimeter (FIR/submm) domain. A recent work focusing on the comparison between data of the diffuse interstellar medium seen by FIRAS-WMAP, as well as Archeops compact sources, with the TLS model allowed us to constrain the model parameters characterizing the general Galactic dust properties. Using the newly available Herschel/Hi-GAL data of the inner Galactic plane, we report a 500 μm emissivity excess in the peripheral parts of the Galactic plane, that can reach up to 20% of the emissivity. Results of the TLS modeling indicate significant changes in the dust properties from the central to peripheral parts of the Galactic plane.

Keywords: dust, extinction, infrared, ISM

1 Introduction

The study of the extended far-infrared (FIR) and submillimeter (submm) sky emission is a relatively young subject. This wavelength range is dominated by emission from large silicate-based interstellar grains, that dominate the total dust mass and radiate at thermal equilibrium with the surrounding radiation field. Their emission is often modeled using a modified black body at a given dust temperature and a fixed spectral index (β). The FIR/submm emission is routinely used to infer total gas column density and mass of objects ranging from molecular clouds to entire external galaxies, assuming that dust faithfully traces the gas. The data analysis of balloon (PRONAOS, Archeops) and satellite (FIRAS, WMAP) data has revealed that the FIR/submm emission cannot be explained by a simple extrapolation of the mid-IR emission:

- Dust emissivity appears to be wavelength-dependent with the emission spectrum flattening in the submm as compared to a modified black-body emission (Reach et al. 1995; Finkbeiner et al. 1999; Galliano et al. 2005; Paladini et al. 2007).
- Dust emissivity appears to be temperature-dependent, the emissivity spectra being flatter with the increasing dust temperature (Dupac et al. 2003; Désert et al. 2008).

Similar variations are now seen in laboratory spectroscopic experiments on amorphous dust analogs (Agladze et al. 1996; Mennella et al. 1998; Boudet et al. 2005). In particular, recent studies on three analogs of amorphous silicate Mg_2SiO_4 , MgSiO_3 , and $\text{CaMgSi}_2\text{O}_6$ reveal that this temperature and wavelength dependence of the absorption is observed on all the samples, but disappear when the same samples are annealed until crystallization (Coupeaud et al. 2011).

These analyses indicate that the T_d - β variations are likely to result from intrinsic dust properties that can be reproduced for the first time by a dust emission model such as the two-level systems (TLS) one.

Dust emissivity also appear to be environment-dependent, with an absolute emissivity value in the far-IR increased in cold and dense environments, as seen in the Taurus cloud (Stepnik et al. 2003; Planck Collaboration 2011a).

¹ Université de Toulouse; UPS-OMP, IRAP, Toulouse, France

² CNRS; IRAP, 9 av. du Colonel Roche, BP 44346, 31028, Toulouse, cedex 4, France

2 Evolution of dust properties from diffuse to dense medium

We analyze the dust emission from the outer Galactic plane using DIRBE, Archeops and WMAP data from 100 μm to 3.2 mm. We perform a correlation study of the FIR-mm emission with gas tracers in individual regions, and derive the average equilibrium temperature of large dust grains in both molecular and atomic phases in a set of regions along the Galactic plane. We use this temperature to derive the emissivity spectra for each phase and region.

We show that the emissivity spectra are always steeper in the FIR ($\lambda < 600 \mu\text{m}$) and flatten in the submm and mm. In regions where dust is significantly colder in the molecular phase than in the surrounding atomic medium, we produce an increase in the emissivity by a factor of $\simeq 3$ in the FIR (see Fig. 1, panel A). However, we showed that the emissivity increase is restricted to the FIR range; the emissivity spectra for the dust in the atomic and molecular phases become comparable again in the submm and mm wavelength range.

We interpret the FIR emissivity excess in the molecular clouds containing cold dust as being caused by the coagulation of large grains into fractal aggregates. The fact that the emissivities do reconcile in the submm could be related to the amorphous nature of the grains contained in the aggregates (see the following Section).

The full description of this analysis is presented in Paradis et al. (2009).

3 A model of amorphous dust: the TLS model

The recent TLS model (Mény et al. 2007) is based on the solid-state physics model developed to interpret specific properties of the amorphous solids identified in laboratory data. As a consequence, it is expected to apply with a high degree of universality, and not to be sensitive to the exact chemical nature of the dust. The disordered charge distribution (DCD) part of the model describes the interaction between the electromagnetic wave and acoustic oscillations in the disordered charge of the amorphous material (Vinogradov, 1960; Schlomann, 1964). This charge-disorder is observed on nanometer scale and is described here by a single charge correlation length. The TLS part models the disorder at atomic scale by a distribution of asymmetric double-well potential (ADWP). Each ADWP can be viewed as to close configurations of atoms or group of atoms in the disordered structure (Phillips 1972, 1987; Anderson et al. 1972). The TLS model describes the interaction of the electromagnetic wave with a simple distribution of two-level systems that represent the lowest states (ground states) of the ADWP. Both DCD and TLS phenomena have been first applied by Bösch (1978) to explain the observed temperature dependence of the absorption of some silica-based glasses in the FIR/mm. Three interaction mechanisms, which all depend on temperature, can occur in such a population of TLS sites: a resonant absorption, and two relaxation processes identified as “tunneling relaxation” and “hopping relaxation”.

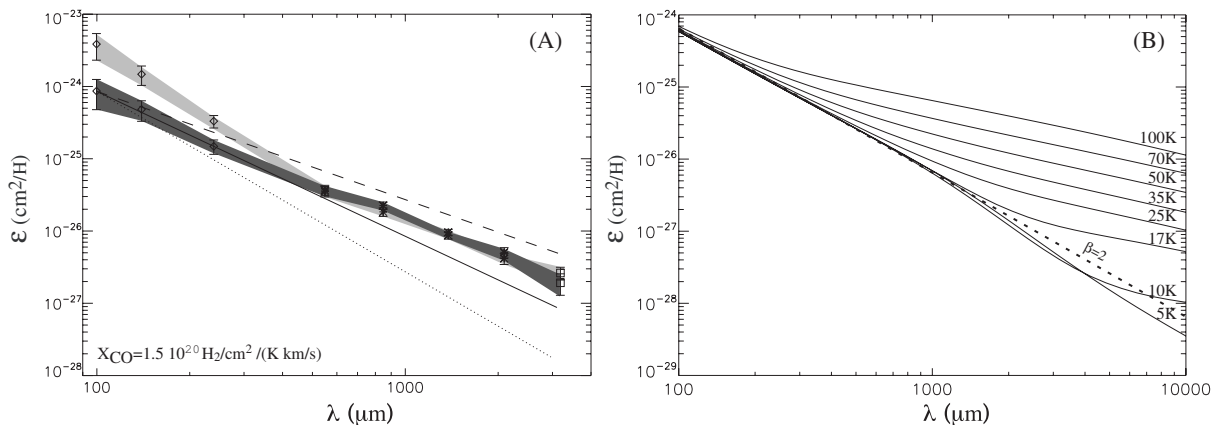


Fig. 1. Left: Panel (A): Median dust emissivity SEDs for regions with dust significantly colder in the molecular phase than in the surrounding atomic medium. The molecular emissivity has been scaled to match that of the atomic phase in the range 550 μm -3 mm. The DIRBE, Archeops and WMAP data correspond to diamond, star and square symbols, respectively. The shaded areas show the $\pm 1\text{-}\sigma$ dispersion around each emissivity SED, in dark and light grey for the atomic and molecular phase. For comparison, power-law spectra with $\beta=1.5$ (dashed), $\beta=2$ (solid) and $\beta=2.5$ (dot) are shown, normalized to the atomic emissivity at 100 μm . **Right:** Panel (B): Predicted emissivity with the TLS model, as a function of wavelength for different temperatures. The dashed line shows a λ^{-2} emissivity power-law.

The TLS model is compared to astrophysical data, such as the FIRAS/WMAP and Archeops data. The FIRAS/WMAP spectrum represents the diffuse interstellar medium in the stellar neighborhood, whereas the Archeops data characterize dust properties in a variety of compact sources, where a significant inverse relationship between the dust temperature and the emissivity spectral index had been shown. We performed a χ^2 minimization to determine standard values for the parameters of the TLS model selected to capture the spectral and temperature variations in the model. These free parameters are the dust temperature (T_{TLS}), the charge correlation length (l_c) that controls the wavelength where the inflection point between the two $\beta = 2$ and $\beta = 4$ ranges occurs, the intensity factor of the TLS processes (A) with respect to the DCD effect, and the intensity factor of the TLS/hopping process (c_Δ). Results indicate that emission in the submm/mm is dominated by the hopping relaxation. According to the model, the BG emission in the FIR/mm domain depends on wavelength and temperature, which is fundamental both for dust mass determination from FIR/submm measurements but also for component separation. Using the best-fit parameters ($T_{TLS} = 17.26$ K, $l_c = 13.4$ nm, $A = 5.81$, and $c_\Delta = 475$) allowing reproduction of both the emission from the diffuse medium and the compact sources, the model predicts significant β variations for temperatures between 5 and 100 K, with a maximum value of 2.6 at 2 mm. The TLS model is presently the only astrophysical model able to predict β variations with temperature and wavelengths, as observed in both observational and laboratory data. The dust emissivity can be seriously underestimated if its variations with temperature and wavelength are not taken properly into account (see Fig. 1, panel B), generally inducing overestimates of the dust mass. We also predict dust emissivities in the IRAS 100 μm , Herschel, and Planck bands for temperatures between 5 and 100 K, which are useful for comparison with the Planck and Herschel data.

The full description of this analysis is presented in Paradis et al. (2011a).

4 Dust properties along the Galactic plane using Hi-GAL data

We investigate variations in the spectral index of the dust emissivity, with temperature and wavelength, in the inner Galactic plane, using Herschel observations in two Hi-GAL ($160 \mu\text{m} < \lambda < 500 \mu\text{m}$) fields, centered at $l = 30^\circ$ and $l = 59^\circ$, acquired during the Herschel Science Demonstration phase, combined with the IRIS 100 μm data, $4'$ angular resolution. We fit the spectral energy distribution (SEDs) for each pixel of the two fields with two independent methods (least-square fit and maximum likelihood using a Monte Carlo Markov Chain algorithm, hereafter MCMC), deriving simultaneously the emissivity spectral index and the dust temperature by adjusting a modified blackbody function to the data. The results are similar with both methods. Using the MCMC method we computed the 68% likelihood contours for each point. We find a T_d - β inverse correlation, with the local variation going from 1.8 to 2.6 for temperatures between 14 and 23 K, shown for the first time in the inner Galactic plane. The median value of β is similar in both fields, equal to 2.3, slightly higher than the usual reference value of 2.

With the newly released Hi-GAL data combined with the IRIS 100 μm data, we perform an analysis of the emissivity variations along the Galactic plane. Changes in the emissivity spectra are interpreted in terms of the TLS model (see Fig. 2). We report:

- A 500 μm emissivity excess with respect to the predictions of a modified black-body model with $\beta=2$, in the peripheral parts of the Galactic plane ($35^\circ < |l| < 70^\circ$) covered by the data. This excess can represent up to 16% to 20% of the total emission. A similar excess has recently been evidenced in the Large Magellanic Cloud (Gordon et al. 2010; Galliano et al. 2011)
- Warmer dust temperatures in the central ($|l| > 35^\circ$) than in the peripheral Galactic regions.
- A flattening of the emissivity spectra in the range 100-500 μm with increasing dust temperature, that does not result from temperature mixture along the line of sight.
- The 500 μm emissivity excess can be explained by an increase in the intensity of the TLS processes, indicating a larger degree of amorphization of the grains in the peripheral parts of the Galactic plane.
- Dust properties along the Galactic plane seem to be different from those of the solar neighborhood, the excess being smaller in the latter than expected from an extrapolation of the Galactic plane behavior.

The full description of this analysis is presented in Paradis et al. (2011b).

5 Conclusions

Understanding emission of the big grains dust component is not easy since it varies with wavelength, temperature and environment. We evidenced variations in the emissivity from diffuse to dense medium, from the solar

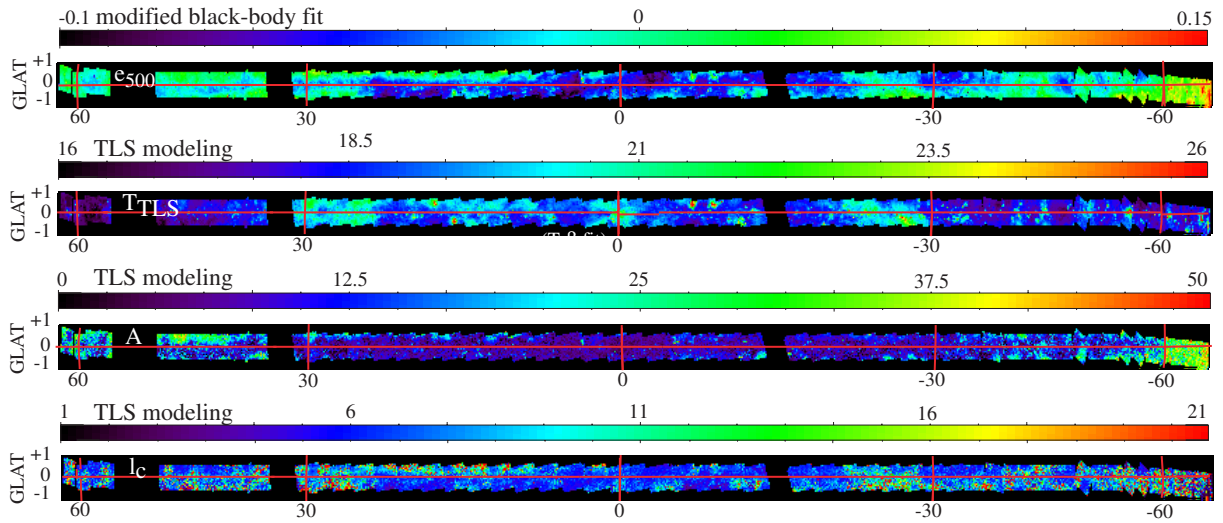


Fig. 2. From top to bottom: 500 μm emissivity excess (e_{500}), and results of the TLS modeling: dust temperature (T_{TLS}) in K, intensity of the TLS processes (A), correlation length (l_c) in nm.

neighborhood to the Galactic plane, and from the central to the peripheral parts of the inner Galactic plane. The presence of submm excess reveals some variations in the optical properties of the interstellar grains. Comparison between astrophysical observations/laboratory data and TLS modeling can lead to deduce more information on the amorphous state of the grain itself.

References

- Agladze, N. I., Sievers, A. J., Jones, S. A., et al. 1996, *ApJ*, 462, 1026
 Anderson, P. W., Halperin, B. I., & Varma, C. M. 1972, *Phil. Mag.*, 25, 1
 Bösch, M. 1978, *Physical Review Letters*, 40, 879
 Boudet, N., Mutschke, H., Nayral, C., et al. 2005, *ApJ*, 633, 272
 Coupeaud, A., et al. 2011, *A&A*, accepted, arXiv1109.2758
 Désert, F.-X., Macías-Pérez, J. F., Mayet, F., et al. 2008, *A&A*, 481, 411
 Dupac, X., Boudet, N., Giard, M., et al. 2003, *A&A*, 404, L11
 Finkbeiner, D. P., Davis M., Schlegel D.J. 1999, *ApJ*, 524, 867
 Galliano, F., Madden, S. C., Jones, A. P., et al. 2005, *A&A*, 434, 867
 Galliano, F., et al. 2011, *A&A*, accepted
 Gordon, K., et al. 2010, *A&A*, 518, 89
 Mennella, V., Brucato, J. R., Colangeli, L., et al. 1998, *ApJ*, 496, 1058
 Mény, C., et al. 2007, *A&A*, 468, 171
 Paladini, R., et al. 2007, *A&A*, 465, 839
 Paradis, D., Bernard, J.-P., & Mény, C. 2009, *A&A*, 506, 745
 Paradis, D., et al. 2010, *A&A*, 520, 8
 Paradis, D., Bernard, J.-P., Mény, C., & Gromov, V. 2011a, *A&A*, in press, arXiv1107.5179
 Paradis, D., et al. 2011b, *A&A*, submitted
 Phillips, W. 1972, *J. Low Temp. Phys.*, 11, 757
 Phillips, W. 1987, *Rep. Prog. Phys.*, 50, 1657
 Planck Collaboration 2011a, *Planck early results 25*, *A&A*, accepted, arXiv1101.2037
 Reach, W. T., et al. 1995, *ApJ*, 451, 188
 Stepnik, B., Abergel, A., Bernard, J.-Ph., et al. 2003, *A&A*, 398, 551

**Atelier A03 commun ASGAIA-PNPS-PNCG-PCMI
SF2A-SEA**

**Stellar and Interstellar physics for the modelling of the
Galaxy and its components**

SF2A 2011, 20-21 juin 2011, Paris

Posters

- David Bancelin** Orbits of Potentially Hazardous Asteroids using Gaia and ground-based observations
- Roger Cayrel et al.** The H α Balmer line as an effective temperature
- Laurent Chemin et al.** Calibration of the Gaia RVS from ground-based observations of candidate standard stars
- Nicolas Gaudin & Hervé Wozniak** Dust mass in simulations of galaxies
- Céline Guédé et al.** Determination of the ages of stars from their position in the HR diagram
- Jean-Louis Halbwachs et al.** New SB2 binaries for accurate stellar masses with Gaia
- T. Kılıçoğlu et al.** Chemical abundances for A-type dwarfs in the young open cluster M6
- Thomas Masseron** Carbon-enhanced metal-poor stars: witnesses of the first generation of stars
- David Montes et al.** Stellar parameters and chemical tagging of nearby FGK stars: testing membership to stellar kinematic groups
- Deborah Paradis et al.** Spitzer characterization of dust in the ionized medium of the Large Magellanic Cloud
- Hélène Posbic et al.** SPADES: a Stellar PArameters DEtermination Software
- Arvind S. Rajpurohit et al.** The physical parameters of the low-mass multiple system LHS1070 from spectral synthesis analysis
- Isabelle Ristorcelli et al.** Planck Early results: The first all-sky survey of Galactic cold clumps
- Monique Spite et al.** Preliminary determination of the Non-LTE Calcium abundance in a sample of the extremely metal-poor stars

ORBIT OF POTENTIALLY HAZARDOUS ASTEROIDS USING GAIA AND GROUND-BASED OBSERVATIONS

D. Bancelin¹, D. Hestroffer¹ and W. Thuillot¹

Abstract. Potentially Hazardous Asteroids (PHAs) are Near Earth Asteroids characterized by a Minimum Orbital Intersection Distance (MOID) with Earth less to 0,05 A.U and an absolute magnitude $H < 22$. Those objects have sometimes a so significant close approach with Earth that they can be put on a chaotic orbit. This kind of orbit is very sensitive for exemple to the initial conditions, to the planetary theory used (for instance JPL's model versus IMCCE's model) or even to the numerical integrator used (Lie Series, Bulirsch-Stoer or Radau). New observations (optical, radar, flyby or satellite mission) can improve those orbits and reduce the uncertainties on the Keplerian elements.

Keywords: Gaia mission, b-plane, Potentially Hazardous Asteroids, orbit determination, astrometry

1 Introduction

Gaia is a 5-years astrometric mission scheduled for spring 2013. The main aim is to make a three dimensional map of our Galaxy. There are a lot of science outcomes from this mission: a better understanding of the star formation and the history of the Milky Way; study on stellar astrophysics, on the Galactic structure and on Binaries and Brown dwarfs. The Solar System Science goal is to map thousand of Main Belt Asteroids (MBAs), Near Earth Asteroids (NEAs) (including comets) and also planetary satellites. The principal purpose is orbital determination (better than 5 mas astrometric precision), determination of asteroid mass, spin properties and taxonomy. Besides, Gaia will be able to discover a few objects, in particular NEAs in the region down to the solar elongation (45°) which are harder to detect with current ground-based surveys. The aim of this study is to analyse the impact of Gaia data on the orbit of Potentially Hazardous Asteroids (PHAs) and also the advantage of combining space-based and ground-based data.

2 Statistical observations of NEAs by Gaia

During the 5-years mission, Gaia will continuously scan the sky with a specific strategy: objects will be observed from two lines of sight separated with a constant basic angle. Five constants already fixed determinate the nominal scanning law but two others are still free parameters: the initial spin phase (influencing the date of observations) and the initial precession angle (influencing the number of observations). These latter will be fixed at the start of the nominal scientific outcome (possibility of performing tests of fundamental physics) together with operational requirements (downlink to Earth windows). Hence several sets of observation will be provided according to the initial precession angle. Figure 1 shows the number of NEAs that would be observed by Gaia. This number represents about 30% of the NEAs population.

3 Astrometry for known PHAs

Asteroid Apophis is a PHA discovered in 2004 and was revealed to be a threatening asteroid for the Earth, since, because of a deep close encounter ($\sim 38000\text{km}$) with Earth in 2029, there is some risks of collision mainly in 2036. In order to better prepare future space missions towards this asteroid, it is important to well quantify the uncertainty in 2029. To better represent the state of an asteroid approaching the Earth, we better use the

¹ Institut de Mécanique Céleste et de Calcul de Éphémérides, 77 Avenue Denfert-Rochereau 75014 Paris, France

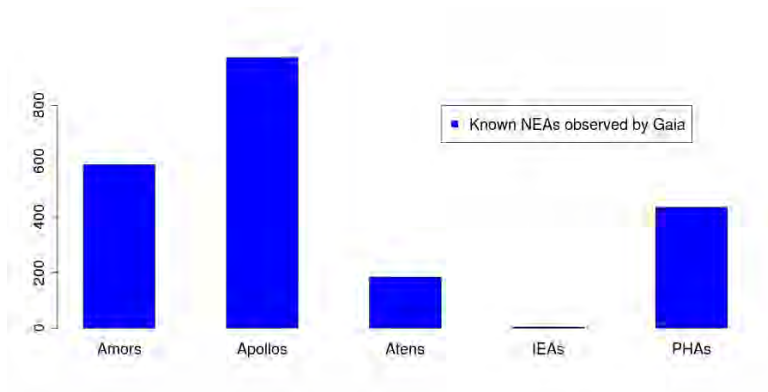


Fig. 1. Number of known NEAs possibly observed by Gaia

b-plane or target plane (Valsecchi et al. 2003) . It passes through the Earth’s center and is perpendicular to the geocentric velocity of the asteroid. In this plane, the asteroid will have two geocentric coordinates (ξ, ζ) . Thus the projection of the 6-dimension region uncertainty of the Keplerian elements in the 2029-b-plane is a 3σ ellipse uncertainty. Fig. 2 represents the 3σ ellipse in (ξ, ζ) in the 2029-b-plane with (blue) and without (grey) additional Gaia data. For completeness, we represented primary(\star) and secondary keyholes leading at collision at the ascending (\blacksquare) and descending node (\blacksquare). Keyholes are regions in the b-plane of 2029 where the asteroid has to pass in order to collide the Earth at some dates indicated in Fig. 2.

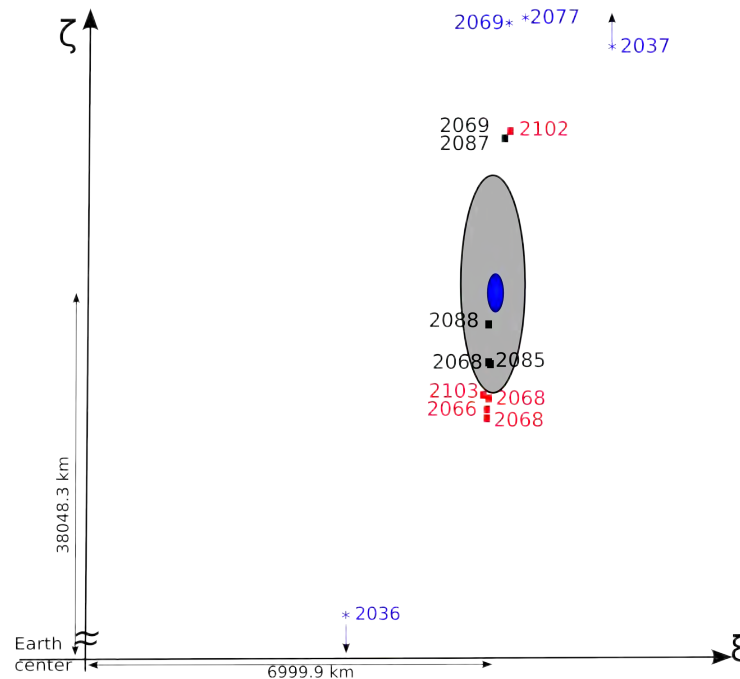


Fig. 2. 3σ ellipse uncertainty in the 2029-b-plane centered in the (ξ, ζ) nominal value: In blue: using Gaia data; in grey: without Gaia data. The positions of the center of keyholes are also represented.

As shown in the Tab. 1, Gaia data enable to reach the kilometer knowledge level on the accuracy of the orbit of Apophis in 2029.

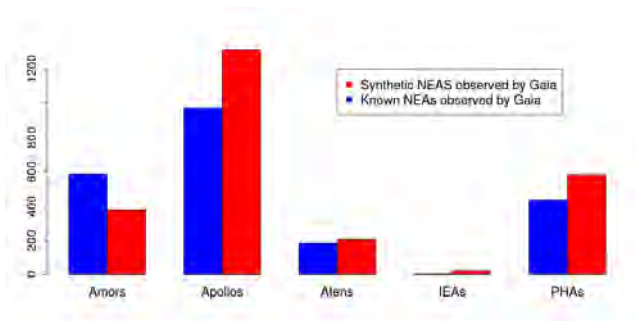
4 Astrometry for newly discovered PHAs

During the mission, we do expect Gaia to observe some new objects and among them new PHAs. But Gaia is not a follow-up mission and as a consequence, the newly discovered objects can rapidly be lost if no recovery process

Table 1. Impact of Gaia data on the size of the 3σ ellipse uncertainty in the 2029-b-plane.

| b-plane uncertainty | Ground-based data only | Ground-based and Gaia data |
|---------------------|------------------------|----------------------------|
| σ_ξ (km) | 10.5 | 0.3 |
| σ_ζ (km) | 87 | 1.4 |

of those potential alerts is done from Earth. We would like first to quantify the number of alerts expected. In a first approach, using a 20000-synthetic population of NEAs (Bottke et al. 2002) and comparing with Fig.1, we see that only a small number of alerts is expected: around one alert every four days. The statistical details are represented in Fig.3. Because of the scanning law, Gaia will provide only two (α, δ) observations (before being re-observed) and separated by $\Delta t \sim 1.5$ hours. When observing a new object, Gaia will send, within 24 h, the coordinates to Earth, where a preliminary short arc orbit can be computed, using Statistical Ranging method (Virtanen et al. 2001)

**Fig. 3.** Number of known and synthetic NEAs that would be observed by Gaia during the 5-years mission.

This yields to an (α, δ) prediction in the sky plane (\circ). As the (α, δ) distribution is large, we can extract its maximum likelihood (ML) and center a typical field of view ($24' \times 24'$) on this ML (\bullet) in order to know where to look in the sky and how long the object can still be recovered. This test is done with an hypothetical asteroid (1620) Geographos that would be discovered by Gaia. In Fig. 4, when comparing with the expected position of Geographos (\blacktriangledown), we can see that up to 7 days, the asteroid may be lost with this size of field of view.

When recovered, this asteroid will be followed at least one night (and preferably more) in order to have an orbit improvement. Fig. 5 shows the advantage of combining, in real-time, ground-based (with 0.5 arcsec accuracy) and space-based data (5 mas accuracy). One can see that the (α, δ) distribution is drastically reduced when adding additional ground-based observations (\circ).

5 Conclusions

Even if Gaia will not be a big NEAs discoverer, it will provide unprecedented accuracy for NEAs orbit's improvement. Besides, this study can be continued considering the astrometric reduction due to the stellar catalogue provided by Gaia. As a matter of fact, this catalogue will be more precise and dense and almost free of zonal errors. Thus, classical ground-based astrometry (and concerning hence more object down to fainter magnitude) will be improved.

The author are grateful to the DPAC members and CU4.

References

- Bottke, W. F., Morbidelli, A., Jedicke, R., et al. 2002, *Icarus*, 156, 399
Valsecchi, G. B., Milani, A., Gronchi, G. F., & Chesley, S. R. 2003, *A&A*, 408, 1179
Virtanen, J., Muinonen, K., & Bowell, E. 2001, *Icarus*, 154, 412

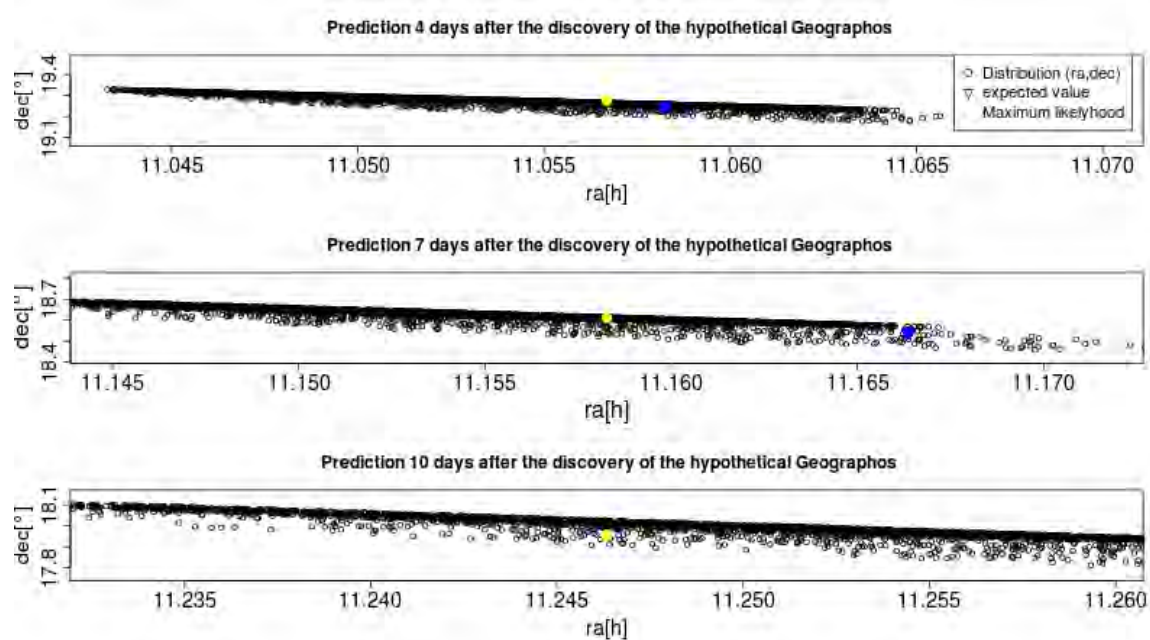


Fig. 4. Prediction on the sky plane of the hypothetical Geographos, until 10 days after its discovery by Gaia.

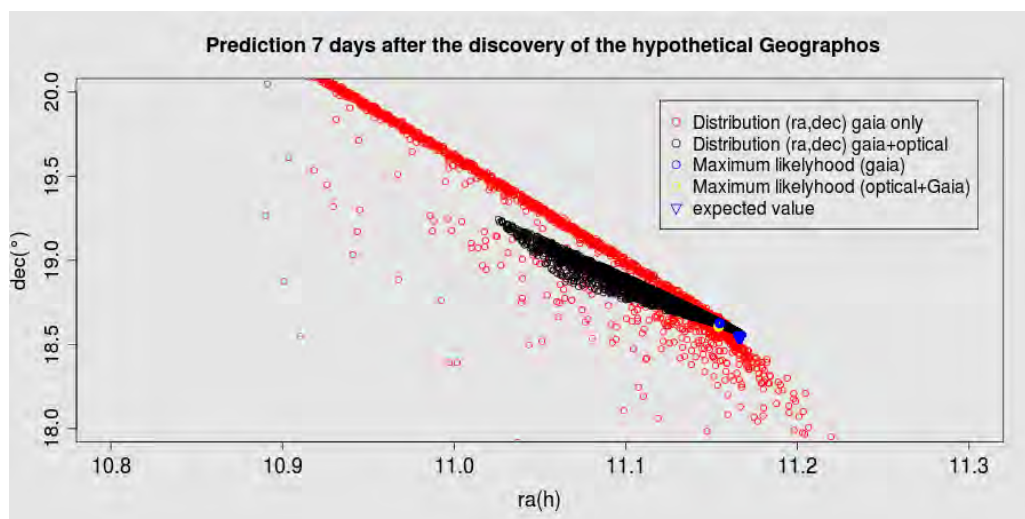


Fig. 5. Distribution (α, δ) combining ground and space-based data (\circ), 7 days after the hypothetical discovery of asteroid Geographos.

THE H α BALMER LINE AS AN EFFECTIVE TEMPERATURE CRITERION

R. Cayrel¹, C. Van't Veer-Menneret², N. F. Allard^{1,3} and C. Stehlé⁴

Abstract. For eleven stars with an accurate effective temperature derived from their apparent angular diameter we determine the effective temperature of the Kurucz Atlas9 model that provides the best fit of the computed theoretical H α profile (using the recent theoretical advances) with the corresponding observed profile, extracted from the S4N spectroscopic database. The two sets of effective temperatures have a significant offset, but are tightly correlated, with a correlation coefficient of 0.9976. The regression straight line of T_{eff}(direct) versus T_{eff}(H α) enables us to reach the true effective temperature from the spectroscopic observation of the H α profile, with an rms error of only 30 K. This provides a way of obtaining the true effective temperature of a reddened star.

Keywords: stars:atmospheres, stars:fundamental parameters, line:profile

1 Introduction

Already many authors have used the H α Balmer line as effective temperature criterion. Two events justify to derive a new calibration of H α versus effective temperature.

The first one is a continuous improvement in the physics of the broadening of the line, from 1999 to 2008. The second one is the enormous gain in the accuracy of apparent angular diameter measurements by interferometric methods. This enables to derive the effective temperatures of a dozen of stars with an accuracy of the order of one per cent by the relation:

$$T_{\text{eff}} = (4/\sigma)^{1/4} f_{\text{bol}}^{1/4} \theta^{-1/2}$$

where σ is the Stefan-Boltzmann constant, and f_{bol} and θ are respectively the apparent bolometric flux and limb-darkened angular diameter of the object. This is the so-called direct method, less model dependent than the Infrared Flux Method, largely used before. Our work has been to connect the effective temperature obtained by the direct method, to the effective temperature of the model giving the best fit between the computed and the observed profile of H α for this dozen of stars.

2 Effective temperatures from the H α fitting procedure

2.1 Observations

We selected the spectra of the S4N spectral library (Allende Prieto et al. 2004) for the 10 stars having apparent angular diameters measurements better than 2 per cent. These spectra are very suited for the study of the H α wings, usually difficult to get with cross-dispersed spectrographs.

2.2 Model atmosphere

We used Kurucz ATLAS9, BALMER9 codes, after incorporating the Stark broadening of Stehlé & Hutcheon (1999) and the collisional broadening by neutral H of Allard et al. (2008). We used a mixing length over pressure scale height ratio of 0.5.

¹ Observatoire de Paris, GEPI, UMR 8111, CNRS, 61, Avenue de l'Observatoire, F-75014 Paris, France

² Observatoire de Paris, GEPI, 5 Place J. Janssen, 92195 Meudon, France

³ Institut d'Astrophysique de Paris, F-75014 Paris, UMR 7095, CNRS, 98bis Boulevard Arago, F-750014 Paris, France

⁴ Observatoire de Paris, LERMA, 5 Place J. Janssen, 92195 Meudon, France

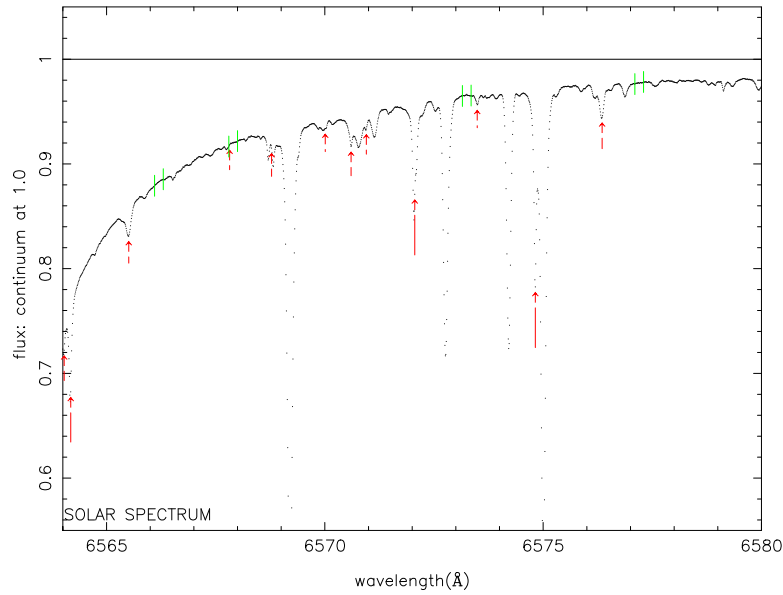


Fig. 1. Red wing of the observed solar $H\alpha$ profile. The windows free of other lines contamination are indicated by a couple of green vertical lines.

2.3 Fitting procedure

As done by Barklem et al. (2002) we have selected windows, where $H\alpha$ is not contaminated by other stellar lines (see Fig. 1). The telluric lines, indicated by red arrows, have been a worry as they move with the radial velocity of the object and must be avoided too. Some windows may be lost. Taking the parameters gravity and metallicity from the PASTEL database (Soubiran et al. 2010), we vary the effective temperature of the model until we get the best fit with the observed profile. See examples in Fig. 2. The procedure is repeated for the selected ten spectra from the S4N library plus the Sun.

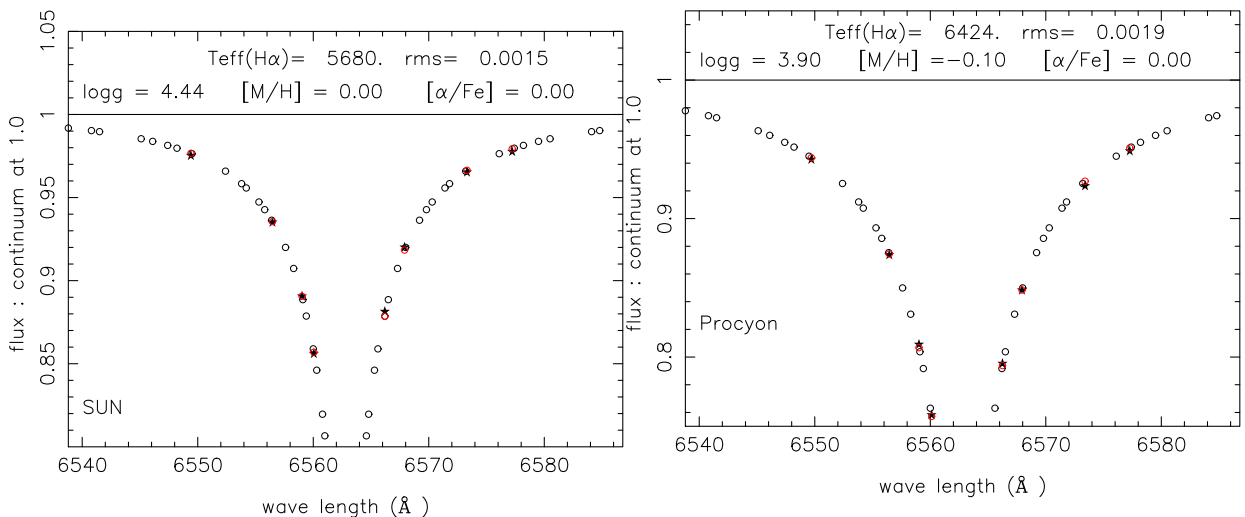


Fig. 2. Left: Fitting of the computed to the observed fluxes of the solar $H\alpha$ profile.

Right: Fitting of the computed to the observed fluxes on the $H\alpha$ profile of Procyon.

Open circles are the theoretical profile, the red ones corresponding to the wavelength of the observed points represented by full black stars.

3 $T_{\text{eff}}(\text{direct})$ and results

The apparent angular diameters have been taken from the literature. Most of them come from the Mount Wilson interferometer (now CHARA) and a few from the ESO VLTI. A list of them can be found in Casagrande et al. (2010). The apparent bolometric magnitudes have been derived from colour indices by relations established by Casagrande et al. (2010). The dispersion of the points around the regression line of $T_{\text{eff}}(\text{direct})$ versus $T_{\text{eff}}(\text{H}\alpha)$ is remarkably small, with a root mean square deviation of only 30 K. The relation between the two sets of effective temperatures is represented by:

$$T_{\text{eff}}(\text{direct}) = 20.3 + 1.014 \times T_{\text{eff}}(\text{H}\alpha)$$

The correlation coefficient between the two sets is 0.9976, a very tight connection (Fig. 3). The principal aim of our paper has been met, a simple procedure for deriving the true effective temperature from the observed H α Balmer line profiles, enabling to bypass the uncertainties in the amount of interstellar reddening, critical for temperatures derived from photometric indices. All the calibration stars are all at distances less than 15 parsecs, therefore not affected by reddening. The remaining interesting problem is to understand why the two sets of temperatures have an offset instead of being equal. This is clearly a problem for 3D hydrodynamical models, that we are investigating now.

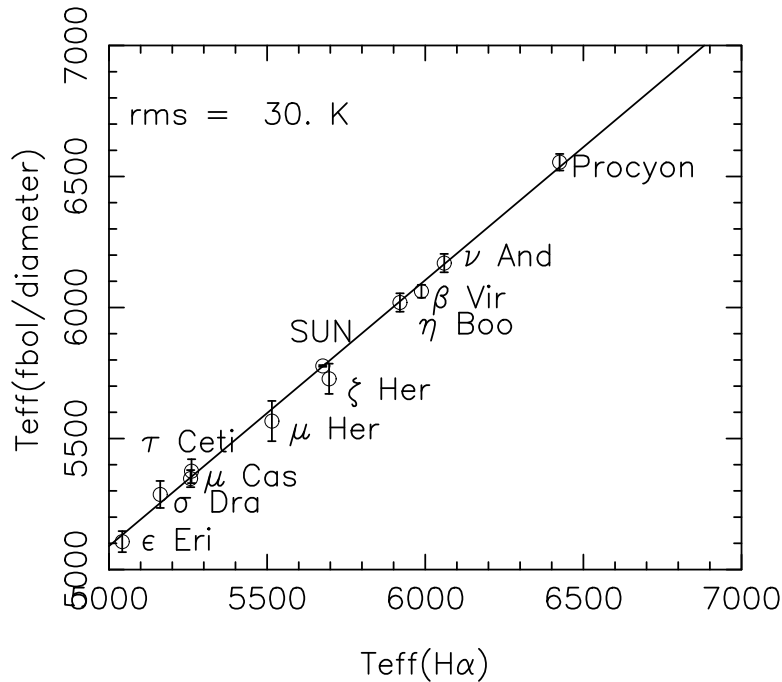


Fig. 3. Regression line between $T_{\text{eff}}(\text{H}\alpha)$ and $T_{\text{eff}}(\text{direct})$. The rms of the fit is 30 K.

The details of this research are available in Cayrel et al. (2011).

References

- Allard, N.F., Kielkopf, J.F., Cayrel, R., van 't Veer-Menneret, C. 2008, A&A 480, 581
 Allende Prieto, C., Barklem, P.S., Lambert, D.L., Cunha, K. 2004, A&A 420, 183 (S4N)
 Barklem, P.S., Stempels, H.C., Allende Prieto, C. et al. 2002 A&A 385,951
 Casagrande, L., Ramírez I., Meléndez, J. et al. 2010, A&A 512, 54
 Cayrel, R., van 't Veer-Menneret, C., Allard, N.F., Stehlé C. 2011, A&A 531, A83
 Soubiran, C., Le Campion, J.-F., Cayrel de Strobel, G., Caillo, A. 2010, A&A 515, A111
 Stehlé C., & Hutcheon, R. 1999, A&AS, 140, 93

CALIBRATION OF THE GAIA RVS FROM GROUND-BASED OBSERVATIONS OF CANDIDATE STANDARD STARS

L. Chemin¹, C. Soubiran¹, F. Crifo², G. Jasniewicz³, D. Katz², D. Hestroffer⁴ and S. Udry⁵

Abstract. The Radial Velocity Spectrometer (RVS) on board of Gaia will perform a large spectroscopic survey to determine the radial velocities of some 1.5×10^8 stars. We present the status of ground-based observations of a sample of 1420 candidate standard stars designed to calibrate the RVS. Each candidate star has to be observed several times before Gaia launch (and at least once during the mission) to ensure that its radial velocity remains stable during the whole mission. Observations are performed with the high-resolution spectrographs SOPHIE, NARVAL and CORALIE, completed with archival data of the ELODIE and HARPS instruments. The analysis shows that about 7% of the current catalogue exhibits variations larger than the adopted threshold of 300 m s^{-1} . Consequently, those stars should be rejected as reference targets, due to the expected accuracy of the Gaia RVS. Emphasis is also put here on our observations of bright asteroids to calibrate the ground-based velocities by a direct comparison with celestial mechanics. It is shown that the radial velocity zero points of SOPHIE, NARVAL and CORALIE are consistent with each other, within the uncertainties. Despite some scatter, their temporal variations remain small with respect to our adopted stability criterion.

Keywords: Galaxy: kinematics and dynamics, Galaxy: structure, Stars: kinematics and dynamics, Minor planets, asteroids: general, Surveys, Techniques: radial velocities

1 Generalities

The RVS is a slitless spectrograph whose spectral domain is 847-874 nm and resolving power $R \sim 11500$. The expected accuracy is 1 km s^{-1} for F0 to K0 stars brighter than $V=13$, and for K1 to K4 stars brighter than $V=14$.

The main scientific objectives of RVS are the chemistry and dynamics of the Milky Way, the detection and characterisation of multiple systems and variable stars (for more details, see Wilkinson et al. 2005). Those objectives will be achieved from a spectroscopic survey of:

- Radial velocities ($\sim 150 \times 10^6$ objects, $V \leq 17$)
- Rotational velocities ($\sim 5 \times 10^6$ objects, $V \leq 13$)
- Atmospheric parameters ($\sim 5 \times 10^6$ objects, $V \leq 13$)
- Abundances ($\sim 2 \times 10^6$ objects, $V \leq 12$)

Each star will be observed ~ 40 times on average by RVS over the 5 years of the mission.

¹ Laboratoire d'Astrophysique de Bordeaux, UMR 5804 (CNRS, Université Bordeaux 1), 33271 Floirac Cedex, France

² Observatoire de Paris, GEPI, UMR 8111 (CNRS, Université Denis Diderot Paris 7), 92195 Meudon, France

³ GRAAL, UMR5024, (CNRS, Université Montpellier 2), 34095 Montpellier Cedex 05, France

⁴ Observatoire de Paris, IMCCE, UMR8028 (CNRS, Université Pierre & Marie Curie Paris 6), 75014, Paris, France

⁵ Observatoire de Genève, 51 Ch. des Maillettes, 1290 Sauverny, Switzerland

2 Calibration of the Gaia RVS

Because the RVS has no calibration module on board, the zero point of its radial velocities has to be determined from reference sources. Ground-based observations of a large sample of well-known, stable reference stars as well as of asteroids are thus critical for the calibration of the RVS. A sample of 1420 candidate standard stars has been established (Crifo et al. 2009, 2010) and has to be validated by high spectral resolution observations.

Two measurements per candidate star are being made before Gaia is launched (or one, depending on already available archived data). Another measurement will occur during the mission. The measurements will allow us to check the temporal stability of radial velocities, and to reject any targets with significant RV variation.

3 Status of observations of stars

The ongoing observations are performed with three high spectral resolution spectrographs:

- SOPHIE on the 1.93-m telescope at Observatoire de Haute-Provence,
- NARVAL on the T elescope Bernard Lyot at Observatoire Pic-du-Midi,
- CORALIE on the Euler swiss telescope at La Silla.

As of June 2011 we have observed 995 distinct candidates with SOPHIE, CORALIE and NARVAL. The detailed observations per instrument are:

- 691 stars (1165 velocities) with SOPHIE
- 669 stars (945 velocities) with CORALIE
- 93 stars (98 velocities) with NARVAL

Figure 1 (left-hand panel) represents the spatial distribution in the equatorial frame of the sample and the number of measurements per object we have done so far with the three instruments.

In addition to those new observations, we use radial velocity measurements available from the spectroscopic archives of two other high-resolution instruments: ELODIE, which is a former OHP spectrograph, and HARPS which is currently observing at the ESO La Silla 3.6-m telescope. The archived data allow us to recover 1057 radial velocities for 292 stars (ELODIE) and 1289 velocities for 113 stars (HARPS).

Figure 1 (right-hand panel) summarizes the status of the total number of measurements for the sample of 1420 candidate stars performed with all five instruments.

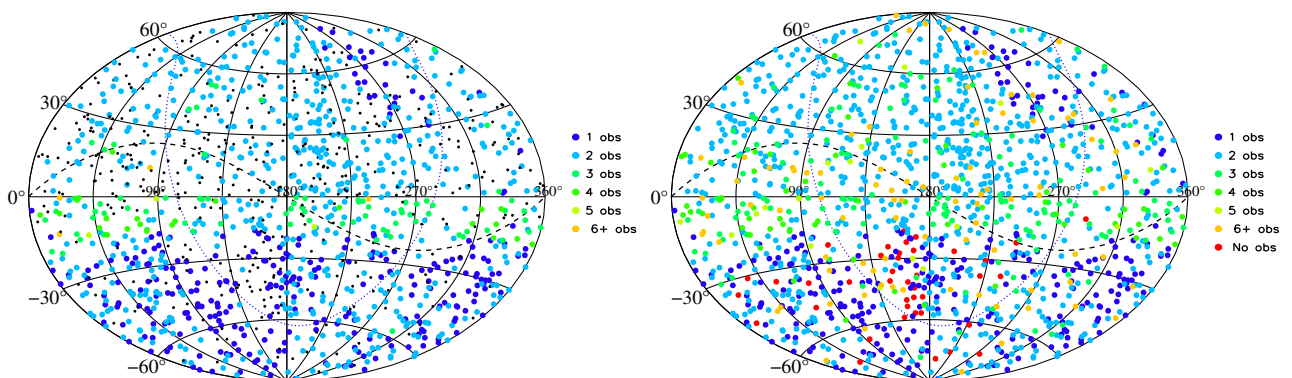


Fig. 1. Left panel: Current status of the number of observations available per candidate standard star observed with the SOPHIE, CORALIE and NARVAL instruments (995 distinct stars). Black dots indicate the locations of the 425 remaining sources from the sample of 1420 candidates. **Right panel:** Same as in left panel, but including archival data of the ELODIE and HARPS instruments as well. The maps are represented in the equatorial frame. The Ecliptic plane is shown as a dashed line and the Galactic plane as a dotted line.

4 How stable are the radial velocities of our candidates?

We have derived the variation of radial velocity of each star for which we have at least two velocity measurements separated by an elapsed time of at least 100 days. These stars represent a subsample of 1044 among 1420 targets. The variation is defined as the difference between the maximum and minimum velocities, as reported in the frame of the SOPHIE spectrograph. Its distribution is displayed in Figure 2.

A candidate is considered as a reference star for the RVS calibration when its radial velocity does not vary by more than an adopted threshold of 300 m s^{-1} . Such a threshold has been defined to satisfy the condition that the variation of the RV of a candidate must be well smaller than the expected RVS accuracy (1 km s^{-1} at best for the brightest stars). As a result, we find $\sim 7\%$ of the 1044 stars exhibiting a variation larger than 300 m s^{-1} , as derived from available measurements performed to date. Those variable stars will have to be rejected from the list of standard stars. Note that about 75% of the 1044 stars have very stable RV, at a level of variation smaller than 100 m s^{-1} .

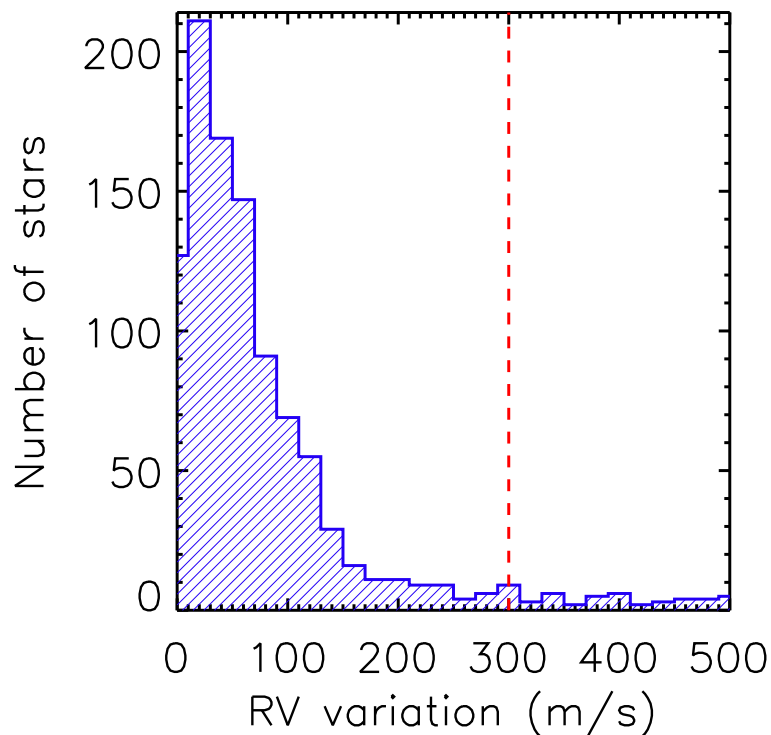


Fig. 2. Distribution of variations of radial velocities of candidate standard stars having at least two RV measurements separated by 100 days or more. A dashed line shows the adopted 300 m s^{-1} stability threshold.

5 Spectral observations of asteroids

Observations of asteroids are very important for the radial velocity calibration. Indeed they will be used to determine the zero-points of the RVs measured with SOPHIE, CORALIE and NARVAL (as well as the Gaia-RVS zero-point). Those goals will be achieved by comparing the spectroscopic RVs of asteroids from ground-based measurements with theoretical kinematical RVs from celestial mechanics. The theoretical RVs are provided by IMCCE and are known with an accuracy better than 1 m s^{-1} . About 280 measurements of 90 asteroids have been done so far.

As an illustration, Figure 3 (left-hand panel) displays the residual velocity (observed minus computed RVs) of asteroids observed by the SOPHIE instrument as a function of the observed RVs. The average residual of asteroids observed with SOPHIE is 30 m s^{-1} and the scatter is 38 m s^{-1} .

In Figure 3 (right-hand panel) we also show the variation of the residual RVs with time. It nicely shows how

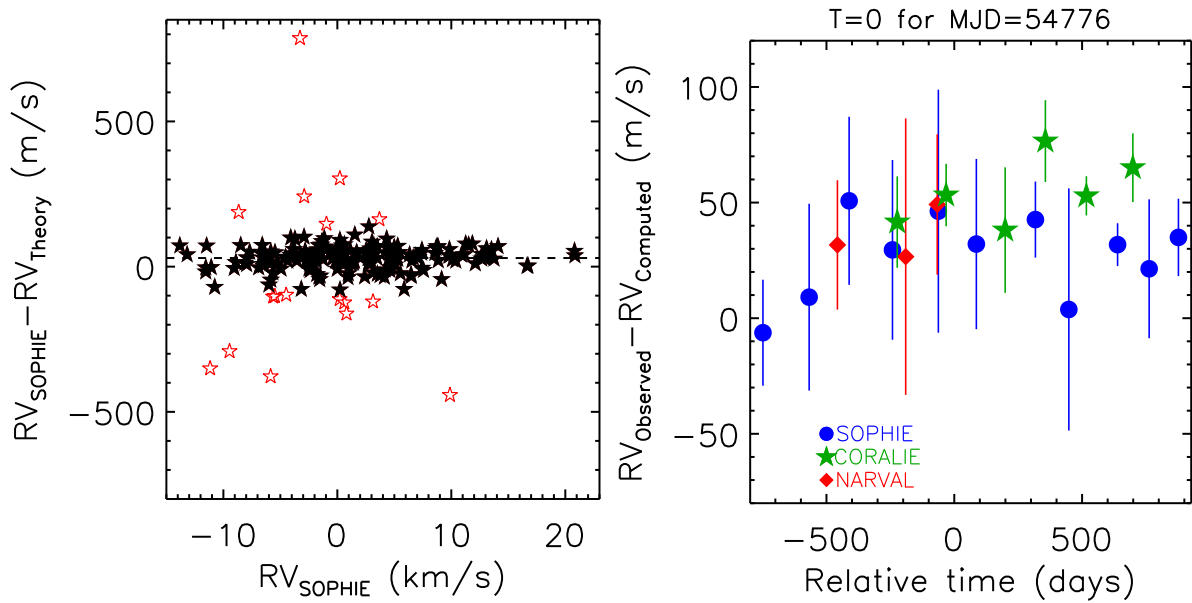


Fig. 3. Radial velocities of asteroids. **Left panel:** Residual velocities (observed minus computed) of asteroids as a function of their observed velocities (SOPHIE observations only). Red symbols are points deviant by more than 3σ . A horizontal dashed line represents the mean residual velocity of 30 m s^{-1} . **Right panel:** Comparison of residual velocities of asteroids for SOPHIE, CORALIE and NARVAL as a function of time for the various observing runs.

stable the RVs are as a function of time. The residual RVs are relatively constant within the quoted errors. The error-bars represent the dispersion of all measurements performed at each observational run. Their amplitude is mainly related to the conditions of observations that differ from one session to another (in particular the moonlight contamination). Though significant (between 10 and 50 m s^{-1}) those error-bars remain smaller than our target stability criterion of 300 m s^{-1} , which will enable us to determine correctly the RV zero point of each instrument.

Note also we have verified that intrinsic properties of asteroids (e.g. their size, shape, rotation velocity, albedo, etc...) have negligible systematic impacts on the determination of RVs zero points for the spectrographs. From now, observations of asteroids shall be performed with reduced moonlight contamination

We are very grateful to the AS-Gaia, the PNPS and PNCG for the financial support of the observing campaigns and the help in this project.

References

- Crifo F., Jasniewicz G., Soubiran C., et al., 2009, SF2A 2009 conference proceedings, 267
 Crifo F., Jasniewicz G., Soubiran C., et al., 2010, A&A, 524, A10
 Wilkinson M., et al., 2005, MNRAS, 359, 1306

DUST MASS IN SIMULATIONS OF GALAXIES

N. Gaudin¹ and H. Wozniak¹

Abstract. We have designed a model to compute dust abundances in chemodynamical N-body+SPH simulations. It includes the production by Asymptotic Giant Branch (AGB) stars, supernovae (SNe, type I and II), the destruction by shock induced by SNe and the growth of dust grains in the interstellar medium (ISM). The model takes advantage of the self-consistent chemodynamical code to compute the evolution of the dust mass: the two ISM phases, evolving stellar populations, and metal enrichment. We show that our model is able to reproduce the abundances of dust and its linear relation with the metallicity of the ISM, provided all dust processes are included. Moreover, some low-metallicity galaxies that are under-abundant in dust could be explained by our simulations as being dominated by the dust destruction in SNe shocks.

Keywords: dust, galaxies: evolution, methods: numerical

1 Introduction

Despite its low mass fraction the dust provides powerful clues for the chemical and physical description of the ISM (Savage & Sembach 1996; Jenkins 2009), and recently for constraining galactic evolution (Dwek et al. 2011).

To understand the life-cycle of dust in ISM, semi-analytic models of galactic evolution have been extensively used (Lisenfeld & Ferrara 1998; Tielens 1998; Hirashita et al. 2002; Morgan & Edmunds 2003; Zhukovska et al. 2008; Dwek & Cherchneff 2011). We present hereafter a model for dust production and destruction mechanisms, specially designed for self-consistent chemodynamical simulations of galaxies. The results obtained in simulation of a massive galaxy are discussed in section 3.

2 The Model

The evolution of a galaxy is simulated using PM+SPH code described in Michel-Dansac & Wozniak (2004). Wozniak et al. (2011) have updated the star formation recipes and the chemical evolution to take the stellar population evolution as well as the multiphase nature of the ISM into account. The new chemodynamical prescription includes star formation based on the local Jeans instability. Stellar populations have various metallicities and evolve over ~ 10 Gyr injecting energy and gas into ISM. The ISM has two gaseous phases. One represents the cold neutral medium with a fixed temperature (10^2 K). The second has a variable temperature ranging from 10^2 to 10^8 K, determined by solving the energy equilibrium. The cooling function is metallicity dependent. Heating from stars is also included. Phases exchange mass by condensation and evaporation mechanisms.

Our model (see Fig. 1, left) computes the dust mass with recipes adapted from semi-analytic models. The main difference is the local nature of our model. Indeed, contrary to the global galactic computation of semi-analytic models, our recipes computes dust mass for each SPH particles having a resolution varying from 10 pc (in the nucleus) to 1 kpc (in the outskirts). All assumptions of classical semi-analytic models of dust evolution have been adapted to the local conditions in simulations. A second difference comes from the physically motivated distinction of two ISM phases (the cold and the warm/hot). Our model takes advantage of this, providing dust mass separately for both phases.

We have performed simulations with different combinations of three basic processes: the production of dust by stars, the accretion in interstellar medium, and the destruction by SNe. The “stardust” is mainly produced by

¹ Observatoire Astronomique de Strasbourg, 11 rue de l’Université, 67000 Strasbourg, France

AGB stars and SNe (Cherchneff & Dwek 2010; Morgan & Edmunds 2003), we make use of data from Zhukovska et al. (2008) with metallicity dependent populations of stars, injecting dust in the two phases of our ISM as proportional to their respective volume. The production by growth of grains in ISM must be included to balance the low lifetime of dust (Draine et al. 2007). In our simulations, it is activated in cold phase above a threshold density of $n_{\text{H}} = 10^4 \text{ cm}^{-3}$. Our accretion recipe uses a simple assumption based on the collision rate between grains and particles of the gaseous phase, leading to:

$$\rho_d(t) = \frac{\rho_d(0)}{(1 - \rho_d(0)/\rho_M) e^{-t/\tau} + \rho_d(0)/\rho_M}, \quad (2.1)$$

where ρ_d is the local density of the dust component, ρ_M its maximal density which is the density of the accreting metal C, O, Mg, Si, Fe (Savage & Sembach 1996; Draine et al. 2007), and τ^{-1} the rate of accretion (proportional to the accreting metal density too). The destruction of dust occurs mainly in shocks produced by SNe. We use the destruction efficiency computed by Jones et al. (1994, 1996) and the shocked mass from Hirashita et al. (2002), to get a formula of destroyed mass of dust, proportional to the energy released by the SNe.

3 Discussion

We have performed four simulations with various combinations of active processes. The global evolution of simulations is plotted in Fig. 1 (right). Our simulations agree well with the observations from Lisenfeld & Ferrara (1998), Draine et al. (2007), and Engelbracht et al. (2008). The trend for the simulations, apart from the simulation with stardust and destruction only, is linear as predicted by the expected relation:

$$\frac{M_{\text{dust}}}{M_{\text{H}}} \approx 0.01 \frac{(O/H)}{(O/H)_{\text{MW}}}, \quad (3.1)$$

scaled from local Milky-Way models (see Draine et al. 2007). If destruction is activated and accretion is not, we obtain lower dust abundances conforming with the low-metallicity galaxies which are dust under-abundant.

We have shown that only the simulation which includes all the three creation and destruction mechanisms is able to reproduce the observed dust mass ratio as a function of metallicity (see Fig. 2). Especially, because of the lack of free parameters for destruction, we need to include accretion to obtain a reasonable mass of dust when the destruction process is activated. Moreover, it is noteworthy that the destruction has a visible effect in low metallicity region of our simulation with the full dust physics. This dust fraction, lower than that predicted by the linear relation, suggests that low-metallicity irregular dwarves could be dominated by the dust destruction. This will be checked by full self-consistent simulations of dwarf galaxies.

References

- Cherchneff, I. & Dwek, E. 2010, *ApJ*, 713, 1
 Draine, B. T., Dale, D. A., Bendo, G., et al. 2007, *ApJ*, 663, 866
 Dwek, E. & Cherchneff, I. 2011, *ApJ*, 727, 63
 Dwek, E., Staguhn, J. G., Arendt, R. G., et al. 2011, *ApJ*, 738, 36
 Engelbracht, C. W., Rieke, G. H., Gordon, K. D., et al. 2008, *ApJ*, 678, 804
 Hirashita, H., Tajiri, Y. Y., & Kamaya, H. 2002, *A&A*, 388, 439
 Jenkins, E. B. 2009, *ApJ*, 700, 1299
 Jones, A. P., Tielens, A. G. G. M., & Hollenbach, D. J. 1996, *ApJ*, 469, 740
 Jones, A. P., Tielens, A. G. G. M., Hollenbach, D. J., & McKee, C. F. 1994, *ApJ*, 433, 797
 Lisenfeld, U. & Ferrara, A. 1998, *ApJ*, 496, 145
 Michel-Dansac, L. & Wozniak, H. 2004, *A&A*, 421, 863
 Morgan, H. L. & Edmunds, M. G. 2003, *MNRAS*, 343, 427
 Savage, B. D. & Sembach, K. R. 1996, *ARA&A*, 34, 279
 Tielens, A. G. G. M. 1998, *ApJ*, 499, 267
 Wozniak, H., Champavert, N., & Feldner, H. 2011, in *EAS Publications Series*, Vol. 44, *EAS Publications Series*, ed. H. Wozniak & G. Hensler, 41–42
 Zhukovska, S., Gail, H.-P., & Trieloff, M. 2008, *A&A*, 479, 453

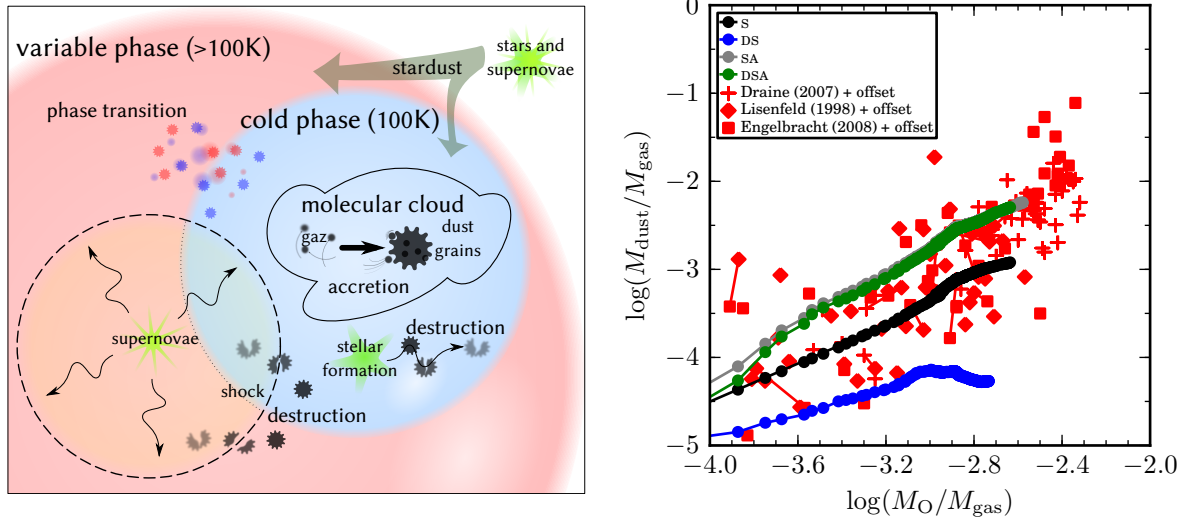


Fig. 1. **Left:** Sketch of physical processes involved to compute the evolution of the dust mass. **Right:** Evolution of our 4 simulations, snapshots every ~ 25 Myr. Simulations are labelled with the active processes: S for stardust, D for destruction, A for accretion. Data from observations (Lisenfeld & Ferrara 1998; Draine et al. 2007; Engelbracht et al. 2008), in red, have been homogenized applying an offset.

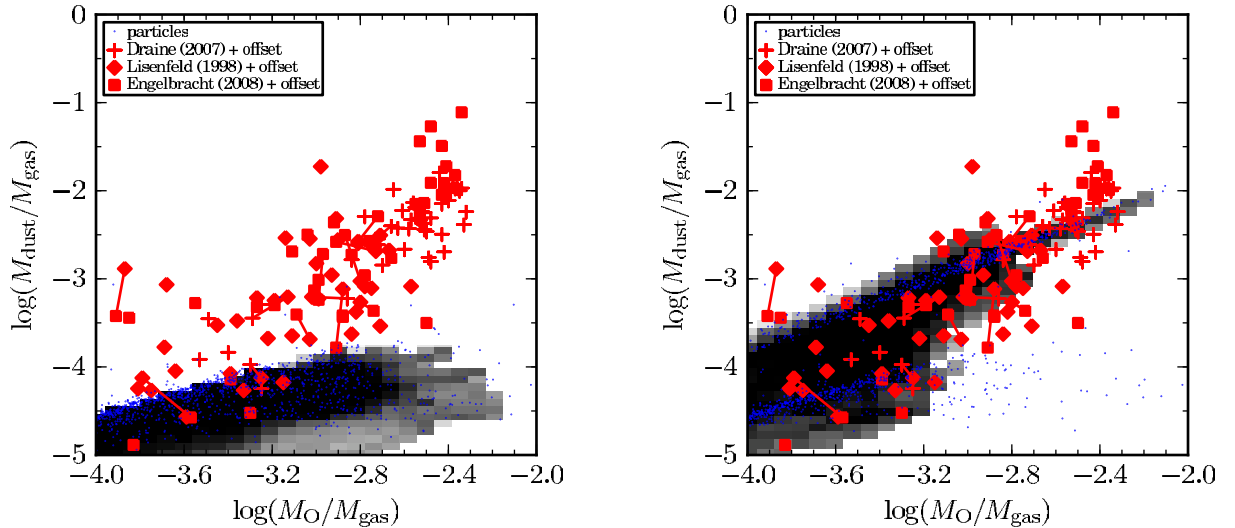


Fig. 2. 2D histograms of snapshots. **Left:** Simulation with stardust, SNe shock destruction, but without accretion. The observed dust abundance for high-metallicity galaxies is higher than the simulated value. All snapshots show similar behavior, we show here snapshot at $t = 264$ Myr. **Right:** Simulation with all the three dust processing active: destruction, stardust, and accretion. We take the snapshot at $t = 264$ Myr, few Myrs after the star formation rate maximum to have high dust destruction rate from SNe shocks.

DETERMINATION OF THE AGES OF STARS FROM THEIR POSITION IN THE HR DIAGRAM

C. Guédé¹, Y. Lebreton¹ and G. Dréan²

Abstract. The determination of stellar ages is fundamental to understand the formation and evolution of the Galaxy. We determine the age of stars by combining their position in the HR diagram with stellar evolutionary tracks or isochrones. The goal of this study is to prepare the tools that will be used to age-date stars after the Gaia mission.

Keywords: stars: fundamental parameters - methods: statistical - (stars:) Hertzsprung-Russell and C-M diagrams

1 Introduction

To understand the formation and evolution of the Galaxy it is necessary to determine the ages of its stars. There are several methods to determine the age of stars which are based on either the kinematics or expansion of stars, the lithium depletion, the gyrochronology, activity, asteroseismology or isochrones models. These methods are described by Soderblom 2010. Here we are interested in determining the ages of large samples of stars for which the method based on isochrones is applicable. The age of stars is determined by combining their position in the HR diagram and models isochrones (Ng & Bertelli 1998, Lachaume et al. 1999). We use a Bayesian estimation to determine the most probable age from stellar models (Pont & Eyer 2004, Jørgensen & Lindegren 2005 and Casagrande et al. 2011). We adapt this method to use the stellar evolutionary tracks instead of the isochrones. We compare our results to Casagrande et al. (2011) work to validate our tools. This method will be used to determine the ages of stars that will be observed by the Gaia mission.

In Section 2 we describe the Bayesian estimation and the methods that we use. In section 3 we compare the ages obtained with evolutionary tracks and with isochrones. Section 4 describes the age-mass relation and age-metallicity relation and the comparison of these relations with Casagrande et al. (2011) work.

2 Determination of ages

We determine the age of the stars from their position in the HR diagram and either stellar evolutionary tracks or isochrones. In the region of isochrones where the stars evolve very quickly (for example the turn-off) a star that we aim to date, can be adjusted by several isochrones. As an example in Fig 1 (Jørgensen & Lindegren 2005), for the star on the left there are three isochrones that adjust properly the star. Therefore, these stars have three possible ages. In this case, the question is how to choose the correct age? In order to answer this question we use a Bayesian approach: this method allows us to determine the most probable age with the *a priori* density function. The age of a star corresponds to the maximum of the *a posteriori* density function $f(T, [Fe/H], m)$, defined as

$$f(T, [Fe/H], m) \propto f_0(T, [Fe/H], m)L(T, [Fe/H], m) \quad (2.1)$$

where $f_0(T, [Fe/H], m)$ is the *a priori* density function, which depends on the Initial Mass Function, Stellar Formation Rate and initial metallicity distribution. We choose to adopt a flat stellar formation rate and a

¹ GEPI UMR 8111, Observatoire de Paris-Meudon , France

² LTSI, INSERM U642 Université de Rennes 1, France

flat initial metallicity distribution. For the initial mass function we use the same than Jørgensen & Lindegren (2005), which is defined as $\xi(m) = m^{-2.7}$ (it is based on the *IMF* of Kroupa et al. 1993). $L(T, [Fe/H], m)$ is the likelihood defined as

$$L(T, [Fe/H], m) = \left(\prod_{i=1}^n \frac{1}{(2\pi)^{\frac{1}{2}} \sigma_i} \right) \exp \left(\frac{-\chi^2}{2} \right) \quad (2.2)$$

where the χ^2 parameter is calculated for the temperature T_{eff} (or color) of the stars, the magnitude M_v (or luminosity) and the metallicity $[Fe/H]$. The σ_i are the corresponding observational errors. For the numerical implementation, we sum the *a posteriori* density function for the evolutionary track that have a metallicity measuring range between $[Fe/H]_{obs} \pm 3.5\sigma_{[Fe/H],obs}$ and for all masses. The age of the star corresponds to the maximum of the *a posteriori* density function.

The method of Jørgensen & Lindegren (2005) determines the age by using isochrones and we have adapted the program to determine the age directly from the evolutionary tracks. We compare both results in Section 3. This method is also well designed to calculate the mass of stars.

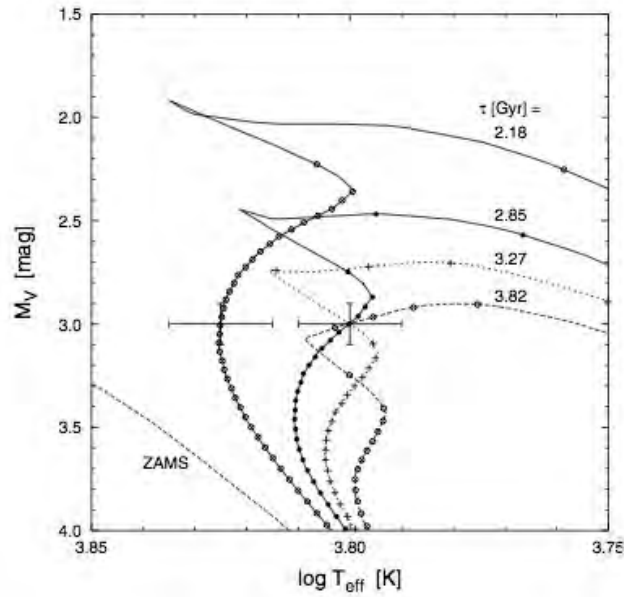


Fig. 1. Isochrones degeneracy in the HR diagram. After Jørgensen & Lindegren (2005)

3 Tracks vs. Isochrones

Traditionally, ages are derived from isochrones built by interpolation of stellar evolutionary tracks and provided by stellar modelers. To determine the ages we use the evolutionary tracks of Basti (Pietrinferni et al. 2004). We calculate the ages of 16 682 stars in the Geneva Copenhagen Survey of the solar neighborhood (Casagrande et al. 2011 but see also Holmberg et al. 2009). These stars are represented in a diagram $\log T_{eff} - M_v$ on the left Figure 2. We compare and classify the ages obtained with the isochrones and evolutionary tracks on the right Figure 2 and in the Table 1. We note that 72.2 % of the stars have similar ages : this shows that we have a good agreement between both methods. We note that the stars have different ages when they are located in the same region in the diagram $\log T_{eff} - M_v$, near the ZAMS. In the vicinity of the ZAMS, low mass stars evolve very slowly in the HR diagram so their age is poorly defined.

4 Age-mass relation and age-metallicity relation

We present the age-mass relation (on the left Figure 3) and the age-metallicity relation (on the right Figure 3) with ages and masses calculated by us with the evolutionary tracks method, for 6670 stars in the GCS catalogue. We obtain a relation that is similar to Casagrande et al. (2011). For the age-metallicity relation we

Table 1. Results of the comparison for the ages obtained with the isochrones and evolutionary tracks.

| | |
|--|--------|
| Similar ages | 72.2 % |
| Relative difference exceeding 30% | 7.5 % |
| Ages lower than 0.3 Gyr | 15.2 % |
| Stars with ages lower than 0.3 Gyr with both evolutionary tracks and isochrones | 47 % |
| Ages greater than 13.5 Gyr | 5.1 % |
| Stars with ages greater than 13.5 Gyr with both evolutionary tracks and isochrones | 68 % |

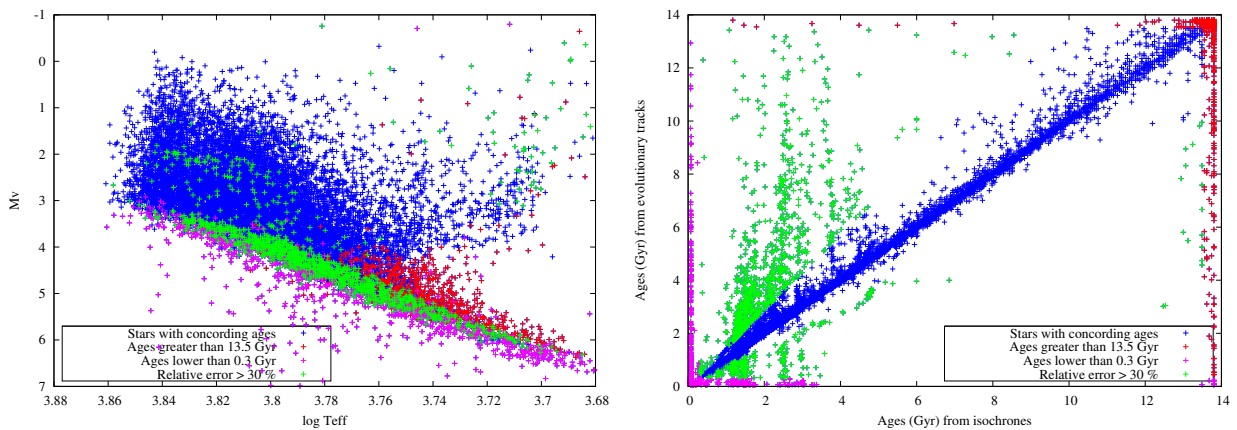


Fig. 2. Left Figure : HR diagram with (i) in red, stars with age > 13.5 Gyr, (ii) in pink stars with age < 0.3 Gyr, (iii) in green stars with ages differing by more than 30 % and (iv) in blue the stars having similar ages. Right Figure : comparison between ages from isochrones and ages from evolutionary tracks.

see a concentration of stars at solar metallicity and small ages: when the age increases there is a metallicity dispersion due to the radial mixing of the stars. The relation allows to demonstrate that a subsample of stars belongs to the thin disk (Haywood 2008).

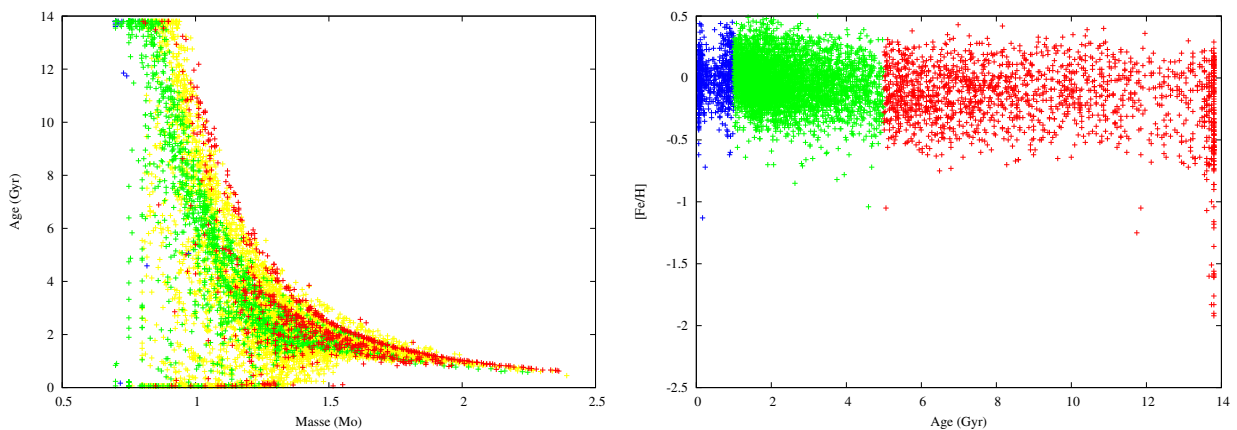


Fig. 3. Left Figure: Mass-Age relation for ages and masses from the evolutionary tracks. Colors indicate increasing metallicity $[Fe/H]$ from metal-poor stars (in blue) to metal-rich stars (in red). Right Figure : Age- $[Fe/H]$ relation for ages from evolutionary tracks. In blue stars with age < 1 Gyr, in green stars with $1 \text{ Gyr} \leq \text{age} < 5$ Gyr, and in red stars with age ≥ 5 Gyr.

5 Conclusions

We adapted the method of Jørgensen & Lindegren (2005) to determine the age of stars from evolutionary tracks. The comparison of the isochrones ages with the evolutionary tracks ages shows that the results of both methods are similar except for the stars close to the ZAMS. In these regions, the stars have a low mass and they evolve very slowly, so their age is arduous to determine. The comparisons of our results with those of Casagrande et al. (2011) shows that we obtain the same trend for the age-mass and age-metallicity relations. These comparisons allow us to validate our program for age determination.

We warmly thank Misha Haywood for his advice and for discussions.

References

References

- Casagrande, L., Schönrich, R., Asplund et al. S. 2011, *A&A*, 530, A138
Haywood, M. 2008, *MNRAS*, 388, 1175
Holmberg, J., Nordström, B., & Andersen, J. 2009, *A&A*, 501, 941
Jørgensen, B. R., & Lindegren, L. 2005, *A&A*, 436, 127
Kroupa, P., Tout, C. A., & Gilmore, G. 1993, *MNRAS*, 262, 545
Lachaume, R., Dominik, C., Lanz, T., & Habing, H. J. 1999, *A&A*, 348, 897
Ng, Y. K., & Bertelli, G. 1998, *A&A*, 329, 943
Pont, F., & Eyer, L. 2004, *MNRAS*, 351, 487
Pietrinferni, A., Cassisi, S., Salaris, M. et al. 2004, *ApJ*, 612, 168
Soderblom, D. R. 2010, *ARA&A*, 48, 581

NEW SB2 BINARIES FOR ACCURATE STELLAR MASSES WITH GAIA*

J.-L. Halbwachs¹, F. Arenou², B. Famaey¹, P. Guillout¹, Y. Lebreton² and D. Pourbaix³

Abstract. The forthcoming Gaia mission will make possible the derivation of accurate stellar masses of binary components, by combining the astrometric measurements and the elements of SB2 orbits. We present a list of 16 long period SB1 systems observed with the T193/Sophie, and for which we measured the radial velocity of the secondary component, changing them in SB2. The 32 components of these systems could get masses with errors around 1 % when the Gaia astrometric measurements and a sufficient set of RV measurements will be available.

Keywords: binaries: spectroscopic, stars: fundamental parameters

1 Introduction

The Gaia astrometric measurements will make possible the derivation of masses of double-lined spectroscopic binary (SB2) components, with relative errors around 1 % (Halbwachs & Arenou 1999, 2009). For that purpose, a large observation programme was undertaken at the OHP observatory with the T193/Sophie in order to get very accurate SB orbital elements. Two hundred and eight target stars were selected among known SB, taken in the SB9 catalogue (Pourbaix & Tokovinin 2003; Pourbaix et al. 2004) and also in Halbwachs et al. (2003) and Halbwachs et al. (2011), but only 52, ie 25 % of them, were already known as SB2. The priority of the first ongoing observing runs is then to detect the secondary components of the SB1, changing them in SB2.

2 The observations

In order to optimize the observing time, ephemerides were computed and the SB are observed only when the radial velocities (RV) of the components are sufficiently different to allow the detection of the secondary. Since many SB have periods as long as a few years, this selection criterion results in observing only a part of the sample, and in accumulating measurements for the stars which are in the best conditions, instead of observing the others. After one year and one additional mission, totalizing 8 nights, 265 radial velocity (RV) measurements were obtained for 123 stars, 29 SB2 and 94 single-lined spectroscopic binaries (SB1). The signal-to-noise ratios (SNR) of the spectra were adapted to the magnitudes of the stars, and were chosen between 50 and 150.

3 Detection of the secondary components

For each observation, the SOPHIE automatic pipe-line provides the cross-correlation function (CCF) of the spectrum of the SB with a mask. This mask usually corresponds to a spectral type close to that of the primary component, but masks adapted to the presumed secondary were also used. For a SB1, the CCF is a single bell-shape dip, that may be approximately fitted with a normal distribution. For a SB2, the dip corresponding to the secondary component is also visible when it is not too close to that of the primary, and the resulting CCF looks like the sum of two normal distributions.

Among the 94 SB1 observed, 16 had a CCF exhibiting a small secondary dip aside from the primary one. These CCF are shown in Fig. 1.

A few cases in Fig. 1 deserve explanations:

* Based on observations performed at the Haute-Provence Observatory

¹ Observatoire Astronomique de Strasbourg, UMR 7550, 11, rue de l'université, F-67000 Strasbourg, France

² GEPI, Observatoire de Paris-Meudon, F-92195 Meudon Cedex, France

³ FNRS, Université libre de Bruxelles, CP226, boulevard du Triomphe, 1050 Bruxelles, Belgium

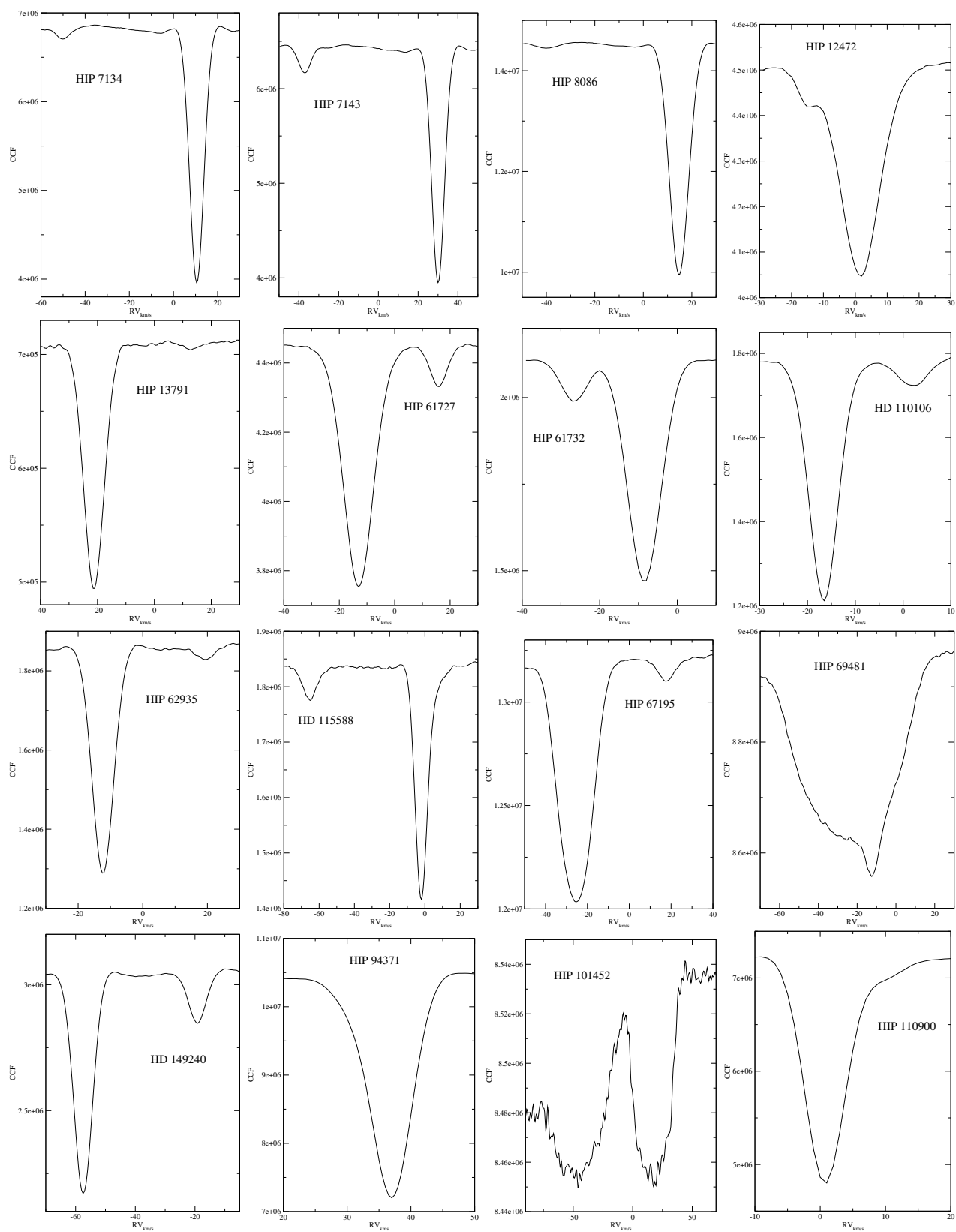


Fig. 1. The CCF of the new SB2. Small secondary dips are visible aside those of the primary components

Table 1. The mass ratios of the new SB2. Very uncertain estimations are indicated with a “:” in the place of the last digit.

| Star | $q = \mathcal{M}_2/\mathcal{M}_1$ | Star | $q = \mathcal{M}_2/\mathcal{M}_1$ |
|-----------|-----------------------------------|------------|-----------------------------------|
| HIP 7134 | 0.72 | HIP 62935 | 0.71 |
| HIP 7143 | 0.58 | HD 115588 | 0.36 |
| HIP 8086 | 0.5 : | HIP 67195 | 0.65 |
| HIP 12472 | 0.68 | HIP 69481 | 0.2 : |
| HIP 13791 | 0.53 | HD 149240 | 0.42 |
| HIP 61727 | 0.64 | HIP 94371 | 0.9 : |
| HIP 61732 | 0.66 | HIP 101452 | 0.92 |
| HD 110106 | 0.75 | HIP 110900 | 0.85 |

- HIP 8086: The secondary dip is very small, but it was observed at 3 different epochs, and its position is moving as expected. The detection is then certain.
- HIP 69481: A narrow secondary dip is emerging from a wide primary dip. A second observation, at another phase, confirms the detection.
- HIP 94371: Only one dissymmetric dip is visible, and the detection must still be confirmed.
- HIP 101452: An A0V-type star, at the very earliest limit of the range covered by SOPHIE. Since the earliest mask is F0, the CCF profile is not really the expected one, with a background much lower on the left side than on the right one.
- HIP 110900: The secondary dip is in the wing of the primary one, and it has to be confirmed.

4 Mass ratios of the new SB2

Since the barycentric velocities of the systems, V_γ , were already obtained with the elements of the SB1 orbits, the mass ratios may be obtained from one observation only. For that purpose, the velocities of the components were derived, fitting the CCF with two normal distributions subtracted to a linear background. The mass ratio is then $q = |V_1 - V_\gamma|/|V_2 - V_\gamma|$, where V_1 and V_2 are the RV of the primary and of the secondary component, respectively. The resulting q are in Table 1. It is worth noticing that these estimations are rather uncertain, since they are based on barycentric velocities obtained with another spectrograph than SOPHIE, and we still have too few measurements for correcting the systematic shift between our SOPHIE measurements and the ones used in the derivation of the SB orbit.

The mass ratios in Table 1 range from around 0.2 to 0.92, with a median around 0.65. We remind that, with spectrographs earlier than the CCD era, the luminosity ratio of binary star components generally prevents detection of secondaries with mass ratio smaller than 0.65 in the best conditions (Halbwachs et al. 2003). Therefore, half of the new SB2 detected with SOPHIE were obviously not detectable with the previous generation. Moreover, three new SB2 have a mass ratio well above this limit :

- HIP 101452. The primary is a A0p-type star, and its radial velocity, obtained in the past from photographic plates, was probably measured thanks to the peculiar lines of the spectrum. These lines could be missing in the secondary spectrum. The two components are clearly visible on the CCF obtained with an early-type mask.
- HIP 94371 and HIP 110900. If the secondary is confirmed in the future, it seems to be underluminous. It is obvious that the relation between the mass ratio and the visibility of the secondary is not unique: for instance, the secondary dip of HD 149240 ($q=0.42$) is much more visible than that of HIP 62935 ($q=0.71$).

5 Conclusions

Thanks to the ability of the SOPHIE spectrograph, the detection limit in mass ratio is shifted from around 0.7 to around 0.4. This leads to a selection of $52 + 16 = 68$ SB2, ie 136 stars for which we expect to derive the

masses with an accuracy near 1 % at the end of the Gaia mission. Since 62 SB1 remain to be measured, we still expect to find around 10 new SB2, leading to a total amount of a bit more than 150 individual masses. Since the combined astometric+spectroscopic solution will also provide the luminosity ratio of the components, the luminosities of the stars in the Gaia *G*-band will be obtained together with the masses. Therefore, the mass–luminosity relation will then be revisited thanks to our programme.

This programme is supported by the PNPS and by the AS-Gaia. We are grateful to the staff of the OHP for their kind assistance.

References

- Halbwachs, J.-L., Arenou, F. 1999, *Baltic Astronomy* 8, 301
- Halbwachs, J.-L., Arenou, F. 2009, *Proceedings SF2A 2009 – Scientific Highlights*, M. Heydary–Malayeri, C. Reylé et R. Samadi édr., p. 53
- Halbwachs, J.L., Mayor, M., Udry, S., Arenou, F. 2003, *A&A* 397, 159
- Halbwachs, J.L., Mayor, M., Udry, S. 2011, *MNRAS* (in preparation)
- Pourbaix, D., Tokovinin, A.A. 2003, The ninth catalogue of the orbital elements of spectroscopic binary stars, <http://sb9.astro.ulb.ac.be/>
- Pourbaix, D., Tokovinin, A.A., Batten, A.H. et al. 2004, *A&A* 424, 727

CHEMICAL ABUNDANCES OF A-TYPE DWARFS IN THE YOUNG OPEN CLUSTER M6

T. Kılıçoğlu¹, R. Monier² and L. Fossati³

Abstract. Elemental abundance analysis of five members in the open cluster M6 (age ~ 90 myr) were performed using FLAMES-GIRAFFE spectrograph mounted on 8-meter class VLT telescopes. The abundances of 14 chemical elements were derived. Johnson and Geneva photometric systems, hydrogen line profile fittings, and ionization equilibrium were used to derive the atmospheric parameters of the stars. Synthetic spectra were compared to the observed spectra to derive chemical abundances. The abundance analysis of these five members shows that these stars have an enhancement (or solar composition) of metals in general, with some exceptions. C, O, Ca, Sc, Ni, Y, and Ba exhibit the largest star-to-star abundance variations.

Keywords: stars: abundances - stars: chemically peculiar - open clusters and associations: individual: M6

1 Introduction

Stars members of an open cluster are generally assumed to share common properties: same initial chemical composition, same age and same distance. Thus open clusters appear to be unique laboratories to constrain evolutionary models via abundance determinations. Especially, early type main sequence members of open clusters of different ages are excellent laboratories to study the competition between radiative diffusion and mixing mechanisms. Abundance analysis of the open clusters (or moving groups) Ursa Major, Pleiades, Coma Berenices, Praesepe, Hyades, NGC 5460 were performed by Monier (2005), Gebran & Monier (2008), Gebran et al. (2008), Gebran et al. (2010), Fossati et al. (2011).

M6 (=NGC 6405) is an open cluster located about 450-500 pc (e.g. Talbert 1965; Vleeming 1974; Paunzen et al. 2006) away in the constellation Scorpio. The first photometric study of M6, including numbering system of the cluster, was performed by Rohlfs et al. (1959). Various ages between 50 and 140 myr were derived by several authors for M6 (e.g. Vleeming 1974; North & Cramer 1981; Paunzen et al. 2006; Landstreet et al. 2007). We averaged these ages and adopted 90 ± 30 myr. M6 is a rich, young, and relatively close cluster. Thus, its brightness allows us to obtain good quality spectra of many members.

2 Observations

The 104 possible member stars have been observed using FLAMES-GIRAFFE spectrograph with MEDUSA fibers, mounted at UT2 (Kueyen), the 8 meter class VLT telescope in May and June, 2007 (Fossati et al. 2008). The spectral regions cover three wavelength intervals: 4500-5100 Å, 5140-5350 Å, and 5590-5840 Å at resolving powers of about 7500, 25900, 24200, respectively. Some of the spectra have very low signal-to-noise ratio which prevent us from performing a detailed abundance analysis. Only 42 members have Geneva seven-color photometric measurements that can be used to derive fundamental parameters. The cluster members are identified according to Rohlfs et al. (1959) classification.

¹ Ankara University, Faculty of Science, Department of Astronomy and Space Sciences, 06100, Tandoğan, Ankara, Turkey

² Laboratoire Hippolyte Fizeau, Université de Nice - Sophia Antipolis, 06108 Nice Cedex 2, France

³ Department of Physics and Astronomy, Open University, Walton Hall, Milton Keynes MK7 6AA, UK.

3 Effective Temperatures and Surface Gravities

3.1 Johnson UBV and Geneva Seven-Colour photometric systems

We mainly used Geneva seven-colour photometry to derive atmospheric parameters. Johnson UBV observations were used to estimate effective temperature only for the stars lacking Geneva photometry. The photometric data was retrieved from the WEBDA database. We adopted the colour excesses of $E(B-V) = 0.15 \pm 0.01$ and $E(B2-V1) = 0.13 \pm 0.01$ for Johnson UBV and Geneva seven-colour photometric systems, respectively (e.g. Vleeming 1974; Nicolet 1981; Ahumada & Lapasset 1995). The calibrations of Kunzli et al. (1997), and Popper (1980) were used during the calculations for Geneva and Johnson systems, respectively.

3.2 Balmer Lines

The Balmer lines of hydrogen are reliable diagnostics for atmospheric parameters. The Balmer profiles are sensitive to both effective temperature and surface gravity variations. At higher temperatures, hydrogen lines are more sensitive to surface gravity variations.

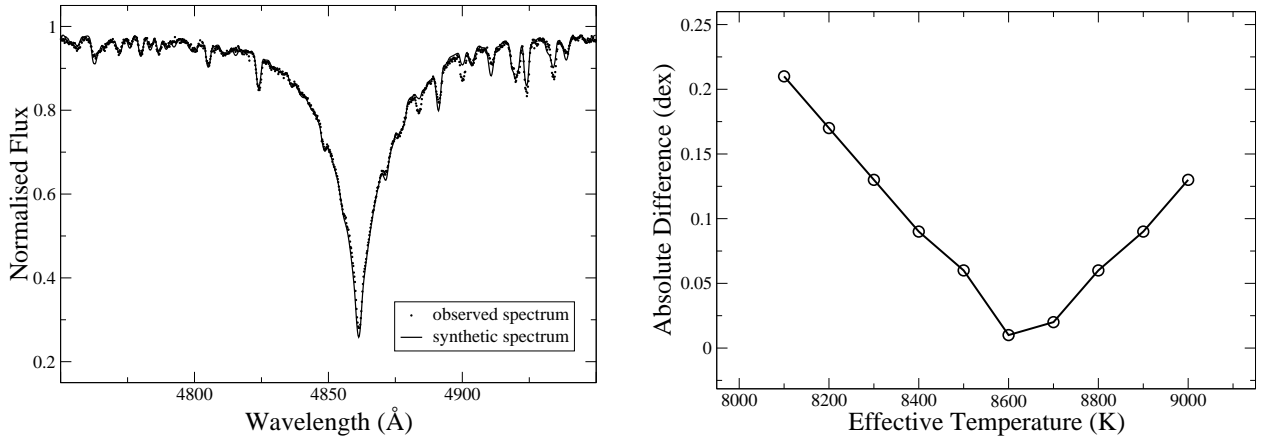


Fig. 1. Left: Comparison of the observed spectrum of NGC 6405 53 and the synthetic spectrum computed for $T_{\text{eff}} = 8100$ K, $\log g = 3.65$, and solar abundances. **Right:** Effective temperature versus absolute difference between the iron abundances (with respect to the Sun) derived by using Fe I and Fe II lines for NGC 6405 53.

In order to derive atmospheric parameters, we compared synthetic H_{β} profiles computed by SYNSPEC48 (Hubeny & Lanz 1992) to the observed H_{β} lines (Fig. 1, left). The H_{β} profiles of the analyzed early type stars appear to be narrower than those computed for the atmospheric parameters derived from the Geneva seven-colour photometry. This suggests that the actual surface gravities of these stars should be lower than those derived from Geneva photometry.

3.3 Ionisation Equilibrium

The hydrogen Balmer lines do not suffice to derive effective temperature and surface gravity simultaneously. In order to obtain these parameters precisely, we used ionization equilibrium of iron lines. We plotted the variation of the absolute value of $[\text{Fe}/\text{H}]_{\text{from Fe I lines}} - [\text{Fe}/\text{H}]_{\text{from Fe II lines}}$ as a function of effective temperature (Fig. 1, right).

As can be seen from Fig. 1, right for NGC 6405 53, the minimum of the curve shows that the effective temperature is close to 8650 K. This temperature is higher than the temperature derived from Balmer H_{β} lines (8100 K), while it is closer to the photometric temperature of 8380 K. The error of T_{eff} can be adopted as 150 K from Fig. 1, right.

4 Microturbulent Velocity

Microturbulent velocities should be derived as precisely as possible to derive reliable chemical abundances. In order to obtain this parameter, we used two methods. We first estimated the microturbulent velocity using

Pace et al. (2006)'s following calibration:

$$V_{\text{mic}} = -4.7 \log(T_{\text{eff}}) + 20.9 \text{ km s}^{-1}$$

Then, we plotted the standard deviations of the iron abundance calculated from many iron lines, according to various microturbulent velocity around that estimated value (Fig. 2, left). The minima in these plots yield the most likely microturbulent velocity. The shapes of the minima also indicate the accuracy of the microturbulent velocity. A sharp minimum provides a more precise value. The microturbulent velocities calculated by using this spectral method are consistent with those calculated from the calibration of Pace et al. (2006) in many cases.

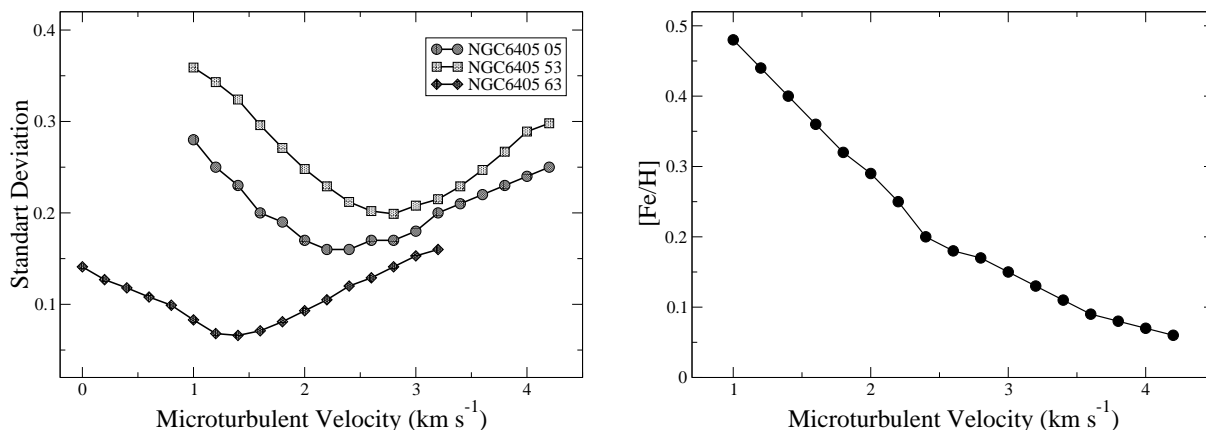


Fig. 2. Left: The standard deviation of the iron abundance derived from Fe I and Fe II lines versus microturbulent velocity for the three stars of the cluster. The standard deviations given for NGC 6405 53 were shifted by +0.05 for display purpose only. **Right:** Effective temperature versus absolute difference between the iron abundances (with respect to the Sun) derived by using Fe I and Fe II lines for NGC 6405 53.

In order to test the effects of microturbulence on the derived abundances, we performed the abundance analysis of unblended iron lines for assumed v_{mic} varying around the estimated value, in steps of 0.2 km s^{-1} for NGC 6405 05 (Fig. 2, right). A change of 0.2 km s^{-1} in microturbulence corresponds to an abundance change between 0.02-0.05 dex for this star.

5 Abundance Analysis

In order to perform the abundance analysis, we used model atmospheres and synthetic spectra. Model atmospheres were calculated by using ATLAS9 (Kurucz 1979), assuming a plane parallel geometry, a gas in hydrostatic and radiative equilibrium and LTE. During the computations, we used prescriptions of Smalley (2004) for the mixing length ratio. The atomic data was firstly constructed from Kurucz's gfhyperall.dat*, and then updated by using VALD, NIST databases and recent publications. Hyperfine structure was taken into account. Synthetic spectra are computed by using SYNSPEC48, assuming Grevesse & Sauval (1998) solar chemical composition.

6 Results and Discussion

Temperatures of 9100, 9400, 8650, 9400, 9900 K were adopted for the stars numbered 05, 47, 53, 71, and 95. Log g values are close to the value of 4.1, except no. 53 having lower value (3.65). We derived the abundances of 14 elements for the five members of M6 (Fig. 3). C, O and Ca abundances are close to solar or often slightly underabundant. All stars exhibit Sc deficiency, while Mg, Cr and Ni appear to be overabundant for the stars nos. 05, 47 and 53. Fe abundances are slightly scattered around the solar iron abundance. The largest star-to-star variations occur for the elements of C, O, Ca, Sc, Ni, Y and Ba.

*<http://kurucz.harvard.edu/LINELISTS.html>.

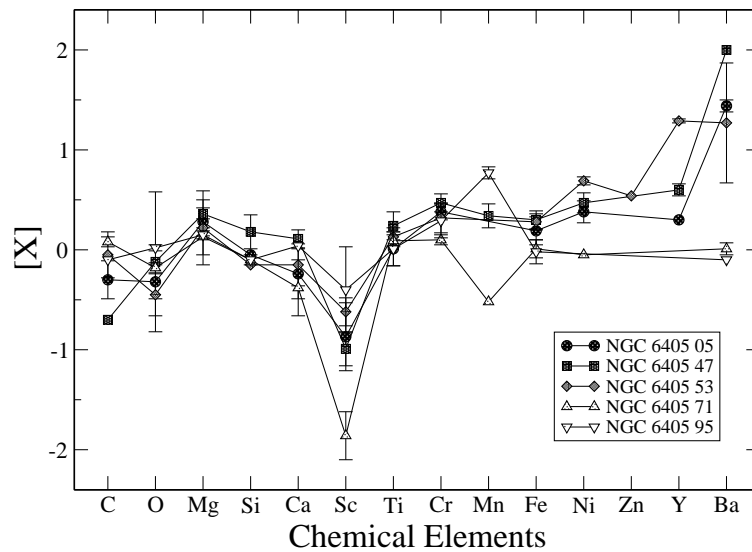


Fig. 3. The derived abundances of the elements with respect to the Sun for the five members of the cluster.

The abundances of the elements heavier than Mg are larger than solar for NGC 6405 47, except for Sc. The elements of Cr, Ni, Y and Ba are overabundant for this star. The abundance pattern for this star resembles that of a hot Am star.

The ongoing analysis of the remaining members will enable us to derive the general abundance pattern of the M6 cluster and address the chemical heterogeneity (star to star variations) of A stars in this open young cluster.

We kindly thank Pierre North for making his code CALIB available. This research was supported by the Scientific and Technological Research Council of Turkey (TÜBİTAK), and has used SIMBAD, WEBDA, VALD, and NIST databases.

References

- Ahumada, J. & Lapasset, E. 1995, *A&AS*, 109, 375
 Fossati, L., Bagnulo, S., Landstreet, J., et al. 2008, *A&A*, 483, 891
 Fossati, L., Folsom, C. P., Bagnulo, S., et al. 2011, *MNRAS*, 413, 1132
 Gebran, M. & Monier, R. 2008, *A&A*, 483, 567
 Gebran, M., Monier, R., & Richard, O. 2008, *A&A*, 479, 189
 Gebran, M., Vick, M., Monier, R., & Fossati, L. 2010, *A&A*, 523, A71+
 Grevesse, N. & Sauval, A. J. 1998, *Space Sci. Rev.*, 85, 161
 Hubeny, I. & Lanz, T. 1992, *A&A*, 262, 501
 Kunzli, M., North, P., Kurucz, R. L., & Nicolet, B. 1997, *A&AS*, 122, 51
 Kurucz, R. L. 1979, *ApJS*, 40, 1
 Landstreet, J. D., Bagnulo, S., Andretta, V., et al. 2007, *A&A*, 470, 685
 Monier, R. 2005, *A&A*, 442, 563
 Nicolet, B. 1981, *A&A*, 104, 185
 North, P. & Cramer, N. 1981, in *Liege International Astrophysical Colloquia*, Vol. 23, Liege International Astrophysical Colloquia, 55–59
 Pace, G., Recio-Blanco, A., Piotto, G., & Momany, Y. 2006, *A&A*, 452, 493
 Paunzen, E., Netopil, M., Iliev, I. K., et al. 2006, *A&A*, 454, 171
 Popper, D. M. 1980, *ARA&A*, 18, 115
 Rohlfs, K., Schrick, K. W., & Stock, J. 1959, *ZAp*, 47, 15
 Smalley, B. 2004, in *IAU Symposium*, Vol. 224, *The A-Star Puzzle*, ed. J. Zverko, J. Ziznovsky, S. J. Adelman, & W. W. Weiss, 131–138
 Talbert, F. D. 1965, *PASP*, 77, 19
 Vleeming, G. 1974, *A&AS*, 16, 331

CARBON-ENHANCED METAL-POOR STARS: WITNESSES OF THE FIRST GENERATION OF STARS

T. Masseron¹

Abstract. Carbon-enhanced metal-poor (CEMP) stars are now accepted to be mass-transferred binary member of the first generation of stars. Indeed, the peculiar chemical fingerprints revealed by their spectra represent a unique opportunity to study their now extinct progenitor (basically all low-metallicity stars with $M > 0.8M_{\odot}$).

Keywords: Carbon stars, metal-poor, abundances

1 The method

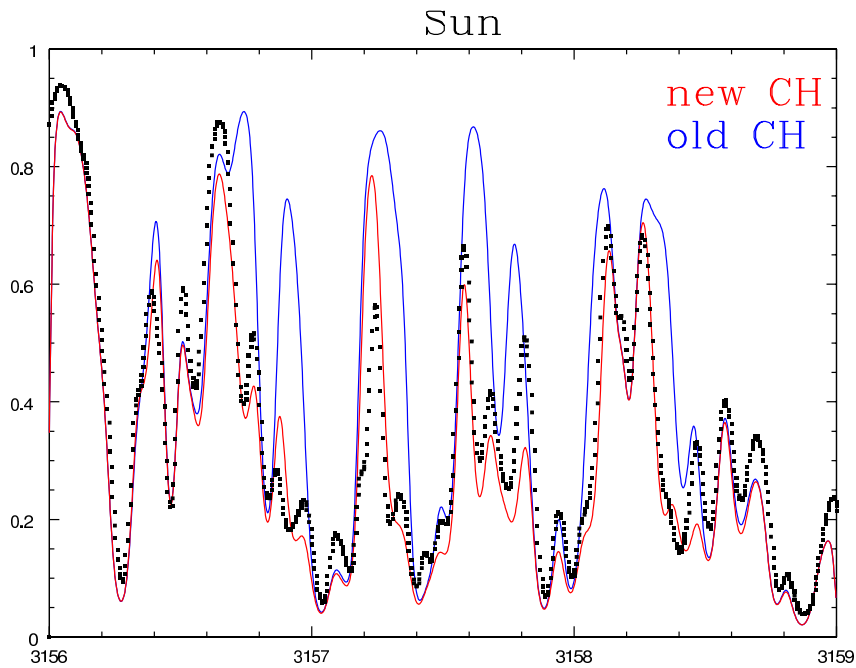


Fig. 1. : Example of synthesis of the Sun spectrum (black squares). The different colored lines show the improvement we made on molecular linelist.

In order to decipher the physics of these first generations of stars, we derive abundances from high resolution and high SNR spectra of a large sample of CEMP stars. For this, we use the radiative transfer code Turbospectrum, and specific stellar atmospheres (MARCS), taking into account the effect of large C enhancement on the atmosphere structure..

¹ Université Libre de Bruxelles, Belgium

One of the critical ingredients of abundance analysis are the input linelists. By using a combination of programs to simulate molecular structure and well selected laboratory measurements, we build new accurate molecular linelists. We show in Fig.1 the results for a part of the C-X band of the CH molecule.

Reciprocally, we also use stellar spectra probing thermodynamical conditions not available on earth to improve molecular constants (notably high rotational levels including predissociation levels).

2 The metal-poor stars zoo

Among metal-poor stars in the Galaxy, $\sim 20\%$ show a high content of carbon, the so-called Carbon-Enriched Metal-Poor (CEMP) stars. It is now clear that most of them have transferred material from an Asymptotic Giant Branch (AGB) star. In particular, AGB stars are known to produced s-process elements (like Ba or Pb).

However, we show in Fig. 2 that many subclasses exists: we do find a subclass of CEMP stars which nicely falls along the s-process predictions, but there are also CEMP stars which show no capture elements enhancement. We observed that these stars tends to have a lower metallicity than other CEMP stars, pointing out that nucleosynthesis of AGB stars may drastically change at very-low metallicity.

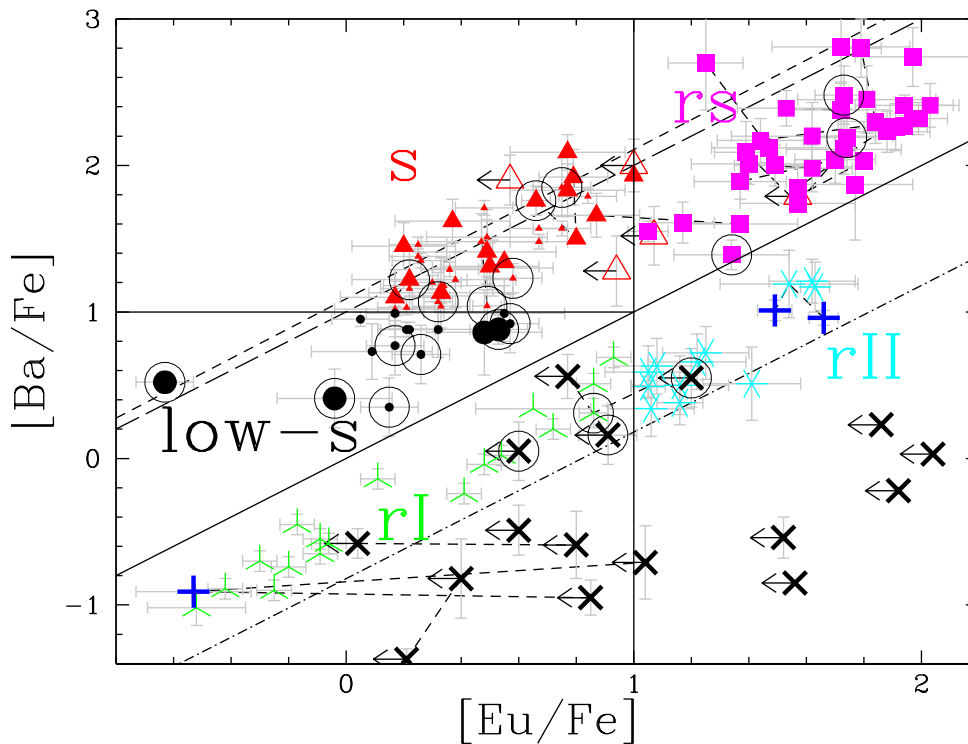


Fig. 2. : Ba vs Eu abundances in metal-poor stars. Lines represent the prediction for pure s-process nucleosynthesis (AGBs) (short and long dashed lines), and pure r-process nucleosynthesis (SNII) (dashed-dotted line). Except black dots, all symbols represent different categories of CEMP stars, according to their content of neutron-capture

In contrast, another subgroup of CEMP stars show a large excess of neutron-capture elements. We claim that another source of neutron is required in order to explain the existence of such stars (possibly the $^{22}\text{Ne}(\alpha, n)^{25}\text{Mg}$).

3 Fluorine

Fluorine is an element very sensitive of the thermodynamical conditions in AGB stars. While C is produced by He burning during the pulses of AGB stars, F is also produced in the He-rich layers of AGB stars, but is dependent on the presence of neutrons in the He intershell. Since the mechanism for making neutrons is still poorly understood, F is a very precious element to constrain the models.

Thanks to the IR high resolution spectrograph CRIRES, we were able to observe the HF lines in sample of CEMP stars (Fig.3). According to the observation of s-process elements, low-metallicity AGB models predict

that the progenitor of CEMP stars should have a mass between $1.2M_{\odot}$ and $2M_{\odot}$. Although we measure mostly upper limits, we did not observe as much Fluorine as expected by the models.

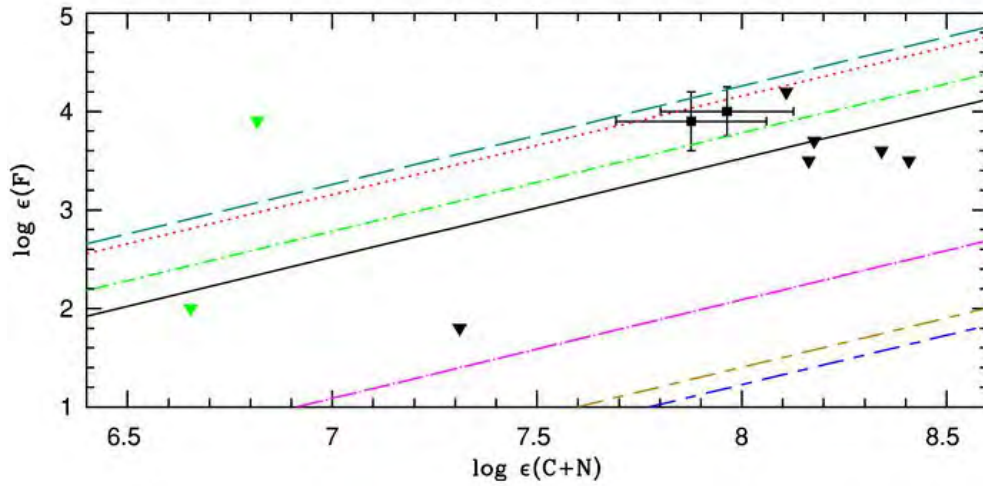


Fig. 3. : black triangles are CEMP stars. Models are from Karakas & Lattanzio (2007) for different masses; solid black line $1.25M_{\odot}$, red dotted line $1.75M_{\odot}$, teal dashed line $2.25M_{\odot}$, green dot-dashed line $2.5M_{\odot}$, magenta dot-dashed line $3.0M_{\odot}$, short-long dashed yellow line $3.5M_{\odot}$, and short-long dashed blue line $4M_{\odot}$.

4 Lithium

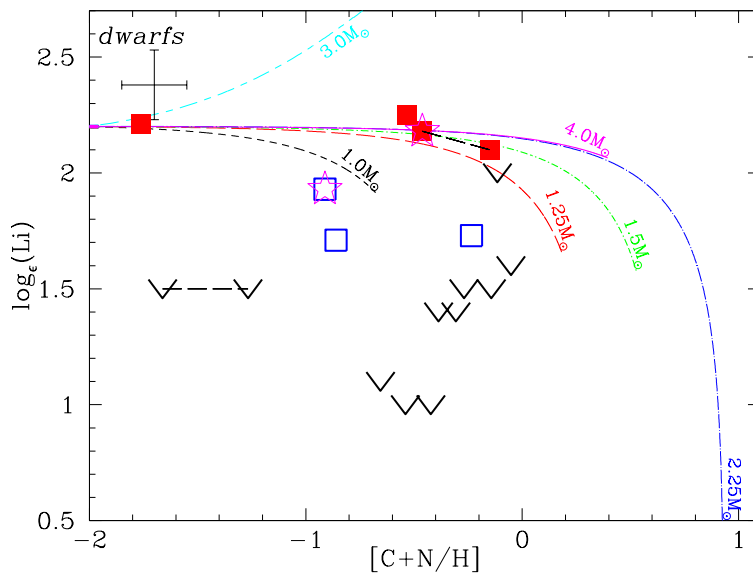


Fig. 4. red squares are CEMP Li-rich stars, blue open squares are Li-poor CEMP stars, black v signs are upper limits. Models are from Karakas & Lattanzio (2010).

While C is produced by AGB stars, Li is generally destroyed. Because CEMP stars have accreted large amount of this AGB material, it was not expected to find CEMP stars with high Li content (close to the Spite plateau). Since then, Li production in AGB stars has been required. However, we demonstrate in Fig.5 that Li-rich stars can naturally be explained by dilution of the AGB yields. In contrast it is more difficult to understand how some CEMP stars can have so low Li content. By looking at the rotation speed of the star, we

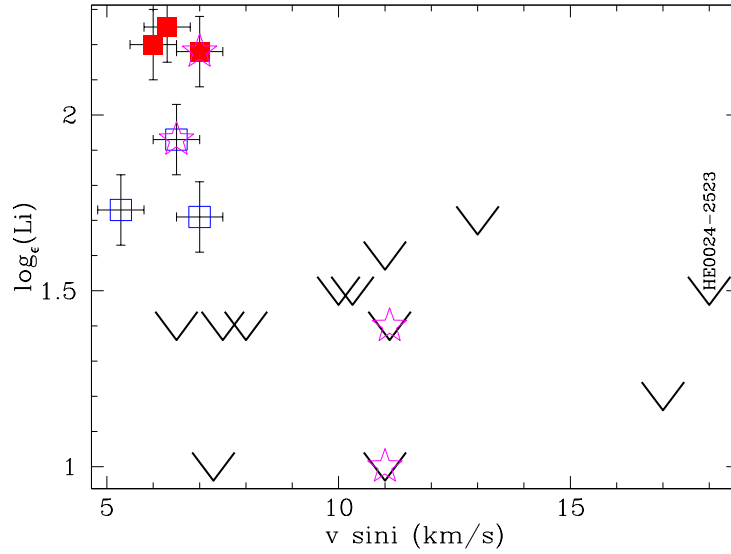


Fig. 5. Li abundance as function of rotational velocity. Red squares are CEMP Li-rich stars, blue open squares are Li-poor CEMP stars, black $v \sin i$ signs are upper limits.

noticed that no fast rotating stars were observed with a high Li content, suggesting that rotation has played a role in the Li destruction.

5 Conclusions

AGB stars at low metallicity show a broad range of nucleosynthetic properties that still need to be understood by the models: it seems that various s-processes occur, but the origin of the neutron source is still not clearly established. Moreover, various mixing mechanisms are expected to occur (thermohaline mixing, canonical extra mixing, hydrogen injection flash, rotation...). The complex interplay of these mechanisms can either lead to the destruction or the production of Li and F. Our observations bring some more constrains to understand AGB stars, but more are needed. Furthermore, there is still a lot of improvement to be made in the analysis and in particular concerning molecular linelists. We plan to build new sets of accurate linelists that could be used for accurate abundance measurements.

References

- Karakas, A., & Lattanzio, J. C. 2007, PASA, 24, 103
- Karakas, A. I. 2010, MNRAS, 403, 1413
- Lucatello, S., Masseron, T., Johnson, J. A., Pignatari, M., & Herwig, F. 2011, ApJ, 729, 40
- Masseron, T., Johnson, J. A., Plez, B., et al. 2010, A&A, 509, A93

STELLAR PARAMETERS AND CHEMICAL TAGGING OF NEARBY FGK STARS: TESTING MEMBERSHIP TO STELLAR KINEMATIC GROUPS

D. Montes¹ and H.M. Tabernerero, J.I. González Hernández, et al.

Abstract. Thanks to the spatial missions Planck and Herschel, we are currently exploring a previously unknown part of the Galaxy: the cold and dense interstellar medium (ISM). The interpretation of these results requires detailed knowledge of the spatial distribution of its dust and gas, as well as the surrounding stars. Accurate distance and extinction measurements from the Gaia satellite will allow us for the first time to truly explore the ISM, and therefore stellar birthplaces, in three dimensions.

¹ UCM, Universidad Complutense de Madrid, Spain

SPITZER CHARACTERIZATION OF DUST IN THE IONIZED MEDIUM OF THE LARGE MAGELLANIC CLOUD

D. Paradis^{1,2,3}, R. Paladini³, A. Noriega-Crespo³, G. Lagache⁴, A. Kawamura⁵, T. Onishi⁶ and Y. Fukui⁵

Abstract. Dust emission associated with ionized gas has so far been detected only in our Galaxy, and for wavelengths longer than 60 μm . Spitzer data now offer the opportunity to carry out a similar analysis in the Large Magellanic Cloud, and to separate dust emission into components associated with different phases of the gas, i.e. atomic, molecular and ionized. We perform a correlation study using infrared Spitzer data as part of the Surveying the Agents of a Galaxy's Evolution (SAGE) and IRAS 12-100 μm combined with gas tracers such as the ATCA/Parkes HI data, for the atomic phase, the NANTEN ^{12}CO data, for the molecular phase, and both the SHASSA $\text{H}\alpha$ and the radio Parkes 5 GHz data, for the ionized phase. In particular, we investigate the presence of dust for different physical regimes of the ionized gas, spanning emission measures from 1 pc cm^{-6} (diffuse medium) to 10^3 pc cm^{-6} (HII regions).

Keywords: dust, extinction, HII regions, Magellanic Clouds

1 Introduction

The Large Magellanic Cloud (LMC), located at a distance of 50 kpc has an advantageous almost face-on viewing angle, with small contamination along the line of sight (LOS). Assessing the presence of dust in the ionized gas phase is very important given that the optical properties of dust grains can vary with the properties of the local environment. In the ionized medium, due to the proximity of the ionized gas with UV sources, such as O and B stars, and the cumulative effect of shock fronts, changes in the optical dust properties are indeed expected. For instance, depletion of polycyclic aromatic hydrocarbons (PAHs) has been observed towards individual HII regions. However, this phenomenon does not appear to be systematic. We present a systematic investigation of the dust properties associated with the ionized gas in the LMC. The full description of this analysis is presented in Paradis et al. (2011a).

2 Data

We use the following data set:

- Infrared: Spitzer data as part of the SAGE program (Meixner et al. 2006), from 3.6 to 160 μm , combined with IRAS 12-100 μm ($4'$ angular resolution).
- HI: 21 cm integrated intensity map (W_{HI}), obtained from the combined ATCA ($1'$ Kim et al. 2003) and Parkes data ($4'$ Staveley-Smith et al. 2003). Assuming the gas is optically thin, we derive: $N_{\text{H}} = 1.82 \times 10^{18} W_{\text{HI}}$.

¹ Universite de Toulouse; UPS-OMP, IRAP, Toulouse, France

² CNRS; IRAP, 9 av. du Colonel Roche, BP 44346, 31028, Toulouse, cedex 4, France-Spitzer Science Center, California Institute of Technology, 1200 E. California Blvd, Pasadena, CA 91125, USA

³ Spitzer Science Center, California Institute of Technology, 1200 E. California Blvd, Pasadena, CA 91125, USA

⁴ Institut d'Astrophysique Spatiale, 91405 Orsay, France

⁵ Department of Astrophysics, Nagoya University, Chikusa-ky, Nagoya 464-8602, Japan

⁶ Department of Physical Science, Osaka Prefecture University, Gakuen 1-1, Sakai, Osaka 599-8531, Japan

- CO: $^{12}\text{CO}(J=1-0)$ integrated intensity map (W_{CO}), second survey (2'6, Fukui et al. 2008) obtained with the 4-m radio NANTEN telescope. We compute $N_H = 2X_{\text{CO}}W_{\text{CO}}$, using X_{CO} values deduced from virial masses for each cloud (Fukui et al. 2008).
- H α : SHASSA survey (Gaustad et al. 2001), with an angular resolution of 0'8. We compute $N_H = 1.37 \times 10^{18} I_{\text{H}\alpha} n_e$ (assuming 1R corresponds to an emission measure of $2.25 \text{ cm}^{-6} \text{ pc}$).
- Radio at 5 GHz: Parkes data at a resolution of 5'6 (Filipovic et al. 1995). The data are transformed in H α emission using: $T_b/I_{\text{H}\alpha} = 8.396 \times 10^3 \nu_{\text{GHz}}^2 \nu_{\text{GHz}}^2 T_4^{0.667} 10^{0.029/T_4} (1 + 0.008)$ (Dickinson et al. 2003).

3 Regimes of the ionized gas

We consider three regimes of the ionized gas, from diffuse H $^+$ to bright HII regions, determined using the pixel brightness distribution of the SHASSA map and the Kennicutt & Hodge (1986) catalog of HII regions:

- Case1: diffuse ionized gas $0.8 \text{ R} < \text{H}\alpha < 7 \text{ R}$, $n_e = 0.055 \text{ cm}^{-3}$ (intermediate value from Haffner et al. (2009))
- Case 2: typical HII regions $7 \text{ R} < \text{H}\alpha < 106 \text{ R}$, we derived $n_e = 1.52 \text{ cm}^{-3}$
- Case 3: bright HII regions $106 \text{ R} < \text{H}\alpha < 1000 \text{ R}$, we derived $n_e = 3.98 \text{ cm}^{-3}$

4 Extinction in bright HII regions

The comparison between the SHASSA map and the Parkes data (converted to H α emission) highlights that for 88% of pixels of case 3, the H α -Parkes data are higher than the SHASSA ones, with a median ratio equal to 1.6. To explain such a discrepancy, we invoke extinction as a source of attenuation in the SHASSA map. In our analysis, the factor 1.6 of discrepancy would induce an extinction value in the SHASSA map of 0.51 mag in bright HII regions. Following O'Donnell (1994), Dickinson et al. (2003) estimate the absorption in the H α as $A(\text{H}\alpha) = 0.81A(V)$. The corresponding extinction of LMC bright HII regions in the visible is $A(V)=0.63 \text{ mag}$.

5 Decomposition of the IR emission and modeling

In the LMC, Bernard et al. (2008) evidenced the existence of a large FIR excess with respect to the atomic, molecular and ionized gas phases, which they attributed to either molecular gas with no associated CO emission or to optically thick HI. Following Paradis et al. (2011b), we decompose the IR emission at each wavelength and for each regime, as a function of the atomic, molecular and ionized gas column density:

$$I(\lambda) = a(N_H^{\text{HI}} + N_H^{\text{X}}) + bN_H^{\text{CO}} + cN_H^{\text{H}^+} + d \quad (5.1)$$

with N_H^{X} the column density in the FIR excess component. In the following, we refer to the sum of the atomic and FIR excess components as the atomic phase.

The H α map is used for the three regions as a tracer of the H $^+$ column density, whereas radio map at 5 GHz is used only for case 3 due to its lower sensitivity.

The thermal fraction of the 5 GHz map (f_{th}) has been estimated, using:

$$\frac{S_5}{S_{1.4}} = f_{\text{th}} \left(\frac{\nu_5}{\nu_{1.4}} \right)^{-\alpha_{\text{ff}}} + (1 - f_{\text{th}}) \left(\frac{\nu_5}{\nu_{1.4}} \right)^{-\alpha_{\text{sync}}} \quad (5.2)$$

where S_5 and $S_{1.4}$ are the total flux densities at 5 and 1.4 GHz, and α_{ff} and α_{sync} are the free-free and synchrotron spectral indices, taken equal to 0.1 and 0.6 respectively. We derive an average thermal fraction of 0.85 in bright HII regions of the LMC.

First, we assume a single radiation field along the LOS. We model the spectral energy distributions (SEDs) associated with each phase of the gas using DustEM (Compiègne et al. 2011, see Fig. 2). We impose, for dust emission associated with the atomic and molecular phases, as well as for dust emission associated with the diffuse ionized gas in case 1, the same interstellar radiation field (RF) hardness as for the solar neighborhood (Mathis et al. 1983). However for cases 2 and 3, dust in the ionized phase is associated with typical and bright

HII regions, and therefore it is essentially heated by local hot stars. For these cases, using the GALEV code*, we have generated an UV/visible spectrum of young stellar clusters of 4 Ma. Second, we test our results using a combination of several RF intensities and hardnesses along the LOS. For this purpose we apply the Dale et al. (2001) model that considers a local SED combination by assuming a power-law distribution of dust mass subjected to a given heating intensity.

6 Results

We evidence for the first time dust emission associated with the ionized gas of the LMC. We report:

- A systematic warmer dust temperature in the H⁺ phase compared to the HI and CO phases
- An emissivity in the diffuse H⁺ of 2.3×10^{-26} cm²/H at 160 μ m, lower than Galactic values by a factor higher than the metallicity ratio between the two galaxies. This result suggest different properties of dust in the H⁺ gas of the LMC, compared to our Galaxy.
- A significant decrease of the PAH relative abundance in the H⁺ phase of all cases (1, 2, 3) with respect to the HI and CO phases, with a larger difference between the phases for cases 2 and 3. We interpret this result as due to PAH destruction caused by the increased radiation field in the H⁺ phase, although the origin of this phenomenon is still under investigation.
- The survival of the PAHs in the molecular phase. In addition, when one compares bright with typical HII regions, the H⁺ phase shows an enhancement of the very small grains relative abundance by more than a factor of 2.
- An important increase of a near-infrared continuum in the H⁺ phase, which does not seem to correlate with PAH emission.
- A systematic increase of the dust emission going from the diffuse medium to bright HII regions, for all gas components.

References

- Bernard, J.-P., et al. 2008, ApJ, 136, 919
 Compiègne, M., et al. 2011, A&A, 525, 103
 Dale, D. A., et al. 2001, ApJ, 549, 215
 Dickinson, C., Davies, R. D., and Davis, R. J. 2003, MNRAS, 341, 369
 Filipovic, M. D. et al. 1995, A&AS, 111, 311
 Fukui, Y., et al. 2008, ApJS, 178, 56
 Gaustad, J. E., McCullough, P. R., Rosing, W., & van Buren, D. 2001, PASP, 113, 1326
 Haffner, L. M., et al. 2009, RvMP, 81, 969
 Kennicutt, R. C., & Hodge, P. W. 1986, ApJ, 306, 130
 Kim, S., et al. 2003, ApJS, 148, 473
 Mathis, J. S., Mezger, P. G., & Panagia, N. 1983, A&A, 128, 212
 Meixner, M., et al. 2006, AJ, 132, 2268
 O'Donnell, J. E. 1994, ApJ, 422, 158
 Paradis, D. et al. 2011a, ApJ, 735, 6
 Paradis, D. et al. 2011b, AJ, 141, 43
 Staveley-Smith, L., et al. 2003, MNRAS, 339, 87

*available at <http://www.galev.org>

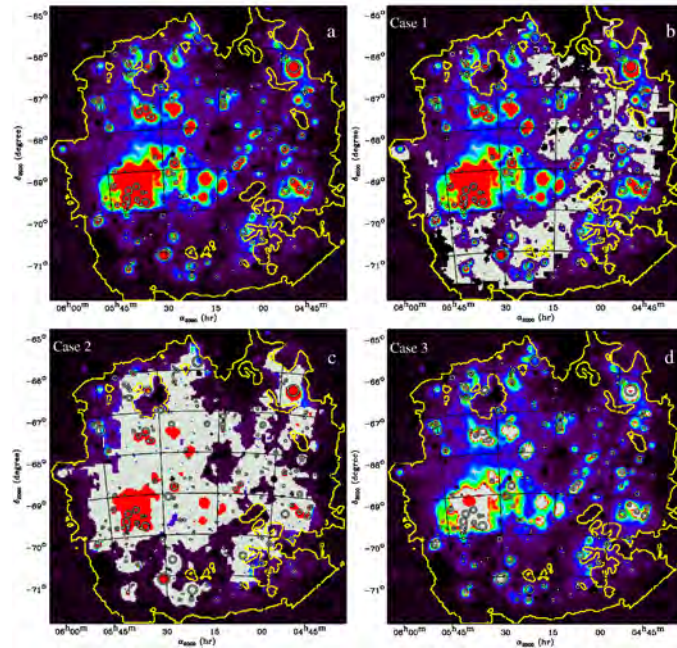


Fig. 1. SHASSA H α map (a) and spatial locations of pixels (in gray) selected for each case: (b) case 1 (diffuse ionized gas), (c) case 2 (typical HII regions), and (d) case 3 (bright HII regions). The overlaid symbols show the HII regions (Kennicutt & Hodge 1986). The range of the maps is $[-8; 100]$ R.

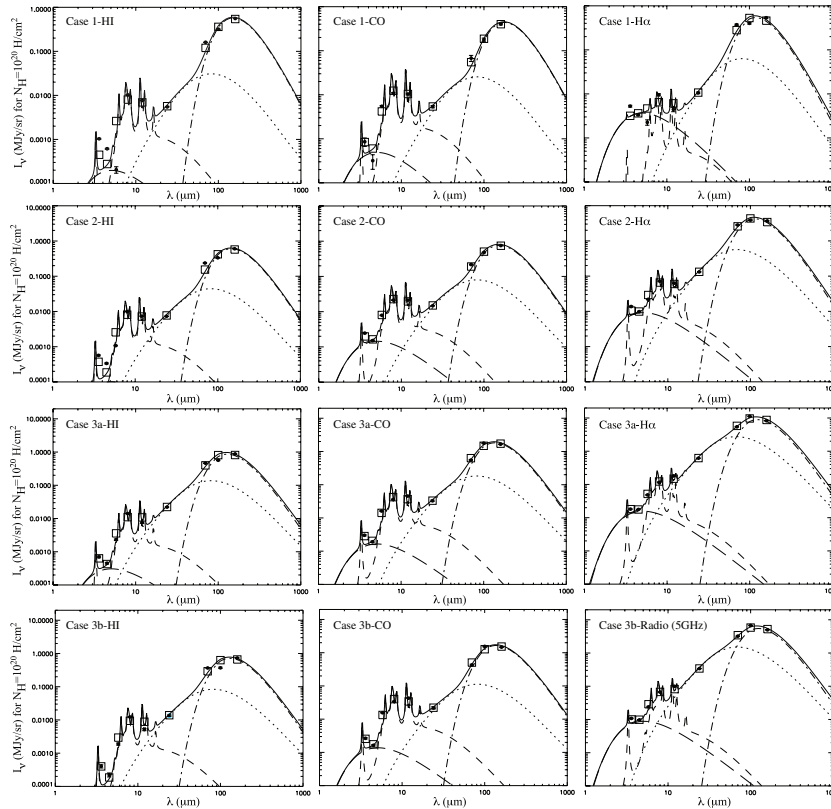


Fig. 2. Results of the fits obtained with the dust emission model (DustEM) assuming a single RF along the LOS. The squares show the fits of the model after applying the color-correction. Different curves denote the contributions from various grain populations: total (solid), big grains (dot-dash), very small grains (dot), polycyclic aromatic hydrocarbons (dash) and a near-infrared continuum (long dash).

SPADES: A STELLAR PARAMETERS DETERMINATION SOFTWARE

H. Posbic¹, D. Katz¹, E. Caffau², P. Bonifacio¹, L. Sbordone², A. Gomez¹ and F. Arenou¹

Abstract. With the large amounts of spectroscopic data available today and the very large surveys to come (e.g. Gaia), the need for automatic data analysis software is unquestionable. We thus developed an automatic spectra analysis program for the determination of stellar parameters: radial velocity, effective temperature, surface gravity, micro-turbulence, metallicity and the elemental abundances of the elements present in the spectral range. Target stars for this software should include all types of stars. The analysis method relies on a line by line comparison of the spectrum of a target star to a library of synthetic spectra. The idea is built on the experience acquired in developing the TGMET (Katz et al. 1998, Soubiran et al. 2003), ETOILE (Katz 2001) and Abbo (Bonifacio & Caffau 2003) software. The method is presented and the performances are illustrated with GIRAFFE-like simulated spectra with high resolution ($R = 25000$), with high and low signal to noise ratios (down to $\text{SNR} = 30$). These spectra should be close to what could be targeted by the Gaia-ESO Survey (GCDS).

Keywords: stellar parameters, spectra analysis, Giraffe

1 Introduction

One of the major applications of spectroscopy is the determination of stellar parameters like the radial velocity (V_r), effective temperature (T_{eff}), surface gravity ($\log g$), micro-turbulence (ξ), metallicity ($[\text{Fe}/\text{H}]$) and chemical abundances ($[\text{X}/\text{H}]$). The present and future large spectroscopic surveys are going to significantly increase the number of spectroscopic data to be analysed. A few examples are the Gaia-ESO Survey with about 160000 stars to be observed, Gaia with about 2×10^6 stars to be analysed for chemical abundances (Katz et al. 2004), RAVE with some 400000 stars observed so far (Boeche et al. (2011) and Siebert et al. (2011)) etc. The space mission Gaia will provide the largest survey ever, and that, in the decade to come. To analyse these quantities of data, automatic spectra analysis software is needed. Different families of software exist. A few examples are software like TGMET (Katz et al. (1998) and Soubiran et al. (2003), ETOILE (Katz 2001), MATISSE (Recio-Blanco et al. 2006), Abbo (Bonifacio & Caffau 2003) etc... The work presented is about the development of a new automatic stellar spectra analysis software. In its first version the software will be optimised for medium-resolution Giraffe spectra (VLT) and will thus be tested on Giraffe like spectra. The software is called SPADES (Stellar PArameters DEtermination Software) and is coded with Java.

2 SPADES

2.1 General idea

The software is based on the comparison between observed spectra and a grid of synthetic spectra (with known parameters). Contrary to many existing software, in SPADES, the comparison between spectra is not made over all the spectrum but around pre-selected lines. Another particularity is that the determination of the stellar parameters does not use any equivalent width measures but is based on profile fitting methods. Another important characteristic of SPADES is that it determines elemental abundances. The general idea is as follows:

For each parameter to be determined, one or several methods of determination (diagnostics) are available. One is chosen by the user. The list of diagnostics for each parameter are:

¹ GEPI, Observatoire de Paris, CNRS, Université Paris Diderot, Place Jules Janssen, 92190 Meudon, France

² Zentrum für Astronomie der Universität Heidelberg, Landessternwarte, Königstuhl 12, 69117 Heidelberg, Germany

- V_r : cross-correlation in direct space with a template
- T_{eff} : excitation equilibrium or Balmer lines profile fitting.
- $\log g$: ionization equilibrium or strong lines (e.g. MgIb green triplet) profile fitting.
- $[\text{Fe}/\text{H}]$: Fe lines profile fitting.
- $[\text{X}/\text{H}]$: X lines profile fitting.
- ξ : empiric calibration or nulling the $\Delta W = f(\text{reduced equivalent widths})$ function slope. ΔW being the residuals of the difference between the observed and synthetic line.

The diagnostics so far implemented and tested are detailed in the next section. Each of the parameters, T_{eff} , $\log g$, $[\text{Fe}/\text{H}]$ and ξ atmospheric parameters is determined one by one assuming all the others known. The process is iterated until convergence. The elemental chemical abundances are then determined.

2.2 Diagnostics

2.2.1 Effective temperature : T_{eff}

H α wings fit method. The first step is defining the reference grid to be used: a 1D (in the parameters space) reference spectra grid is defined. This grid varies over T_{eff} only, the other parameters being fixed to their input values. This grid is read or calculated by interpolation based on a pre-calculated reference spectra grid. The analysis is limited to the H α line, more generarely to a spectral range around this line. This range will be now called the ‘‘H α spectral domain’’. For each reference spectrum (T_{eff} value), the H α spectral domain continuum is fitted to the studied H α spectral domain continuum. An example of superposed continuum fitted H α spectral domains is presented in Fig. 1 (Left). The spectral domains differ by their T_{eff} .

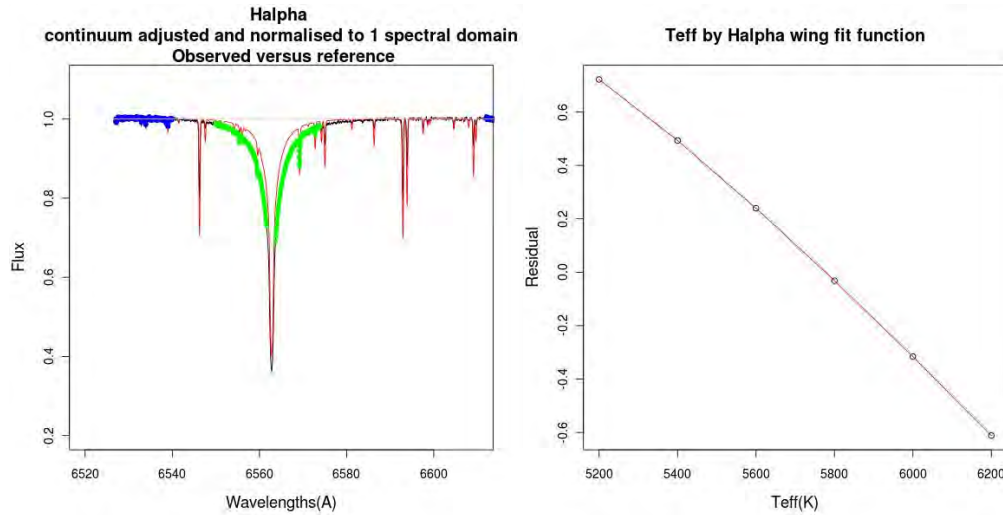


Fig. 1. Left: The reference spectrum H α spectral domain in red is superposed to the studied spectrum H α spectral domain in black. The continuum pixels are in blue. The H α wings pixels are in green. **Right:** The residuals as function of the reference spectra T_{eff} . The result T_{eff} is the value that nulls this function.

The wavelengths ranges used for the continuum fit are pre-defined. The corresponding pixels are in blue. The green pixels represent the H α wings. The wavelength limits of the wings are also pre-defined. Over the H α wings pixels the residual is calculated as: $s = \sum_{\text{pixels}} (x_{\text{obs}} - \tilde{x}_{\text{ref}})$. That is done for all the spectra in the 1D reference spectra grid. $s = f(T_{\text{eff}}(\text{ref}))$ is thus constructed. An example of this function is presented in Fig. 1 (Right). The result T_{eff} is the one that nulls this function.

Excitation equilibrium. In this method a list of pre-selected FeI lines is used. As in the previous method, a 1D (in the parameters space) reference spectra grid is defined with T_{eff} values varying around the input value while the other parameters are fixed to their input values. Around each central wavelength a spectral domain is cut in the reference and observed spectra. The line and continuum limits are determined automatically. For each reference spectrum, the spectral domains around the pre-selected lines are continuum fitted to the continuum of their corresponding spectral domain in the studied spectrum. An example of superposed, continuum fitted spectral domains is given in Fig. 2.

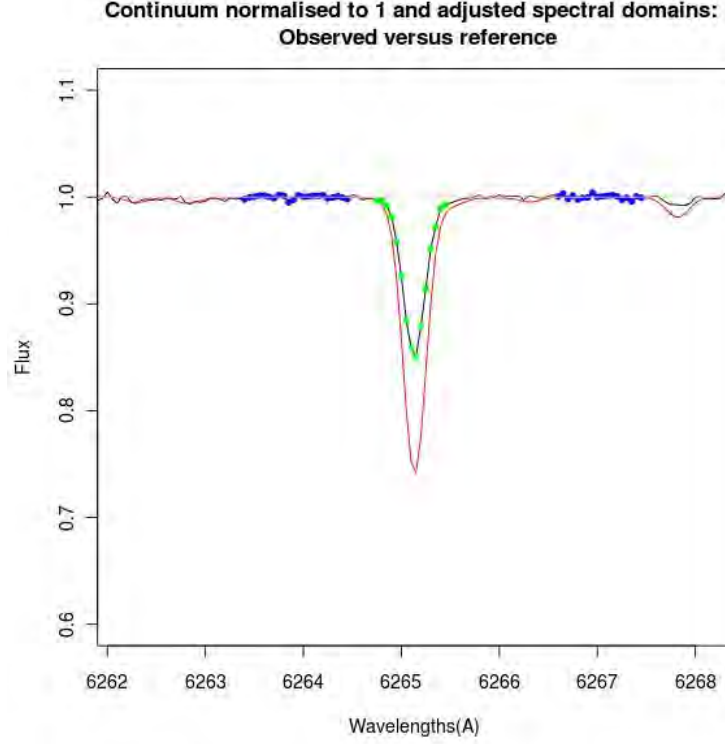


Fig. 2. In red the spectral domain of a FeI line in the reference spectrum superposed to the studied spectral domain of the same line, in black. The studied and the reference spectra are at different T_{eff} s which explains the difference between the line. The continuum pixels are in blue. The line pixels are in green.

For each reference spectral domain, and over the line pixels (green pixels) the residual is measured as such: $\Delta W = \sum_{\text{pixels}} -(x_{\text{obs}} - \tilde{x}_{\text{ref}})$.

This measurement is done for all the used lines. Let ΔW_n be the residual of the n th line. For each reference spectrum, the lines ΔW_n are plotted as a function of the lines respective excitation potentials ξ_n . An example of this function is given in Fig. 3 (Left).

For each reference spectrum (T_{eff} value) the slope a of this function is measured ($\Delta W_n = a * \xi_n + b$). Another function is then constructed: the $a = f(T_{\text{eff}})$ function. An example of this function is presented in Fig. 3 (Right). The result T_{eff} is the one that nulls the $a = f(T_{\text{eff}})$ function.

2.2.2 Gravity: $\log g$

Ionisation equilibrium. In this method the measurement made over the FeI and the FeII lines to be used are: $\Delta W_{\text{FeI}} = \sum_{\text{pixels}} -(x_{\text{obs}} - \tilde{x}_{\text{ref}})$ and $\Delta W_{\text{FeII}} = \sum_{\text{pixels}} -(x_{\text{obs}} - \tilde{x}_{\text{ref}})$.

The diagnostic to be analysed is : $\Delta = \Delta \bar{W}_{\text{FeI}} - \Delta \bar{W}_{\text{FeII}}$ where $\Delta \bar{W}_{\text{FeI}}$ (respectively $\Delta \bar{W}_{\text{FeII}}$) are the mean of the $\Delta W_{\text{FeI},n}$ s (respectively the $\Delta W_{\text{FeII},n}$ s) for all the FeI (respectively the FeII) lines. The result $\log g$ nulls the Δ as a function of the reference spectra $\log g$ function.

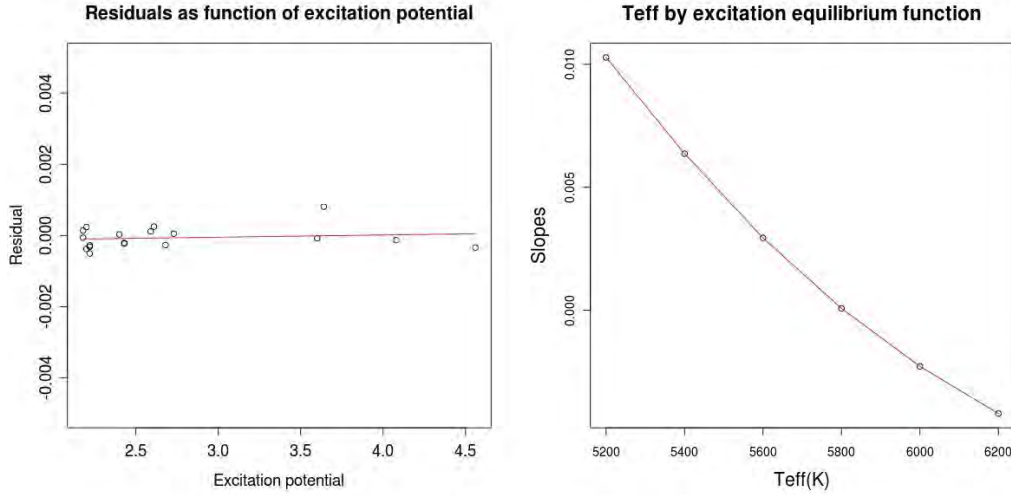


Fig. 3. Left: Line residuals (ΔW_n) as function of excitation potentials ξ_n for the reference spectrum with $T_{\text{eff}} = 5800$ K. **Right:** The slopes such as $\Delta W_n = a * \xi_n + b$ as a function of the reference spectra T_{eff} . The result T_{eff} is the value that nulls this function.

2.2.3 Metallicity and elemental abundances: [X/H]

Profile fit. In this method the measurement over the n lines of the X element to be used is : $s^2 = \sum_{pixels} (x_{obs} - \tilde{x}_{ref})^2 / \sigma^2$. The diagnostic to be analysed over all the X element lines is: $S^2 = \sum_{lines} \sum_{pixels} (x_{obs} - \tilde{x}_{ref})^2 / \sigma^2$. The result [X/H] is the one that nulls the S^2 as function of the reference spectra [X/H] function.

2.3 Tests and performances

SPADES was tested by Monte-Carlo over synthetic spectra with resolution $R = 25000$, effective temperature $T_{\text{eff}} = 5800$ K, gravity $\log g = 4.40$, metallicity $[Fe/H] = -1.0$, with individual abundances of Ca and Ni: $[Ca/H] = 0.0$ and $[Ni/H] = 0.0$. The tests were made for 2 signal to noise ratios (SNR): 30 and 100 (200 reference spectra for each SNR). The values of the dispersions at $1 - \sigma$ of the residuals (difference between the estimated and the real value) for each parameter are as follows (Table 1).

Table 1. Monte-Carlo simulations.

| | $SNR = 30$ | $SNR = 100$ |
|----------------------|------------|-------------|
| T_{eff} (K) | 31 | 9 |
| $\log g$ | 0.14 | 0.05 |
| [Fe/H] (dex) | 0.04 | 0.0013 |
| [Ca/H] (dex) | 0.03 | 0.009 |
| [Ni/H] (dex) | 0.05 | 0.017 |

The mean results of these Monte-Carlo runs for each parameter show no bias. The dispersions are acceptable. Actually, for the T_{eff} determination using the $H\alpha$ method, the dispersion is at SNR of 100 (respectively 30) about 10 times (respectively 3 times) smaller than the systematic error (estimated by Cayrel et al. 2011) linked to the physics behind the models used. We note that, of course, the $H\alpha$ line is not always available for use: one reason is that it can simply not be in the spectral domain used, another is that this T_{eff} determination method cannot be used for all stars (cool stars for example). The excitation equilibrium method is then used.

3 Future work

The future work to be done on the software is :

- On the fly reference grid calculation: dynamic call of the SYNTHE software for calculating the reference grid directly from SPADES (completed at the time of writing the proceedings)
- Fix a method for determining micro-turbulence
- Determine the external errors (as opposed to the internal errors determined by Monte-Carlo). One of the methods will be the test on known stars (e.g. Sun)
- In its first version, the software will be fine-tuned to analyze medium to high resolution GIRAFFE spectra of Thick Disk stars .

References

- Boeche, C., Siebert, A., Williams, M., et al. 2011, ArXiv e-prints 1109.5670
- Bonifacio, P. & Caffau, E. 2003, *A&A*, 399, 1183
- Cayrel, R., van't Veer-Menneret, C., Allard, N. F., & Stehlé, C. 2011, *A&A*, 531, A83
- Katz, D. 2001, *Journal of Astronomical Data*, 7, 8
- Katz, D., Munari, U., Cropper, M., et al. 2004, *MNRAS*, 354, 1223
- Katz, D., Soubiran, C., Cayrel, R., Adda, M., & Cautain, R. 1998, *A&A*, 338, 151
- Recio-Blanco, A., Bijaoui, A., & de Laverny, P. 2006, *MNRAS*, 370, 141
- Siebert, A., Williams, M., Siviero, A., et al. 2011, *VizieR Online Data Catalog*, 3265, 0
- Soubiran, C., Bienaymé, O., & Siebert, A. 2003, *A&A*, 398, 141

THE PHYSICAL PARAMETERS OF THE LOW-MASS MULTIPLE SYSTEM LHS1070 FROM SPECTRAL SYNTHESIS ANALYSIS

A. S. Rajpurohit¹, C. Reylé¹, M. Schultheis¹, C. Leinert² and F. Allard³

Abstract. LHS1070 is a nearby multiple systems of low mass stars. It is an important source of information for probing the low mass end of the main sequence, down to the hydrogen-burning limit. The primary of the system consist of a mid-M dwarf and two components are late-M to L dwarf, at the star-brown dwarf transition. It makes it even more valuable to understand the formation of dust in cool stellar atmospheres. This work aims to determine the fundamental parameters of LHS1070 and to test recent model atmospheres. We compared the well calibrated data in the optical and infra-red with synthetic spectra computed from recent cool stars atmosphere models. We derived the physical parameters T_{eff} , radius and $\log g$ for three components of LHS1070. The models which include the formation and settle of dust are able to reproduce and describe the main features of the visible to IR spectra of the components.

Keywords: stars: atmospheres, stars: fundamental parameters, stars: low-mass

1 Introduction

M dwarfs are the most numerous stars in our Galaxy which makes them an important probe for our galaxy as they carry fundamental informations regarding the stellar physics, galactic structure and formation, and its dynamics. In addition the existence of brown dwarfs or planets being discovered and confirmed around M-dwarfs (Butler et al. 2004; Bonfils et al. 2005) plays an important role for the knowledge of the formation of brown dwarfs and planets. The energy distribution in these late type stars is governed by various absorption molecular bands like TiO, CaH, VO in the optical and H₂O and CO bands in the infrared. The presence of these molecular bands dominates the spectrum in the visible and infared. This affects the resulting opacity in the photosphere of these stars and leads to an onset of the dust formation in the photospheric layers (Tsuji et al. 1996a,b; Allard et al. 1998). In particular, the wavelength region from 6300 Å to 9000 Å encompasses a number of TiO and VO bands which are blended with other lines and leaves no window on the true continuum. Because of their complex atmosphere, a reliable way to determine the physical parameters of M-dwarfs is to compare the observed spectra with synthetic spectra. Atmospheric modeling allows us to determine the fundamental reason for such changes in the cool atmosphere and also helps to determine the physical parameters of the M-dwarfs (Bean et al. 2006).

LHS1070 is a low mass multiple system of cool dwarfs discovered by Leinert et al. (1994), with visual magnitude 15. It is located at a distance of 7.72 ± 0.15 pc from the Sun (Costa et al. 2005) and is considered as a member of the old disk population with a probable age of several Ga (Leinert et al. 2001). The spectral type for the A, B and C components was found to be M5.5-M6, M8.5 and M9-M9.5 (Leinert et al. 2000). Components A,B, and C were the faintest stars within 10 pc from the Sun for which dynamical determinations of mass appeared possible. Leinert et al. (2001); Seifahrt et al. (2008) constrained the combined mass of components B and C and showed that their mass is very close to the hydrogen burning minimum mass, in good agreement with the masses of $0.080\text{-}0.083M_{\odot}$ and $0.079\text{-}0.080M_{\odot}$ derived by Leinert et al. (2000) from theoretical mass-luminosity relations (Baraffe et al. 1998; Chabrier et al. 2000).

¹ Université de Franche Comté, Institut UTINAM CNRS 6213, Observatoire des Sciences de l'Univers THETA de Franche-Comté, Observatoire de Besançon, BP 1615, 25010 Besançon Cedex, France.

² Max-Planck-Institut für Astronomie, Königstuhl 17, 69117 Heidelberg, Germany.

³ Centre de Recherche Astrophysique de Lyon, UMR 5574: CNRS, Université de Lyon, École Normale Supérieure de Lyon, 46 allée d'Italie, F-69364 Lyon Cedex 07, France.

The mass range spanned by the components of LHS1070 makes it a valuable system to study, for understanding the formation of dust in the cool atmospheres and the processes that occur at the star/brown dwarf transition. The comparison of the observed spectra of this system with recent atmospheric models helps to determine the stellar parameters (effective temperature, $\log g$, metallicity, radius) and provides an unique opportunity to better understand the lower end of the main sequence which is still poorly understood. LHS1070 is also a testbed to validate and define further developments of the atmospheric models.

2 Model Atmospheres

In this study, we have used the recent new BT-Settl models (Allard et al. 2010) for our analysis of LHS1070. These model atmospheres are computed with the PHOENIX code using hydrostatic equilibrium, convection using the Mixing Length Theory and a mixing length of $1/H_p=2.0$ according to results of radiation hydrodynamics (Ludwig et al. 2006), spherically symmetric radiative transfer, departure from LTE for all elements up to iron, the latest solar abundances by (Asplund et al. 2009), equilibrium chemistry, an important database of the latest opacities and thermochemical data for atomic and molecular transitions, and monochromatic dust condensates refractory indexes. Grains are assumed spherical and non-porous, and their Rayleigh and Mie reflective and absorptive properties are considered. The diffusive properties of grains are treated based on 2-D radiation hydrodynamic simulations, including forsterite cloud formation to account for the feedback effects of cloud formation on the mixing properties of these atmospheres Freytag et al. (2010). For this paper, we use the model grid described as follows: T_{eff} from 2000 K to 4000 K with 100 K step, $\log g = 5.0$ dex, 5.5 dex, $M/H = -1.5$ dex, -1.0 dex, -0.5 dex, 0 dex, +0.3 dex, +0.5 dex.

We have also used the grid of MARCS model atmosphere (Gustafsson et al. 2008). These models are hydrostatic and computed on the assumptions of Local Thermodynamic Equilibrium (LTE), chemical equilibrium, homogeneous plane-parallel stratification, and the conservation of the total flux (radiative plus convective; the convective flux being computed using the local mixing length recipe). The radiation field used in the model generation is calculated by assuming absorption from atoms and molecules by opacity sampling at approximately 100000 wavelength points over the range 1300 Å to 20 μm. This grid spans effective temperatures between $2550 \text{ K} < T_{eff} < 4050 \text{ K}$ in steps of 100 K, surface gravities of $5.0 < \log g(\text{cgs}) < 5.5$ in steps of 0.5 dex, a constant microturbulence of 2 km s^{-1} , and metallicities of $-0.5 < [\text{Fe}/\text{H}] < 0.25$ in steps of 0.25 dex and with an $[\alpha/\text{Fe}] = +0.2$ and $+0.1$ for the two lowest metallicities, respectively.

The model spectra are converted to absolute fluxes ($\text{erg cm}^{-2} \text{ s}^{-1} \text{ \AA}^{-1}$) at the position of the observer by multiplying with the dilution factor $[r/d]^2$ where the stellar radii are varying from $0.096R_{\odot}$ to $0.142R_{\odot}$ at a step of 0.002 by assuming the distance for the system 7.72 pc (Costa et al. 2005).

3 Physical Parameters Determination and Results

3.1 Effective Temperature and Radius

The effective temperature and radius have been calculated using a χ^2 minimization technique in an automatic interactive way in IDL program. In this technique we first rebin all the synthetic spectra both in optical and infrared to the same resolution as the observed spectra. For all of the observed spectra we then calculate the χ^2 value compared to the grid of the synthetic spectra in the wavelength range between 4500 Å to 2.4 μm. Due to the low S/N ratio of the observed spectra, we excluded the region below 4500 Å. In a second step a 3-D χ^2 map has been obtained for each of the component in the optical and in infrared as a function of temperature and radius. The 3-D χ^2 plot both in optical and in IR shows clearly the parameter space which gives an acceptable solution. We then compared the possible solutions in the optical and IR for each component. The common intersection between the solutions in the optical and infrared were considered as the best physically acceptable solution. The solution was then crossed checked by visual inspection by overplotting them with the observed spectra. The same procedure has been used with both BT-Settl and MARCS model. The derived parameters are given in Table 1. Figure 1 shows the best fit model superimposed to the observed optical and IR spectra for all the three components using BT-Settl and MARCS model.

3.2 Gravity and metallicity

Assuming the stellar radii from theoretical evolutionary model (Baraffe et al. 1998; Baraffe 1999), and the masses computed by Seifahrt et al. (2008), the $\log g$ of the components is found to be close to 5.3. We therefore

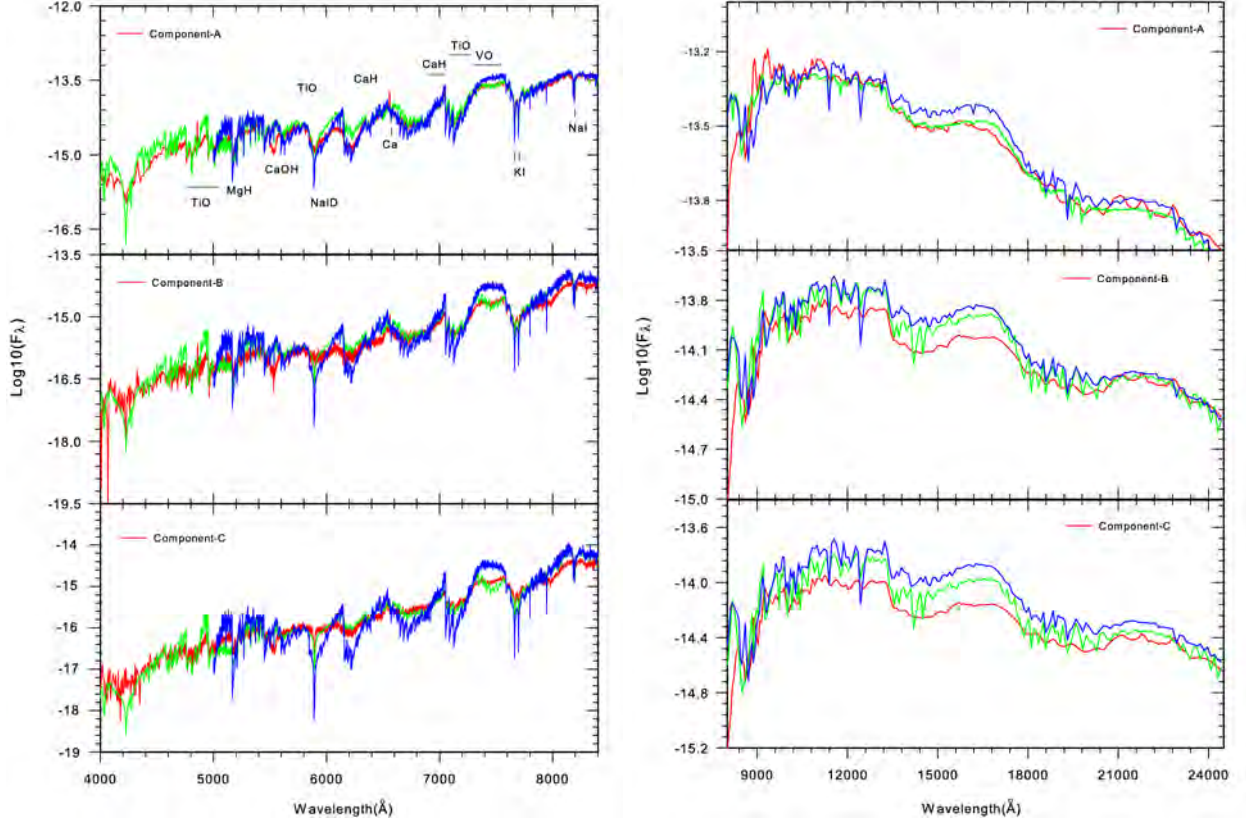


Fig. 1. Optical (left) and Infra-red (right) spectra of all three components. Red: observed spectra. Green: best fit BT-Settl model. Blue: best fit MARCS model. The parameters that give the best fit are given in Table 1.

Table 1. Derived parameters for the LHS1070 system. The uncertainties are drawn from the χ^2 maps and is 100 K for T_{eff} . The metallicity is assumed to be $[m/H] = 0$ and $\log g = 5.0$ to 5.5

| Component | Spec. Type | BT-Settl model | | | MARCS model | | | |
|-----------|------------|----------------|---------------|----------|------------------------|---------------|----------|------------------------|
| | | $[m/H]$ | T_{eff} (K) | $\log g$ | Radius (R_{\odot}) | T_{eff} (K) | $\log g$ | Radius (R_{\odot}) |
| A | M5.5-M6 | 0.0 | 2900 | 5.5 | 0.134 ± 0.005 | 2900 | 5.0 | 0.136 ± 0.005 |
| B | M8.5 | 0.0 | 2500 | 5.5 | 0.102 ± 0.004 | 2600 | 5.0 | 0.098 ± 0.002 |
| C | M9.5-M9 | 0.0 | 2400 | 5.5 | 0.098 ± 0.002 | 2500 | 5.0 | 0.100 ± 0.002 |

restrict our analysis with gravity of 5.0 and 5.5 dex. The surface gravity can be obtained by analyzing the atomic line like K I, Na I and metal hydride like CaH which are gravity sensitive. K I line line 7665 Å and 7699 Å is particularly useful gravity discriminant for M stars. The high density of low-mass stars cause an increase in the gravity and thus the pressure broadening will enhanced the line profiles. Figure 2 (left panel) shows such determination of the gravity for the component A from K I line using both BT-Settl and MARCS model. The strength of line suggests that some important dust opacities yet has to be included into the model. The best fit gives us a $\log g = 5.5$ for the BT-Settl models while $\log g = 5.0$ for the MARCS models. However both values agree within the uncertainties as found by Seifahrt et al. (2008).

The main indicator of the metallicity for all three component is the VO absorption band 7300 Å– 7600 Å which is very well reproduced by the BT-Settl model for the solar metallicity for all the components (see Figure 2, right panel).

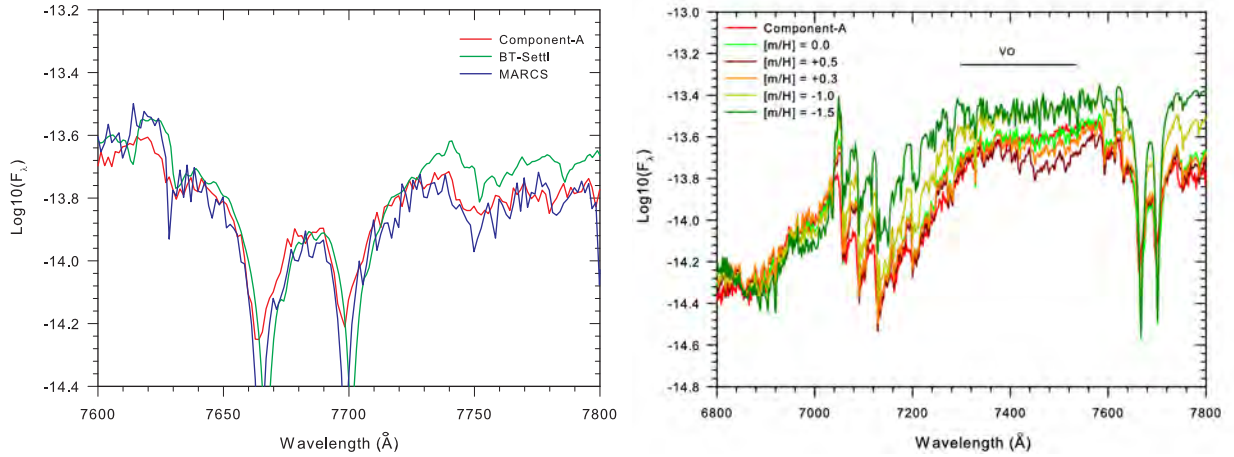


Fig. 2. Left: KI line in the component A (red) compared to the BT-Settl model (green) at $T_{eff} = 2900$ K, $\log g = 5.5$, $R_{\odot} = 0.134$ at solar metallicity along with the MARCS model (blue) at $T_{eff} = 2900$ K, $\log g = 5.0$, $R_{\odot} = 0.136$ at solar metallicity. **Right:** VO band observed in the component A (red) compared to the BT-Settl model at $T_{eff} = 2900$ K, $\log g = 5.5$, $R_{\odot} = 0.134$ at different metallicity

4 Conclusions

This paper presents the results from the spectral synthesis analysis of the LHS1070 triple system. We have determined the physical parameters T_{eff} , $\log g$, metallicity and radius of all the three component by comparing observed spectra with the synthetic spectra computed by BT-settl and MARCS models. The derived parameters agree with those derived using evolutionary models and observed bolometric luminosities (Baraffe et al. 1998; Chabrier et al. 2000). While for the hotter component A the overall agreement between the model and the spectra is satisfactory, we find systematic differences for model B and C. For both components the overall fit is better with the BT-Settl model than the MARCS model. However, we noticed several issues regarding the BT-Settl models. The MgH around 5200 \AA , NaI doublet at around 5900 \AA is far too strong as well as the CaH band at 7000 \AA while the CaOH band is missing. On the other side the TiO and VO band strengths are well reproduced by the models in the NIR part but the calculated fluxes are too high mainly in the J and H band. This may be due to the consideration of too hot deep layers from which the fluxes emerges. This indicates an inaccuracy in the atmosphere structure and also the treatment of the dust grains and opacities in the models as effective temperature decreases which was already proposed by Leggett et al. (2001). There is also clearly a discrepancy in the predicted water bands mainly in the J and H-band visible. Thus LHS1070 can be used as a testbed to validate and define further developments of the atmospheric models.

We acknowledge financial support from "Programme National de Physique Stellaire" (PNPS) of CNRS/INSU, France

References

- Allard, F., Alexander, D. R., & Hauschildt, P. H. 1998, in *Astronomical Society of the Pacific Conference Series*, Vol. 154, *Cool Stars, Stellar Systems, and the Sun*, ed. R. A. Donahue & J. A. Bookbinder, 63
- Allard, F., Homeier, D., & Freytag, B. 2010, *ArXiv e-prints astro-ph.SR 1011.5405*
- Asplund, M., Grevesse, N., Sauval, A. J., & Scott, P. 2009, *ARA&A*, 47, 481
- Baraffe, I. 1999, in *Astronomical Society of the Pacific Conference Series*, Vol. 173, *Stellar Structure: Theory and Test of Connective Energy Transport*, ed. A. Gimenez, E. F. Guinan, & B. Montesinos, p. 111
- Baraffe, I., Chabrier, G., Allard, F., & Hauschildt, P. H. 1998, *A&A*, 337, 403
- Bean, J. L., Sneden, C., Hauschildt, P. H., Johns-Krull, C. M., & Benedict, G. F. 2006, *ApJ*, 652, 1604
- Bonfils, X., Forveille, T., Delfosse, X., et al. 2005, *A&A*, 443, L15
- Butler, R. P., Vogt, S. S., Marcy, G. W., et al. 2004, *ApJ*, 617, 580
- Chabrier, G., Baraffe, I., Allard, F., & Hauschildt, P. 2000, *ApJ*, 542, 464

- Costa, E., Méndez, R. A., Jao, W.-C., et al. 2005, *AJ*, 130, 337
- Freytag, B., Allard, F., Ludwig, H.-G., Homeier, D., & Steffen, M. 2010, *A&A*, 513, A19
- Gustafsson, B., Edvardsson, B., Eriksson, K., et al. 2008, *A&A*, 486, 951
- Leggett, S. K., Allard, F., Geballe, T. R., Hauschildt, P. H., & Schweitzer, A. 2001, *ApJ*, 548, 908
- Leinert, C., Allard, F., Richichi, A., & Hauschildt, P. H. 2000, *A&A*, 353, 691
- Leinert, C., Jahreiß, H., Woitas, J., et al. 2001, *A&A*, 367, 183
- Leinert, C., Weitzel, N., Richichi, A., Eckart, A., & Tacconi-Garman, L. E. 1994, *A&A*, 291, L47
- Ludwig, H.-G., Allard, F., & Hauschildt, P. H. 2006, *A&A*, 459, 599
- Seifahrt, A., Röhl, T., Neuhäuser, R., et al. 2008, *A&A*, 484, 429
- Tsuji, T., Ohnaka, K., Aoki, W., & Nakajima, T. 1996a, *A&A*, 308, L29
- Tsuji, T., Ohnaka, K., Aoki, W., & Nakajima, T. 1996b, *A&A*, 308, L29

PLANCK EARLY RESULTS: THE FIRST ALL-SKY SURVEY OF GALACTIC COLD CLUMPS

I. Ristorcelli¹ and Planck collaboration

Abstract. We present the statistical properties of the first version of the Cold Clump Catalogue of Planck objects (C3PO), in terms of their spatial distribution, temperature, distance, mass and morphology. The temperatures range from 7K to 17K, with a peak around 13K and a dust emissivity spectral index varying from 1.4 to 2. For one third of the objects the distances are derived using methods based on the extinction signature and association with known molecular complexes and infrared dark clouds. Most of the detections are within 2kpc in the solar neighbourhood, but a few are at distances over 4kpc. The sources are distributed over the whole range of longitude and latitude, from the deep Galactic plane to high latitudes. The associated mass estimates derived from dust emission range from 1 to 10^5 solar masses. These cold clumps are not isolated but mostly organized in filaments associated with molecular clouds. The C3PO gives an unprecedented statistical view of the galactic cold clumps including a number of potential pre-stellar objects and offers the possibility of their classification based on their intrinsic properties and environment.

¹ IRAP -CNRS/UPS, Toulouse, France

PRELIMINARY DETERMINATION OF THE NON-LTE CALCIUM ABUNDANCE IN A SAMPLE OF EXTREMELY METAL-POOR STARS*

M. Spite¹, F. Spite¹, P. Bonifacio¹, E. Caffau^{1,2}, S. Andrievsky^{1,3}, S. Korotin³, R. Cayrel¹ and P. François¹

Abstract. The abundance ratios of the elements found in the extremely metal-poor stars (EMP) are a test of the yields predicted by the models of supernovae. For precise comparisons, it is of course preferable to avoid the approximation of LTE. The difference of LTE and NLTE profiles is displayed for three strong lines. The NLTE abundances of Ca are derived from the profiles of about 15 Ca I lines in the EMP giants and about 10 lines in the turnoff stars. The improved abundance trends are consistent with a [Ca/Fe] ratio constant vs. [Fe/H], and with a [Ca/Mg] ratio slightly declining when [Mg/H] increases. Also [Ca/Mg] presents a scatter larger than [Ca/Fe]. As far as the comparison with sulfur (another alpha element) is concerned we find that [S/Ca] presents a scatter smaller than [S/Mg].

Keywords: Galaxy:abundances, Galaxy:halo, Galaxy:evolution, Stars:abundances

1 Introduction

In the frame of the ESO Large Program “First Stars” 52 Extremely Metal-Poor Stars “EMP stars” have been observed with the high resolution spectrograph UVES at the ESO-VLT. In this sample 9 turnoff stars and 22 giants have $[\text{Fe}/\text{H}] < -3$.

These stars are the witnesses of the early Galaxy. The metals contained in their atmosphere have been formed by the first supernovae. The aim of this work was to find the chemical composition of the matter in the early Galaxy, to deduce the characteristics of the first supernovae and to constrain the nucleosynthetic processes. The analysis of the stars has been made under the LTE hypothesis and the main results of this analysis have been published in Cayrel et al. (2004) and Bonifacio et al. (2009).

However we have shown that the derivation of accurate element abundances requires that NLTE effects be taken into account (e.g. Andrievsky et al., 2010, 2011, Spite et al. 2011). We present here an attempt to determine the Ca abundance from NLTE computations.

2 Atmospheric parameters

The adopted values of the atmospheric parameters of the stars were discussed in detail in Cayrel et al. (2004) and Bonifacio et al. (2007).

The temperatures were deduced from the color indices, and also, for the turnoff stars, from the profile of the H α wings. The gravity was derived from the ionization equilibrium of iron and titanium (under the LTE hypothesis).

*Based on observations obtained with the ESO Very Large Telescope at Paranal Observatory, Chile (Large Programme “First Stars”, ID 165.N-0276(A); P.I.: R. Cayrel).

¹ GEPI, Observatoire de Paris, CNRS, Univ. Paris-Diderot, France

² Zentrum für Astron. der Univ. Heidelberg, Germany

³ Dept. of Astronomy and Astronomical Observatory, Odessa National Univ., Ukraine

3 NLTE Abundance of Calcium

In our sample of very metal poor stars about 15 Ca I lines and 2 Ca II lines (the 393.3nm and 866.2nm lines) can be measured.

The NLTE profiles of these lines were computed using a modified version of the MULTI code (Carlsson et al., 1986) described by Korotin et al. (1999).

Our model atom contains 70 levels of Ca I, 38 levels of Ca II, and the ground level of Ca III. The fine structure was taken into account for the levels 3d2D and 4p2P* of Ca II. The ionization cross-sections come from TOPBASE. Collisional rates between the ground level and the ten lower levels of Ca I are based on detailed results available from the R-matrix calculations of Samson & Berrington (2001). For Ca II, collisional rates have been found in Meléndez et al. (2007).

Collisions with hydrogen atoms were taken into consideration using the Steenbock & Holweger (1984) formula with a correction coefficient obtained by fitting the synthetic and the observed profiles of the Ca lines in the Sun and in some reference stars (Procyon, HD 122563 and ν Indi). This correction factor was found to be 0.1, in good agreement with Mashonkina et al. (2007).

At low metallicity the influence of the NLTE is very complex and depends on the line considered. In Fig. 1 we present the LTE and NLTE profiles of the 422.6nm line (Ca I) and the 393.3nm (Ca II K) and 866.2nm lines of Ca II for a giant with $[\text{Fe}/\text{H}] \approx -3$.

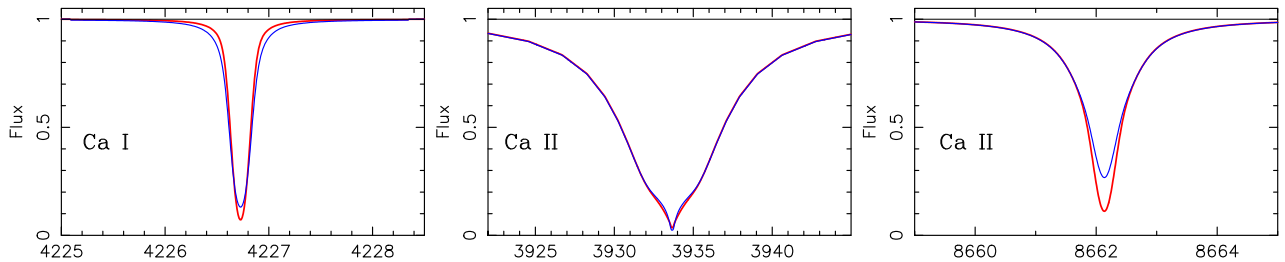


Fig. 1. Profiles of three Ca lines computed for a giant star with $[\text{Fe}/\text{H}] \approx -3$ with LTE (blue) and NLTE (red) hypotheses. **Left:** The profile of the resonance line of Ca I is affected by NLTE effects. The NLTE profile is narrower even in the wings. **Center :** The K Ca II line is practically not affected by NLTE. **Right:** The NLTE correction is important for the strong IR Ca II line, but the wings are not affected and a reliable calcium abundance can be deduced from these wings.

4 Results and Conclusion

The calcium abundance has been derived from about 15 Ca I lines in giants and 10 in dwarfs. In Fig. 2 we present the variation of $[\text{Ca}/\text{Fe}]$ vs. $[\text{Fe}/\text{H}]$ and of $[\text{Ca}/\text{Mg}]$ vs. $[\text{Mg}/\text{H}]$ for our sample of extremely metal-poor stars. (NLTE Mg abundance from Andrievsky et al., 2010).

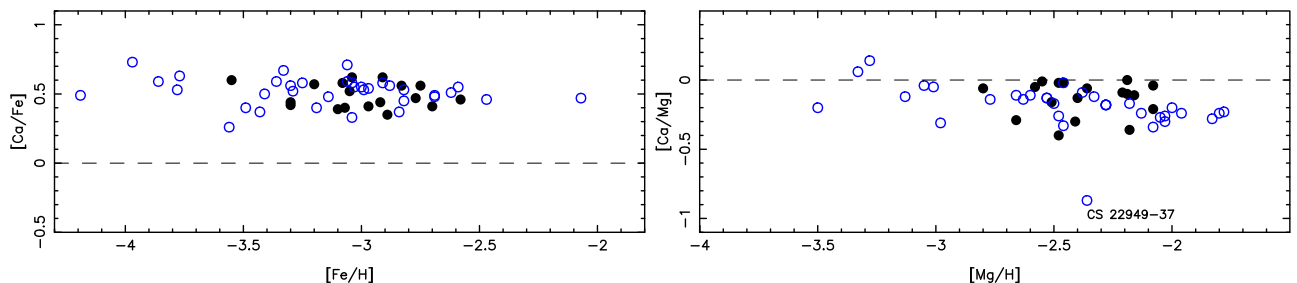


Fig. 2. **Left:** $[\text{Ca}/\text{Fe}]$ vs. $[\text{Fe}/\text{H}]$ and **(Right)** $[\text{Ca}/\text{Mg}]$ vs. $[\text{Mg}/\text{H}]$ at very low metallicity. Black dots, dwarfs, open symbols, giants. The calcium abundance of CS22949-37 is normal but it is Mg-rich and also C-rich, N-rich and O-rich (Depagne et al. 2002).

- In both cases there is a very good agreement between dwarfs and giants.
- In Fig. 2 (right) it seems that there is a slight increase of $[\text{Ca}/\text{Mg}]$ at very low metallicity but this trend is not significant (owing to the larger error on $[\text{Ca}/\text{Fe}]$ and $[\text{Ca}/\text{Mg}]$ at very low metallicity).
- Unexpectedly, the scatter of $[\text{Ca}/\text{Mg}]$ is a little larger than the scatter of $[\text{Ca}/\text{Fe}]$ although Ca and Mg are “ α elements” supposed to be formed in similar processes (unlike Fe).
- In the early Galaxy, if we consider the stars with $[\text{Fe}/\text{H}] < -2.7$: $[\text{Ca}/\text{Fe}] \approx +0.50 \pm 0.10$ dex and $[\text{Ca}/\text{Mg}] \approx -0.15 \pm 0.12$ dex.

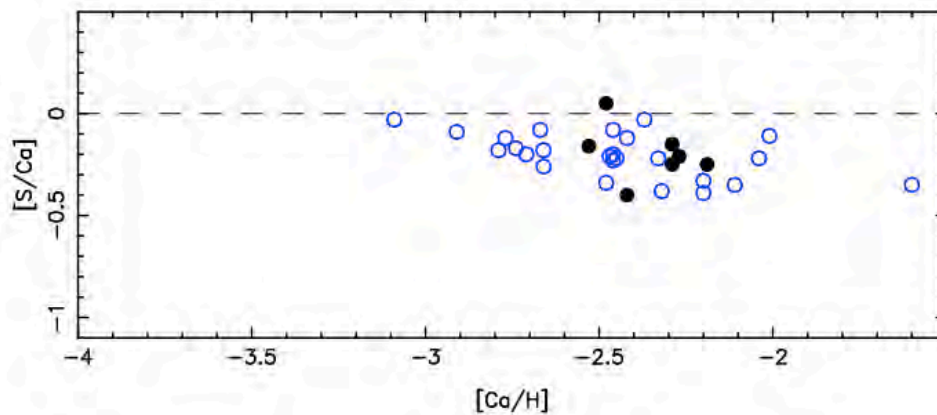


Fig. 3. $[\text{S}/\text{Ca}]$ vs. $[\text{Ca}/\text{H}]$. Symbols like in Fig. 2.

In Fig. 3 we present $[\text{S}/\text{Ca}]$ vs. $[\text{Ca}/\text{H}]$. S is also an “ α element”, its NLTE abundance has been taken from Spite et al. (2011). The correlation between the sulfur and the calcium abundance is very good, the spread of $[\text{S}/\text{Ca}]$ is small, smaller than the spread of $[\text{S}/\text{Mg}]$ (see Spite et al. 2011). This suggests that the production processes of S and Ca are more closely linked than the productions of S and Mg.

References

- Andrievsky S. M., Spite M., Korotin S. A., Spite F., Bonifacio P., Cayrel R. et al. 2010, *A&A*, 509, 88
 Andrievsky S. M., Spite F., Korotin S. A., François P., Spite M., Bonifacio P. et al. 2011, *A&A*, 530, 105
 Bonifacio P., Molaro P., Sivarani T., Cayrel R., Spite M., Spite F., Plez B. et al. 2007, *A&A*, 462, 851
 Bonifacio P., Spite M., Cayrel R., Hill V., Spite F., François P., Plez B. et al. 2009, *A&A*, 494, 1083
 Carlsson M. 1986, *Uppsala Obs. Rep.* 33
 Cayrel R., Depagne E., Spite M., Hill V., Spite F., François P., Plez B., et al. 2004, *A&A*, 416, 117
 Depagne E., Hill V., Spite M., Spite F., Plez B., et al. 2002, *A&A*, 390, 187
 Korotin S.A., Andrievsky S.M., Luck R.E. 1999, *A&A*, 351, 168
 Mashonkina L., Korn A.J., Przybilla N. 2007, *A&A*, 461, 261
 Meléndez M., Bautista M.A., Badnell N.R. 2007, *A&A*, 469, 1203
 Samson A.M., Berrington K.A. 2001, *ADNT*, 77, 87
 Spite M., Caffau E., Andrievsky S. M., Korotin S. A., Depagne E., Spite F., Bonifacio P. 2011, *A&A*, 528, 9
 Steenbock W., & Holweger H. 1984, *A&A*, 130, 319